

ENTANGLEMENT FOR ATOM INTERFEROMETERS

Von der QUEST-Leibniz-Forschungsschule
der Gottfried Wilhelm Leibniz Universität Hannover
zur Erlangung des Grades

Doktor der Naturwissenschaften

Dr. rer. nat.

genehmigte Dissertation von

M.Sc. ALEXANDER IDEL

Erscheinungsjahr 2021

REFERENT:
apl. Prof. Carsten Klempt

KOREFERENTEN:
Prof. Dr. Jan Arlt
Prof. Dr. Luis Santos

TAG DER PROMOTION:
29. April 2021

ABSTRACT

Quantum Sensors, like atom interferometers (AI), can be employed for high-precision measurements of inertial forces, including their application as gravimeters, gradiometers, accelerometers, and gyroscopes. Their measurement principle relies on ultracold atoms that are prepared in quantum-mechanical superposition states in external degrees of freedom. These states can be prepared by a momentum transfer of a Raman laser. Then the superposition state senses the effect of an inertial force, which induce a corresponding relative phase. The phase is read out by a final coupling which converts the interferometric phase into a atom number difference between the two states. The difference provides an estimate of the interferometric phase and the corresponding quantity of interest. The quantum mechanical noise of the atomic ensemble cause a fundamental uncertainty of this estimation, which I analyze for generic AIs. For small atomic densities, the quantum phase noise of the ensemble limits the interferometric sensitivity. For large densities, quantum number fluctuations generate density fluctuations, which generates phase noise. I show that these two competing effects result in an optimal atom number with a maximal interferometer resolution. Squeezed atomic samples allow for a reduction of the quantum noise of one quantity at the expense of an increased noise along of a conjugate quantity. Phase and number are such quantities which obey to a variant of Heisenberg's uncertainty principle. Neither phase nor number squeezing can improve the maximal interferometer resolution. As one main result of this thesis, I show how an optimal squeezing in between number and phase squeezing, allows for a fundamental improvement. I evaluate possible experimental paths to implement the proposed protocol.

Concepts for a squeezing-enhanced operation of external-degree AIs have not yet been demonstrated. I propose and implement an atomic gravimeter, which is designed to accept spin-squeezed atomic states as input states. The interferometer is designed such that the interferometer couplings are performed in spin space, while the phase accumulation is performed in momentum states. For this interferometer, the squeezed input can be directly obtained from spin dynamics in spinor Bose-Einstein condensates. The main noise contributions in the experiment are analyzed, which results in a factor of 84 above the relevant quantum limit, preventing a squeezing enhancement so far. I outline a suppression of the main noise source, uncontrolled AC Stark shift on the squeezed mode and propose future important applications, including test of spontaneous collapse theories and an improvement of large-scale, high-precision gradiometers.

Schlagworte: Verschränkung, Atominterferometrie, Quantenoptik

ACKNOWLEDGMENTS / DANKSAGUNG

Die Resultate dieser Arbeit konnten nur durch die tolle Unterstützung aller Beteiligten entstehen, bei denen ich mich hier bedanken möchte. Allen voran spreche ich meinen herzlichen Dank meinem Doktorvater Carsten Klempt aus, der mir die Möglichkeit gab, in einem neuen Themenbereich der Physik promovieren zu können. Er hatte immer ein offenes Ohr für alle Belange, egal ob in der wöchentlichen Gruppenbesprechung oder bei einem Kaffee oder Cappuccino. Er hat sein Wissen und seine Hilfe immer angeboten und geholfen. Ich möchte mich auch bei meinem Post-Doc Jan und meinem Seniorekollegen Karsten bedanken, die mich mit offenen Armen aufgenommen haben und mich in das Experiment eingearbeitet haben. Jan hat mich lange während meiner Promotionszeit begleitet und war immer ein kompetenter und hilfsbereiter Ansprechpartner für alle meine Fragen. Besonders sein Wissen über die Spezialitäten des Experiments waren häufig eine unschätzbare Hilfe. Auch vielen Dank an Karsten, dafür das du mir die vielen Tricks und Kniffe für das Experiment gezeigt hast. Speziellen Dank an meinen Kollegen Fabian, deine Kreativität und dein Wissen waren unersetzlich. Außerdem dank ich für die interessanten Kaffee (oder Tee/Kuchen) Pausen, die zu vielen interessanten Gesprächen geführt haben. Ich bedanke mich auch bei Bernd für die vielen interessanten Gespräche und den frischen Wind, die du in unsere Gruppe gebracht hast. Die gute Zusammenarbeit mit Polina hat mir viel über die Theorie beigebracht und ohne sie hätten wir viele Ideen nicht gehabt. Mareike, Bernd, Martin und Cebraill möchte ich ebenfalls für die gute Zusammenarbeit danken. Ich möchte mich an dieser Stelle auch bei Jan Arlt und Luis Santos für das Referieren meiner Arbeit bedanken.

Ebenso bedanke ich mich bei allen Mitgliedern der AG Rasel, dem Sekretariat und der Feinmechanikwerkstatt für ihre nette und hilfsbereite Art und das sie immer versucht haben alles möglich zu machen.

Ich möchte mich bei meiner Familie für die tolle Unterstützung, während meines gesamten Studiums bedanken.

Mein größter Dank gilt meiner Frau Johanna. Danke für deine Unterstützung und dein Verständnis für mich.

CONTENTS

Entanglement in Atom interferometer

1	INTRODUCTION	3
2	FUNDAMENTALS OF ATOM INTERFEROMETRY	7
2.1	Ensembles of 2-mode atoms	8
2.2	Interferometer input states	11
2.3	Beamsplitters and phase shifts	13
2.3.1	Spin domain	13
2.3.2	Momentum domain	14
2.4	Implementations	14
2.4.1	Microwave beam splitter	15
2.4.2	Bragg momentum kick	18
2.4.3	Raman momentum kick	19
3	FUNDAMENTAL SENSITIVITY LIMITS OF ATOM INTERFEROMETRY	23
3.1	Shot noise and density limit	23
3.2	Phase, number and optimal squeezing	25
3.3	Realistic application	29
3.4	Methods for generating squeezing	31
4	GENERATION OF SQUEEZING IN SPINOR BECS	33
4.1	Spinor BECs	33
4.2	Generation of entanglement	35
4.2.1	Two-mode squeezed vacuum states	38
4.2.2	Twin-Fock states	39
4.3	Geometries for entangled atom interferometers	40
4.3.1	Twin-Fock interferometer	42
4.3.2	Squeezed vacuum interferometer	44
5	EXPERIMENTAL SETUP	49
5.1	General experimental setup	49
5.1.1	Improvements of the existing system	51
5.1.2	State manipulation with microwaves	57
5.2	Interferometer setup	59
5.3	Noise sources in the interferometer and the state preparation	64
5.3.1	Raman laser	64
5.3.2	Microwave	66
5.3.3	Magnetic field	66
5.3.4	Detection noise	67
5.3.5	BEC life time	68
5.3.6	Laboratory temperature effects	68
6	GRAVIMETER	69
6.1	Results	69

6.1.1	Classical-interferometer	69
6.2	Discussion	76
6.2.1	Improvements	78
6.3	Squeezed vacuum vs. twin-Fock interferometer	79
7	CONCLUSION AND OUTLOOK	81
7.1	Conclusion	81
7.2	Outlook	81

Appendix

A	CALCULATIONS	87
A.1	Optimal squeezing	87
A.2	Artificial phase shift	88

	BIBLIOGRAPHY	89
--	--------------	----

LIST OF FIGURES

Figure 2.1	Classical interferometer	7
Figure 2.2	Single spin state representation on the Bloch sphere	9
Figure 2.3	Order of a collective spin	10
Figure 2.4	Squeezed states at the Bloch sphere	12
Figure 2.5	Dressed state picture and dressing MW.	15
Figure 2.6	Momentum transfer.	19
Figure 2.7	Multi momentum Raman transfer.	20
Figure 3.1	Classical interferometer	23
Figure 3.2	Different kinds of squeezing	27
Figure 3.3	Density depending squeezing	30
Figure 4.1	Spin changing collisions.	33
Figure 4.2	Parametric down conversion analogue.	34
Figure 4.3	Effective potential.	36
Figure 4.4	Level scheme for the twin-Fock interferometer.	42
Figure 4.5	State preparation for the twin-Fock interferometer.	43
Figure 4.6	Scheme of the twin-Fock interferometer	44
Figure 4.7	Level scheme for the squeezed vacuum interferometer.	45
Figure 4.8	State preparation for the squeezed vacuum interferometer.	46
Figure 4.9	Scheme of the squeezed vacuum interferometer	47
Figure 5.1	Experimental setup,modified from Ref.	49
Figure 5.2	interferometer setup.	50
Figure 5.3	Magnetic field stabilization.	53
Figure 5.4	Dipole trap laser distribution system.	54
Figure 5.5	Temperature fluctuations	56
Figure 5.6	Schematic of the microwave setup	57
Figure 5.7	Microwave cross transfer.	59
Figure 5.8	cross transfer pulse simulation.	60
Figure 5.9	Experimental interferometer setup.	61
Figure 5.10	Raman laser pulse shaping	63
Figure 5.11	Relative AC Stark shift.	65
Figure 5.12	Magnetic field noise.	67
Figure 6.1	Raman laser pulse duration measurement	69
Figure 6.2	Interferometer sequence	70
Figure 6.3	Mask placement on the absorption detection picture	72
Figure 6.4	Absorption pictures interferometer.	73

Figure 6.5	measurement of the gravitational acceleration	74
Figure 6.6	single state g measurement	75
Figure 6.7	g measurement with post correction	76
Figure 6.8	Histogram of the transferred fraction	77
Figure 6.9	measurement of the gravitational acceleration	78
Figure 6.10	Selective radio frequency transfer.	78

ENTANGLEMENT IN ATOM INTERFEROMETER

INTRODUCTION

The understanding of nature improved a lot in the last decades by high precision measurements. Two main pillars of our modern understanding are quantum mechanics and general relativity which were founded in the beginning of the 20th century. The description of general relativity [1] is relevant for macroscopic scales, where on the other hand quantum mechanics [2, 3] describe the wave behavior and the quantized energy on the microscopic scale. The most precise measurements nowadays are conducted with wave interference experiments. One example would be a long baseline laser interferometer like the "Laser Interferometer Gravitational Wave Observatory" (LIGO), which is used to measure gravitational waves predicted by Albert Einstein. This experiment directly observed a gravitational wave in 2015 [4]. Each of the two detectors measured a differential length variation with a peak amplitude of $\Delta L/L = 1.0 * 10^{-21}$. The LIGO detectors were already limited by the quantum projection noise, which they overcome with the use of squeezed states of light [5, 6]. The Heisenberg uncertainty principle states that it is not possible to exactly know the velocity and the position of a quantum particle at the same time. For an electromagnetic wave this principle also holds with the amplitude and the phase of the wave. That can be displayed by a classical state, a coherent state, where both quadratures have the same size, which can be imagine as a disk in a 2-D coordinate system. The squeezing is now reducing the quadrature in on direction, by increasing it in the other one, which turns the disk into an ellipse. The reduced quadrature is then used for the interferometric measurement.

But interferometers can not only be constructed with light, they can also be designed with massive particles. This interferometers can be used to prob a different frequency range of gravitational waves than light interferometers [7]. Massive particles can also be used to measure time and inertial quantities to a up to now unreached precision. The time is nowadays defined in the International System of Units (SI) by the hyperfine transition between the two ground levels of Cesium. Optical atom clocks, which are atomic clocks that use optical transitions in the atoms, already reached a instability of $6.6 * 10^{-19}$ [8]. These levels of precision would allow the measurement of local gravity effects by comparing two clocks, whose frequencies are changed by gravity, the so called gravitational red-shift. The gravitational red shift says that a clock runs faster or slower depending on the gravitational potential that it experience. These clocks are limited by the standard quantum limit (SQL) if the states are not squeezed which can be

overcome by using squeezed states. Squeezing can also be used instead of other methods to increase the stability of the clocks, like the increase of the particle number of used particles which may be limited by technical reasons. An example of a squeezed clock better than the standard quantum limit was shown earlier in our group [9].

Another way to use an atom interferometer is the measurement of an acceleration like the g -factor of Earth's acceleration. In such an interferometer, the atoms would be the wave and the light would act as a beamsplitter or mirror, which is like the reverse setup of a laser interferometer. To improve such an atom interferometer, there are different ways like the increase of the atom number in the ensemble or a longer interrogation time. As an example, an atom interferometer with a baseline of 10m, the "very long baseline interferometer", is built in Hannover. However, the length of a baseline and other factors can be technically limited. Then, squeezing could further increase the sensitivity of the atom interferometer. Up to now, it is not experimentally shown how entanglement can be implemented in an atom gravimeter.

For such a gravimeter, the momentum states of the atom interferometer need to be squeezed. There is the possibility to generate the squeezing directly in the momentum states or to transfer it to them from a generation in the internal states. There are different methods to generate the squeezing as for example atom-light interactions and atomic collisions. The creation of entangled pairs in the external degree of freedom was shown with Helium [10, 11] and Rubidium [12]. As an alternative, the entanglement can be generated between the two spatial modes in a double well potential [13, 14]. These techniques are not well suited for a measurement with a high atom number (entangled pairs) or have a problem with the individual access (double well potential). Therefore we can use atom-light interactions. It was used to generate squeezing in laser-cooled samples [15–17] or gas cells [18, 19]. The best squeezing of 20.1dB was shown by using atom-light interaction of an atomic ensemble in a cavity [20]. These results were shown in thermal atomic ensembles and not in Bose-Einstein condensates (BEC), which are beneficial for a longer interrogation time due to the lower expansion rates of the condensate. Therefore, atomic collisions in a Bose-Einstein condensate, which can be used to generate entangled states by using non-linear effects, should be used.

The most promising technique for entanglement on internal states with the necessary parameter for an gravimeter is the creation of entanglement in the internal states. It can be generated by one-axis twisting (OAT) by exploiting the different collisional properties of two spin states [21, 22]. A second way is the use of spin changing collisions (SCC) to generate twin-Fock states [23, 24] or spin-squeezed states [9, 25–27]. In this work, SCC is considered to be the most beneficial method for our experimental setup.

To use the squeezed states in an high precision atom interferometer, other effects need to be taken into account. At high atom numbers, that is the density shift of the phase due to a high atom number in the BEC, which can lead to a relative phase shift between the two path of the atom interferometer. That can be counteracted by choosing the right squeezing angle to counteract the twisting caused by the density shift. I will show how to calculate this optimal squeezing angle and will also present a scheme that is made to use this optimal squeezing. Furthermore, i will show a realization of the scheme which shows the measurement of the acceleration of Earth, with a 3-mode interferometer approach. This allows us to analyses the influence of external parameters and noise to the signal. Especially the relative phase between the 2 of the 3 modes is analyzed, due to their strong influence on the signal contrast.

This work is structured in the following way: In the second chapter, the fundamentals of atom interferometry are explained. Furthermore, the effect of different types of momentum transfer for a beamsplitter is discussed. In the third chapter the fundamental limits of an atom interferometer such as the shot noise and density limit are explained. The noise for a realistic interferometer setup is calculated and discussed, as well as which generation technique for an entangled state is the most promising at the moment. The chosen techniques for generation of entanglement are explained and described theoretically in chapter 4. Two possible geometries for inertially sensitive atom interferometers are developed and explained, each for a different entangled input state. The fifth chapter explains the full experimental setup and the interferometric setup in detail. The improvements in the setup since the work of B. Lücke [28] are described and finally the influence of the different technical noise sources is investigated. In chapter 6 the results are presented and discussed also in the context of technical noise and fundamental limits. The final chapter 7 gives a conclusion of this work and an outlook for what the results in this work can be used and what could be further possible improvements.

For the understanding of entanglement in atom interferometers it is important to consider the basics of atom-atom and atom-light interactions and the basic structure of different atom interferometers. These will be explained in this chapter.

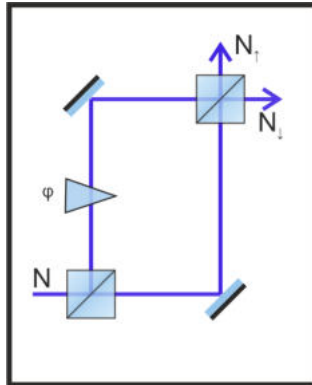


Figure 2.1: **Classical interferometer**

The input port has N particles and the second input port is empty. The first beamsplitter creates a superposition of state one (upper path) and state two (right path). In the upper path, a phase shift φ is applied. Due to the second beamsplitter the both path interfere with each other. That results in a change of the mean atom number in $\langle N_{\uparrow} \rangle$ and $\langle N_{\downarrow} \rangle$ at the output ports, depending on the relative phase φ .

A classical atom interferometer can be understood as an analogon to the light interferometer. Instead of having N photons at an input port, we have N particles there. The atoms are then split into two separated clouds by a beam splitting process. They will accumulate a relative phase shift to each other, shown by φ in Fig. 2.1. After a second beam splitting, which interfere the two particle clouds, the particle numbers can be measured at the two output ports. Due to the relative phase shift, the number difference at the output ports change.

This phase shift can now be caused by different sources. We need to differentiate between atom interferometers on the internal degrees of freedom and the external ones. On the internal degrees of freedom a phase shift can be caused by a detuning between the internal energy levels, where the transfers are done. This will be explained in Sec. 2.4. On the external degrees of freedom a relative phase shift can be caused by a spatial distance between the two particle clouds. Due to a different momentum of the clouds they can separate and then be at different positions. There they can experience different external

potentials which cause the phase shift. It is possible to have phase shifts from external and internal degrees of freedom in the same interferometer.

2.1 ENSEMBLES OF 2-MODE ATOMS

First we define an orthonormal basis for a 2-mode particle. The basis can be a spin-up state ($|\uparrow\rangle$) and a spin-down state ($|\downarrow\rangle$). They are here oriented along the z-axis, so $|\uparrow\rangle$ on the north pole and $|\downarrow\rangle$ on the south pole of the Bloch sphere, shown in Fig. 2.9. These are the eigenvalues of a spin measurement of the spin operator s_z . The full Bloch sphere is defined by the expectation value of the three spin operators s_x, s_y, s_z measuring along the corresponding axes [29]. The operators can be written as

$$s_x = \frac{1}{2}(|\downarrow\rangle\langle\uparrow| + |\uparrow\rangle\langle\downarrow|) \quad (2.1)$$

$$s_y = \frac{1}{2i}(|\downarrow\rangle\langle\uparrow| - |\uparrow\rangle\langle\downarrow|) \quad (2.2)$$

$$s_z = \frac{1}{2}(|\uparrow\rangle\langle\uparrow| - |\downarrow\rangle\langle\downarrow|). \quad (2.3)$$

They can be also written in dependency of the Pauli matrices σ_k as

$$s_x = \frac{1}{2} \begin{pmatrix} 0 & 1 \\ 1 & 0 \end{pmatrix} = \frac{1}{2}\sigma_x \quad (2.4)$$

$$s_y = \frac{1}{2} \begin{pmatrix} 0 & -i \\ i & 0 \end{pmatrix} = \frac{1}{2}\sigma_y \quad (2.5)$$

$$s_z = \frac{1}{2} \begin{pmatrix} 1 & 0 \\ 0 & -1 \end{pmatrix} = \frac{1}{2}\sigma_z. \quad (2.6)$$

The operators also fulfill the commutator relation

$$[s_k, s_l] = i\epsilon_{klm}s_m. \quad (2.7)$$

Now, the basis of $|\uparrow\rangle$ and $|\downarrow\rangle$ can be used to describe every possible superposition of a pure spin state, as a function of θ and φ ,

$$|\psi\rangle = a|\uparrow\rangle + b|\downarrow\rangle = e^{i\varphi/2}\cos\left(\frac{\theta}{2}\right)|\uparrow\rangle + e^{-i\varphi/2}\sin\left(\frac{\theta}{2}\right)|\downarrow\rangle, \quad (2.8)$$

with $0 \leq \varphi < 2\pi$ as the relative phase and $0 \leq \theta < \pi$ as the ratio between $|\uparrow\rangle$ and $|\downarrow\rangle$. Therefore, the expectation values of the spin operators are

$$\langle \vec{s} \rangle = \begin{pmatrix} \langle s_x \rangle \\ \langle s_y \rangle \\ \langle s_z \rangle \end{pmatrix} = \frac{1}{2} \begin{pmatrix} \sin(\theta)\cos(\varphi) \\ \sin(\theta)\sin(\varphi) \\ \cos(\theta) \end{pmatrix}. \quad (2.9)$$

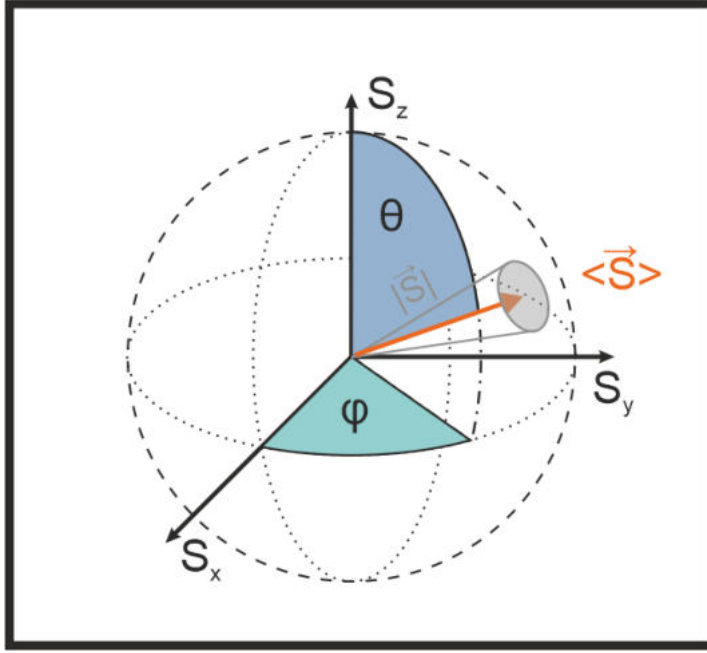


Figure 2.2: **Single spin state representation on the Bloch sphere**

A single spin state \vec{s} can be described on a Bloch sphere. It is visualized by a cone around $\langle \vec{s} \rangle$, which is the mean orientation (orange vector) of \vec{s} . Because the spin length $|\vec{s}| = \sqrt{s(s+1)}$ of is longer than the mean it constructs the cone. The differences between the mean and the side lengths span the gray disk on the surface of the Bloch sphere. The mean direction is described in polar coordinates in dependency of θ and φ .

That allows to display every expectation value of \vec{s} on the surface of the Bloch sphere in Fig. 2.9 and is also the same style as a standard polar coordinate system with a radius of $r = \frac{1}{2}$. The length of these vectors is $|\langle \vec{s} \rangle| = \frac{1}{2}$ for a pure spin state and the vectors lie on the surface of the Bloch sphere. But the length of the spin $|\vec{s}|$ defined by quantum mechanics differs from the length of the expectation value of the spin. It is

$$|\vec{s}| = \sqrt{\langle \vec{s}^2 \rangle} = \sqrt{s(s+1)} = \sqrt{\frac{3}{4}}, \quad (2.10)$$

which is longer than the expectation value. Therefore, it is possible to represent the spin as a cone on the Bloch sphere, where the area on the sphere is defined by fluctuations of the other spin components. This is caused by the non-vanishing commutator relations in Eq. 2.7. This leads to Heisenberg-like uncertainty relation of the operators

$$(\Delta s_l)^2 (\Delta s_m)^2 \geq \frac{1}{4} |\langle s_n \rangle|^2, \quad (2.11)$$

with l, m, n can be x, y, z in any permutation.

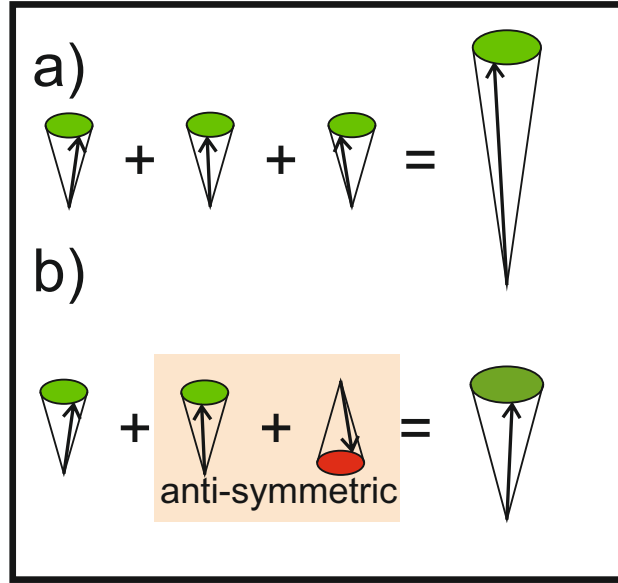


Figure 2.3: **Order of a collective spin**

a) In a pure multi-particle spin state of Bosons, all spins are pointing in the same direction, they are symmetric and indistinguishable. Then, the collective spin length is maximal $J_{max} = \frac{N}{2}$. b) In a mixed state the spins can be also be ordered anti-symmetrical and be distinguishable, therefore the collective spin length is in general not maximal.

This description of a single spin can now be extended to a multi-spin description with a Bloch sphere for the sum of the spins. This collective spin \vec{J} can be calculated as

$$\vec{J} = \sum_{k=1}^N \vec{s}^{(k)}, \quad (2.12)$$

with N as the particle number and $\vec{s}^{(k)}$ as the individual spins. The collective spin operators J also follow the commutator relation Eq. 2.7, which is

$$[J_l, J_m] = i\epsilon_{lmn}J_n. \quad (2.13)$$

Therefore also the uncertainty is Heisenberg related as

$$(\Delta J_l)^2(\Delta J_m)^2 \geq \frac{1}{4}|\langle J_n \rangle|^2, \quad (2.14)$$

with l, m, n as a permutation of x, y, z in the same reference system as for the single spin. This is now a multi-particle Bloch sphere, where the length of \vec{J} is approximated by

$$\sqrt{\langle \vec{J}^2 \rangle} = \sqrt{J(J+1)} \approx J, \quad (2.15)$$

with the approximation that the particle number N is high, which is usually the case in our experiment. Calculating now the maximum

spin length J_{max} for a symmetric spin state (shown in Fig. 2.3a)) leads to $J_{max} = \frac{N}{2}$, by using Eq. 2.12 and $s = \frac{1}{2}$. Therefore, the Bloch sphere has a radius of $\frac{N}{2}$. Concluding from the uncertainty relation 2.13, the collective spin state is described as a cone, similar to the single spin description. The fluctuations can be described by assuming that they are uncorrelated, therefore $(\Delta J_x)^2 = (\Delta J_z)^2$, with the assumption that the vector is pointing in the direction of the J_y -axis. Then we use Eq. 2.14 with $J_{max} = \frac{N}{2}$ which leads to

$$\begin{aligned} (\Delta J_z)^2 (\Delta J_z)^2 &\geq \frac{1}{4} |\langle J_y \rangle|^2 = \frac{1}{4} \left(\frac{N}{2} \right)^2 \\ \Rightarrow (\Delta J_z)^2 &\geq \frac{1}{2} \frac{N}{2} \\ \Rightarrow \Delta J_z &\geq \frac{\sqrt{N}}{2}, \end{aligned} \quad (2.16)$$

which is a lower bound for the noise, the so-called shot-noise limit. In a measurement with the employed basis, the J_z -axis is a measurement of the difference between the spin up and the spin down state. Therefore is

$$\Delta J_z = \frac{1}{2} \Delta(N_\uparrow - N_\downarrow). \quad (2.17)$$

That leads to the minimal noise in a measurement of

$$\Delta(N_\uparrow - N_\downarrow) = 2\Delta J_z = \sqrt{N}, \quad (2.18)$$

which shows the particle number dependency of the shot-noise limit.

For a non-symmetric state the spin length can be smaller than J_{max} , therefore the cone can end inside the Bloch sphere and not on the surface, this shortened cone is depicted in Fig. 2.3b). A perfect BEC with indistinguishable particles is a symmetric state.

The collective spin operators can be written in the following form [30, 31]:

$$\begin{aligned} J_x &= \frac{1}{2}(a^\dagger b + b^\dagger a) \\ J_y &= \frac{1}{2i}(a^\dagger b - b^\dagger a) \\ J_z &= \frac{1}{2}(a^\dagger a + b^\dagger b), \end{aligned} \quad (2.19)$$

where a, a^\dagger are the bosonic annihilation and creation operators for a spin up particle $|\uparrow\rangle$ and b, b^\dagger respectively for a spin down state $|\downarrow\rangle$. This will be helpful for the description of the different entangled states.

2.2 INTERFEROMETER INPUT STATES

In our experimental setup, we have two sorts of interferometer input states that can be combined with each other. There are the internal

states in the spin domain and the external states in the momentum domain. The input states for the momentum domain will be always a freely falling BEC in this thesis. The different input states will be generated in the internal degrees of freedom and then transferred to the external ones. Therefore the internal state can be chosen as a classical or a non-classical state.

As shown in the section before, the interferometer states can be displayed on the multi-particle Bloch sphere, where a classical state is represented by a disk on the surface. As an example the measurement of the number of particles in $|\uparrow\rangle$ and $|\downarrow\rangle$ is a projection onto the J_z axis, therefore the fluctuation in this direction should be as small as possible, which is $\Delta(N_\uparrow - N_\downarrow) = \sqrt{N}$ for a classical state as shown in Eq. 2.18. This limit can be overcome with squeezing i.e. reducing the fluctuations in one direction, e.g. the z -axis at a cost of higher fluctuations in the y - or x -direction. In the following, a few example states are shown.

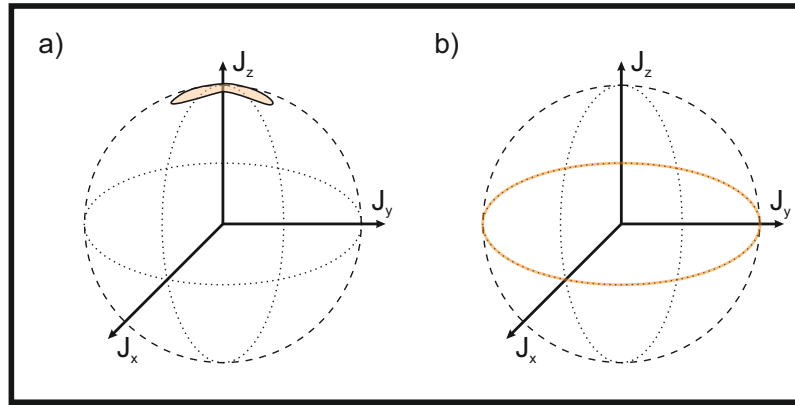


Figure 2.4: Squeezed states at the Bloch sphere

a) Squeezed vacuum state on a multi-particle Bloch sphere. The coherent state is squeezed around the J_x -axis of the Bloch sphere. b) Twin-Fock state with vanishing width in J_z direction and undefined phase, which is displayed by the complete ring around the equator of the Bloch sphere.

A squeezed vacuum state is a squeezed state where the expectation value of the quadratures remain zero. It can be employed in interferometry by coupling it to the empty input port instead of squeezing the main port with a large number of particles. This has the benefit that the gain of squeezing can be reached without the challenge of generating squeezing in a large amount of atoms. For a classical state, the vacuum port of an interferometer input is empty, for the squeezed vacuum state this port is weakly populated by squeezed atoms. This can be displayed by an ellipse on the multi-particle Bloch sphere, as shown in Fig. 2.4a).

A twin-Fock state have a vanishing width in J_z direction and undefined phase, shown in Fig. 2.4b). This makes a twin-Fock state a highly

sensitive state for interferometry if the squeezed direction (here J_z) is used to sample the phase information with a higher sensitivity than a classical state.

2.3 BEAMSPLITTERS AND PHASE SHIFTS

2.3.1 Spin domain

The manipulation of states can be shown on Bloch spheres. Here I will explain a beam splitter and a phase shift on the multi-particle Bloch sphere as an example.

The beam splitter brings a particle in one of the two starting spin states ($|\uparrow\rangle$ and $|\downarrow\rangle$) into a superposition state. This can be understood geometrically on the Bloch sphere as a rotation around the s_x -axis or s_y -axis [30], as an example we will choose here the s_x -axis. That leads to

$$\vec{s}^{(k)} = \begin{pmatrix} s_x^{(k)} \\ s_y^{(k)} \\ s_z^{(k)} \end{pmatrix} = \begin{pmatrix} 1 & 0 & 0 \\ 0 & \cos(\theta) & -\sin(\theta) \\ 0 & \sin(\theta) & \cos(\theta) \end{pmatrix} \begin{pmatrix} s_x^{(k)} \\ s_y^{(k)} \\ s_z^{(k)} \end{pmatrix} \quad (2.20)$$

for a single particle with the spin $\vec{s}^{(k)}$, with θ as defined before. The description is similar for the multi-particle Bloch sphere because the collective spin \vec{J} is only the sum of the single spins $\vec{s}^{(k)}$ (see Eq. 2.12). Therefore the beam splitter for the multi-particle spin can be described as

$$\vec{J} = \begin{pmatrix} J_x \\ J_y \\ J_z \end{pmatrix} = \begin{pmatrix} 1 & 0 & 0 \\ 0 & \cos(\theta) & -\sin(\theta) \\ 0 & \sin(\theta) & \cos(\theta) \end{pmatrix} \begin{pmatrix} J_x \\ J_y \\ J_z \end{pmatrix}. \quad (2.21)$$

In the interferometer sequence I will use a 50:50 beamsplitter which is reached at an angle of $\theta = \frac{\pi}{2}$.

For our interferometer, a relative phase shift is necessary to measure the desired quantity which will be imprinted onto the phase. A relative phase on the multi-particle Bloch sphere is depicted similarly to the beam splitting by a rotation. This time the rotation is around the J_z -axis. This can be written as

$$\vec{J} = \begin{pmatrix} J_x \\ J_y \\ J_z \end{pmatrix} = \begin{pmatrix} \cos(\varphi) & -\sin(\varphi) & 0 \\ \sin(\varphi) & \cos(\varphi) & 0 \\ 0 & 0 & 1 \end{pmatrix} \begin{pmatrix} J_x \\ J_y \\ J_z \end{pmatrix}, \quad (2.22)$$

with φ as defined before for the angle in the J_x, J_y plane on the multi-particle Bloch sphere.

The combination of multiple of these two operations to the full interferometer sequence will be shown now. To describe the full sequence

we need a beam splitter operation, a phase shift and again a beam splitter operation. These matrices multiplied with each other, leads to

$$\vec{J} = \begin{pmatrix} J_x \\ J_y \\ J_z \end{pmatrix} = \begin{pmatrix} \cos(\varphi) & 0 & \sin(\varphi) \\ 0 & 1 & 0 \\ \sin(\varphi) & 0 & -\cos(\varphi) \end{pmatrix} \begin{pmatrix} J_x \\ J_y \\ J_z \end{pmatrix}. \quad (2.23)$$

Each of the operation beam splitter and phase shift can consist of multiple parts in the experimental sequence, e.g. a transfer in the internal states and on the external states.

2.3.2 Momentum domain

In the previous subsection, the description of a beam splitter and a phase shift in the spin domain was explained. It is also possible to describe both in the momentum domain. In Sec. 2.4 the technical implementation of the beam splitting and phase shifting process will be explained.

It is possible to describe the operations in the basis of two momentum states similar to Eq. 2.21 and Eq. 2.22. The difference is, that instead of spin up $|\uparrow\rangle$ and spin down $|\downarrow\rangle$, two momentum states are the basis for the description, $|0\rangle = 0\hbar k$ and $|1\rangle = +2\hbar k$. These different momenta will then lead to a spatial splitting of the two clouds.

They also have the same uncertainty relation as the spin states 2.18 which means that they also need to be displayed as a disk on the surface of the Bloch sphere. In the phase shift description, the difference is that the particles could be influenced by an external potential difference which defines the phase instead of the detuning between the two spin states. An example would be the potential difference of gravity, when the the two particle clouds are on different heights compered to earth. This results then in an extra phase shift. This will be shown in more detail in Sec. 2.4. These two ways to sample a phase (detuning of internal energy levels and external potential) need to be kept in mind if we construct the interferometer sequence.

It is possible that during an interferometer sequence a phase is sampled from the detuning of the internal states and also from the gravitational potential difference. If both of these phases are variable, it would make it more complex to recalculate the external acceleration back from the phase. For the planed interferometers the internal phase shift is a fixed value. This cause only an offset to the phase that is sampled due to the gravitational potential difference.

2.4 IMPLEMENTATIONS

Now we come to a more experimentally focused description of how to implement a beam splitter or a phase shift in our experiment in the different domains.

2.4.1 Microwave beam splitter

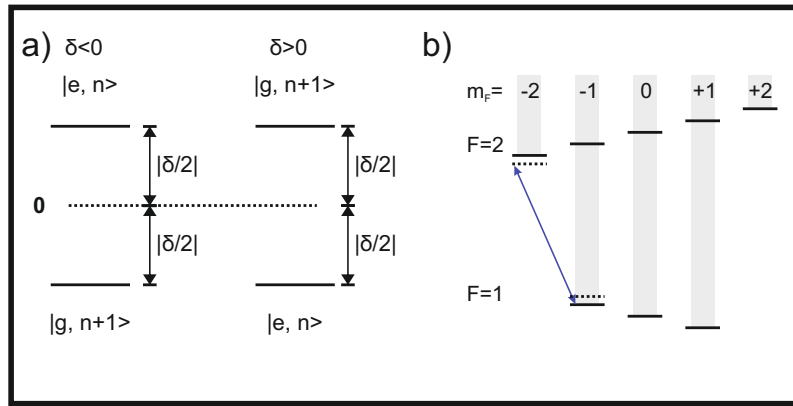


Figure 2.5: Dressed state picture and dressing MW.

a) The energy difference of the bare states $|g, n + 1\rangle$ and $|e, n\rangle$ is δ without coupling to a dressing field. The relation of the bare states to the 0 line depends on the sign of δ (dashed line, only guide to the eye). b) In our experiment we use a strong detuned microwave field to couple the $|F = 1, m_F = -1\rangle$ state with the $|F = 2, m_F = -2\rangle$ state. This coupling generate the dressed states which are the eigenstates of the Hamiltonian with microwave coupling. They can be written as a superposition of the bare states.

For the implementation of a beam splitter in the spin domain we can use a microwave coupling pulse. First, the system of dressed and bare states will be introduced to explain how the transfer and the dressing works, because the system of dressed states is necessary to explain the generation of entanglement in Sec. 4.2. Then, it will be simplified again to explain the case of microwave transfer.

To describe the change in energy difference between two states due to the influence of a microwave field, the dressed state picture can be used. This is used in many cold atom experiments [26, 32–34]. The energy levels of a ^{87}Rb BEC can be shifted by coupling the hyperfine levels by a detuned microwave signal with a frequency ω . We use a microwave dressing in the experiment on the $|F = 1, m_F = 1\rangle \leftrightarrow |F = 2, m_F = 2\rangle$ transition as shown in Fig. 2.5b) to enable spin dynamics which will be described in chapter 4. There I will also give an explanation why this transition is chosen. As an example we use the state of an atom in the Zeeman level $F = 1, m_F = 1$ as the ground state $|g\rangle$ and the excited state $|e\rangle$ is in the Zeeman level $F = 2, m_F = 2$. The energy difference between these two states is $\omega_0 = E_e - E_g$ and ω is close to ω_0 .

For a system without any coupling between the microwave signal and the atoms, the bare states $|g, n\rangle$ and $|e, n\rangle$ are the eigenstates of the system, with n as the number of microwave photons. When the microwave frequency is exactly the same $\omega = \omega_0$, the states

$|\psi_g\rangle = |g, n+1\rangle$ and $|\psi_e\rangle = |e, n\rangle$ have the same energy and are coupled by the microwave. The detuning $\delta = \omega - \omega_0$ of the microwave frequency results in a corresponding energy difference $\hbar\delta$ of these two states. The zero energy is chosen in a way that it is between the two levels and the states have the energy $\pm\frac{\delta}{2}$ as shown in Fig. 2.5a).

With the bare states as a basis, the Hamiltonian [29] of the effective two-level atom in a microwave field is

$$H = \frac{1}{2} \begin{pmatrix} \delta & \Omega \\ \Omega & -\delta \end{pmatrix} \quad (2.24)$$

with the resonant coupling Ω between the two states, depending on the microwave power P , because $\Omega \propto \sqrt{n} \propto \sqrt{P}$. Then the bare states are not longer the eigenstates of the Hamiltonian, because of the coupling of the microwave field to the bare states. Instead the new eigenstates of the system are the dressed states

$$\begin{aligned} |\psi_+\rangle &= \sin\left(\frac{\phi}{2}\right) |g, n+1\rangle + \cos\left(\frac{\phi}{2}\right) |e, n\rangle \\ |\psi_-\rangle &= \cos\left(\frac{\phi}{2}\right) |g, n+1\rangle - \sin\left(\frac{\phi}{2}\right) |e, n\rangle \end{aligned} \quad (2.25)$$

with $\phi = \tan^{-1}\left(\frac{\Omega}{\delta}\right)$. The energies of these eigenstates are then

$$\begin{aligned} E_+ &= +\frac{1}{2}\sqrt{\Omega^2 + \delta^2} \\ E_- &= -\frac{1}{2}\sqrt{\Omega^2 + \delta^2}. \end{aligned} \quad (2.26)$$

This means that the bare states are no longer degenerate and change to the dressed states which have an energy difference of Ω at $\delta = 0$.

Now we calculate the energy shift for the dressed states ΔE_g and ΔE_e . For this the energies of the corresponding bare states $E_e = -\frac{\delta}{2}$ and $E_g = +\frac{\delta}{2}$ are subtracted from the dressed states, which results in

$$\Delta E_g = +\frac{1}{2}\sqrt{\Omega^2 + \delta^2} - \frac{\delta}{2} = +\frac{\delta}{2} \left(\sqrt{\frac{\Omega^2}{\delta^2} + 1} - 1 \right) \quad (2.27)$$

$$\Delta E_e = -\frac{1}{2}\sqrt{\Omega^2 + \delta^2} + \frac{\delta}{2} = -\frac{\delta}{2} \left(\sqrt{\frac{\Omega^2}{\delta^2} + 1} - 1 \right). \quad (2.28)$$

The sign of these shifts depends on the sign of the detuning δ , as depicted in Fig. 2.5a), because the term in the brackets will always be positive. For a microwave frequency $\omega < \omega_0$, the detuning is negative $\delta < 0$, and the energy difference $E_e - E_g$ is increased by the dressing, because the ground state and the excited state are both shifted away from the zero line. Contrary, for a detuning $\delta > 0$, the energy difference is reduced by the dressing.

MICROWAVE TRANSFER It is also possible to transfer atoms between the internal energy states. During the state preparation in the experiment, we employ resonant microwave pulses with a detuning $\delta = 0$. Then, the bare states $|\psi_g\rangle$ and $|\psi_e\rangle$ can be expressed by the dressed states $|\psi_-\rangle$ and $|\psi_+\rangle$ using Eq. 2.25 and zero detuning

$$\sin\left(\frac{\phi}{2}\right) = \cos\left(\frac{\phi}{2}\right) = \frac{1}{\sqrt{2}}, \quad (2.29)$$

because of $\phi = \tan^{-1}\left(\frac{\Omega}{0}\right) = \tan^{-1}(\infty) = \frac{\pi}{2}$. This leads to

$$\begin{aligned} |\psi_g(t)\rangle &= \sin\left(\frac{\phi}{2}\right) |\psi_+(t)\rangle + \cos\left(\frac{\phi}{2}\right) |\psi_-(t)\rangle \\ &= \frac{1}{\sqrt{2}} |\psi_+(t)\rangle + \frac{1}{\sqrt{2}} |\psi_-(t)\rangle \end{aligned} \quad (2.30)$$

$$\begin{aligned} |\psi_e(t)\rangle &= \cos\left(\frac{\phi}{2}\right) |\psi_+(t)\rangle - \sin\left(\frac{\phi}{2}\right) |\psi_-(t)\rangle \\ &= \frac{1}{\sqrt{2}} |\psi_+(t)\rangle - \frac{1}{\sqrt{2}} |\psi_-(t)\rangle. \end{aligned} \quad (2.31)$$

The time dependence [29] of the dressed states follows from the Heisenberg equation of motion

$$i\hbar \frac{\partial}{\partial t} \psi_{\pm} = H \psi_{\pm} = \pm \frac{\Omega}{2} \psi_{\pm}, \quad (2.32)$$

by using Eq. 2.26 and can be then expressed by

$$|\psi_+(t)\rangle = e^{-it\frac{\Omega}{2}} |\psi_+\rangle \quad (2.33)$$

$$|\psi_-(t)\rangle = e^{it\frac{\Omega}{2}} |\psi_-\rangle. \quad (2.34)$$

Using Eq. 2.25, the bare ground state can be written as

$$\begin{aligned} |\psi_g(t)\rangle &= \frac{1}{\sqrt{2}} e^{-it\frac{\Omega}{2}} |\psi_+\rangle + \frac{1}{\sqrt{2}} e^{it\frac{\Omega}{2}} |\psi_-\rangle \\ &= \frac{1}{\sqrt{2}} \left(e^{-it\frac{\Omega}{2}} \frac{1}{\sqrt{2}} (|\psi_g\rangle + |\psi_e\rangle) + e^{it\frac{\Omega}{2}} \frac{1}{\sqrt{2}} (|\psi_g\rangle - |\psi_e\rangle) \right) \\ &= \frac{1}{2} \left(|\psi_g\rangle (e^{-it\frac{\Omega}{2}} + e^{it\frac{\Omega}{2}}) + |\psi_e\rangle (e^{-it\frac{\Omega}{2}} - e^{it\frac{\Omega}{2}}) \right) \\ &= \cos\left(\frac{t\Omega}{2}\right) |\psi_g\rangle - i \sin\left(\frac{t\Omega}{2}\right) |\psi_e\rangle. \end{aligned} \quad (2.35)$$

Respectively, the excited state becomes

$$\begin{aligned} |\psi_e(t)\rangle &= \frac{1}{\sqrt{2}} e^{-it\frac{\Omega}{2}} |\psi_+\rangle - \frac{1}{\sqrt{2}} e^{it\frac{\Omega}{2}} |\psi_-\rangle \\ &= -i \sin\left(\frac{t\Omega}{2}\right) |\psi_g\rangle + \cos\left(\frac{t\Omega}{2}\right) |\psi_e\rangle. \end{aligned} \quad (2.36)$$

This is also a description for a beamsplitter, which shows that we can use the microwave transfer as an beamsplitter.

Now, we want to see the time evolution of the population of the excited state. With a particle starting in the ground state $|\psi_g\rangle$ and a microwave pulse with the time t , the probability P_e that the particle is in the excited state $|\psi_e\rangle$ after the pulse is given by

$$P_e(t) = |\langle\psi_e(t)|\psi_g\rangle|^2 = \sin^2\left(\frac{t\Omega}{2}\right), \quad (2.37)$$

without detuning. This is a Rabi oscillation, which transfers all atoms from the ground to the excited state with a resonant π -pulse ($t_\pi = \frac{\pi}{\Omega}$). A 50 : 50 beamsplitter would be a resonant $\frac{\pi}{2}$ -pulse ($t_{\pi/2} = \frac{\pi}{2\Omega}$). These will be used in the interferometer sequence in Sec. 4.3. For an existing detuning $\delta \neq 0$ the probability P_e is

$$P_e(t) = \frac{\Omega^2}{\Omega_R^2} \sin^2\left(\frac{t\Omega_R}{2}\right) \quad (2.38)$$

with $\Omega_R = \sqrt{\Omega^2 + \delta^2}$, which makes the oscillation faster but also the maximal transfer probability lower. This prevents a complete transfer. Therefore, a resonant pulse is necessary for a 100% transfer as it is desired in our state preparation and for some parts of the interferometer sequence. That is important for the review on the noise sources in Sec. 5.3.

2.4.2 Bragg momentum kick

One way to implement a momentum transfer that is required for a momentum beam splitter is the Bragg deflection. Bragg deflection has the benefit that a transfer of more than $1008\hbar k$ is possible, which increases the signal of the interferometer [35]. It is similar to a deflection of light on a grating, where the light is shifted in frequency and direction, depending which order of the grating is used.

With a Bragg deflection, the atoms are deflected by a moving light wave described by

$$E_{kin} = n\hbar(\omega_1 - \omega_2) = n\hbar\omega_r \quad (2.39)$$

with ω_r as the photon recoil frequency an n as the order of diffraction [35] and $\omega_{1/2}$ as the frequencies of the standing wave in respect to the two different momentum states $|p_0\rangle = 0\hbar k$ and $|p_1 = 2\hbar k\rangle$. That can be used as shown in Fig. 2.6b) with a standing wave in an angle to the direction of the atoms [36, 37] or with two laser beams with a frequency difference ω_n that are retro-reflected. This transition frequency is described by the sum of the Doppler shift ω_0 and the photon recoil frequency ω_r , due to the already existing momentum of the atoms:

$$\omega_n = 2n\omega_r + \omega_0 \quad (2.40)$$

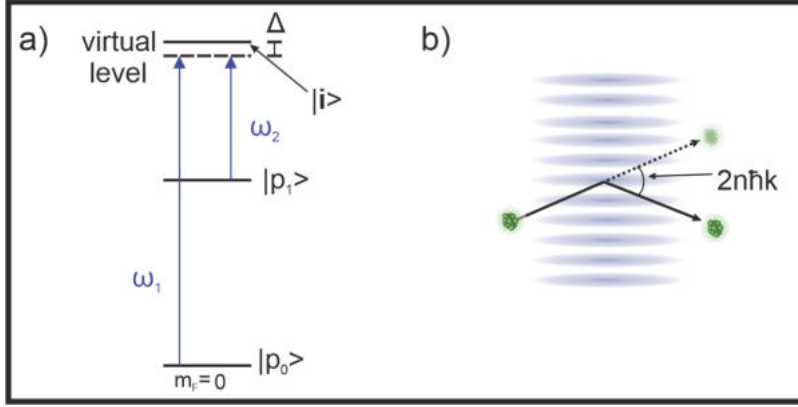


Figure 2.6: **Momentum transfer.**

a) Level scheme for a 2-photon transfer in ^{87}Rb , that can transfer a momentum of $2\hbar k$ and only depends on the momentum states. Both laser couple with the frequencies ω_1 and ω_2 to a virtual level that is detuned by Δ from the $5P_{3/2}$ manifold. The difference between ω_1 and ω_2 is proportional to the energy difference due to the different momentum of $p_1 = p_0 + 2\hbar k$. b) Bragg deflection on a standing wave. The standing wave of the laser acts as a lattice that transfers $2n\hbar k$ momentum to the atom ensemble, if the atoms move in an angle to the laser direction.

Bragg deflection is in general independent from the internal state of the atoms and only depends on the momentum states. That is beneficial for some experiments, but for the schemes that are used in this work it is a disadvantage, because the entanglement that should be used to improve a measurement will be generated in different internal states. For that reason, another method is used to transfer the momentum as explained in the following part.

2.4.3 Raman momentum kick

A second possibility to implement a momentum kick is a stimulated Raman transfer. The Raman transfer is a two-photon process with two phase-locked lasers to transfer atoms from one hyperfine state to another. In this work, we want to transfer the atoms from $|F = 1, m_F = 0\rangle$ to $|F = 2, m_F = 0\rangle$ or vice versa, because these states are magnetically insensitive in first order which is beneficial for an interferometer. For the two-photon process both lasers are detuned to a virtual level as shown in Fig. 2.6a).

The electric field $E(t)$ of this transition can be described by

$$E(t) = E_1 \cos(\omega_1 t + \varphi) \hat{e}_1 + E_2 \cos(\omega_2 t + \varphi) \hat{e}_2 \quad (2.41)$$

with the laser frequencies ω_{1i} and ω_{2i} . The effective Rabi frequency between $|1\rangle$ and $|2\rangle$ is then just the multiplication of the single photon

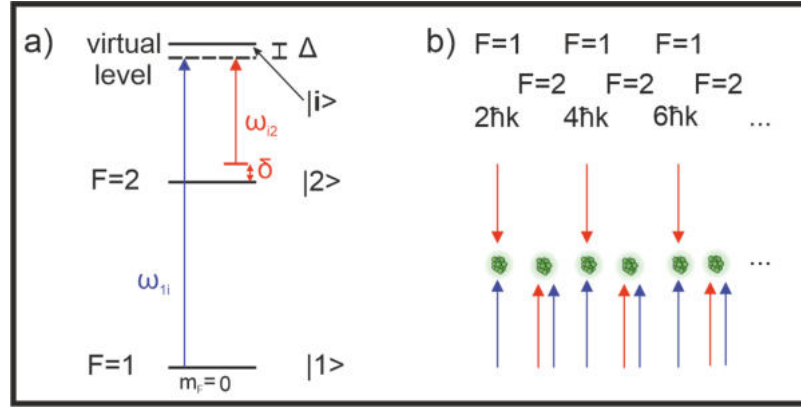


Figure 2.7: **Multi momentum Raman transfer.**

a) Level scheme for a two-photon Raman transfer in ^{87}Rb , that can transfer a momentum of $2\hbar k$ and change the clock state. Both laser couple with the frequencies ω_{1i} and ω_{i2} to a virtual level that is detuned by δ from the $5P_{3/2}$ manifold. δ is the detuning of the two clock transition states to each other, in an ideal case it is zero. b) By arranging a setup of alternating co- and counterpropagating Raman laser beams, multiple $2\hbar k$ can be transferred. The copropagating beams set the internal level of the atoms back to the starting level.

Rabi frequencies divided by two times the detuning Δ_i from the intermediate level $|i\rangle$ [38]:

$$\Omega_{eff} = \frac{\Omega_1^* \Omega_2}{2\Delta_i} \quad (2.42)$$

This is used to replace the Ω in Eq. 2.38, which leads to the probability of the two photon transfer of

$$P_e = \frac{\Omega_{eff}^2}{\Omega_R^2} \sin^2 \left(\frac{t\Omega_R}{2} \right), \quad (2.43)$$

with $\Omega_R = \sqrt{\Omega_{eff}^2 + \delta^2}$ and δ as the detuning from $|2\rangle$ to the laser frequency ω_{i2} . For an ideal Raman transfer, the detuning is $\delta = 0$. This also displays the similarity of a transfer by a Raman pulse and a transfer by a microwave pulse, with the difference that the Raman pulse can transfer a momentum of $2\hbar k$ when counter-propagating beams are used. From the first laser pulse a momentum is absorbed and the atom change to the virtual level $|i\rangle$ from the ground level $|1\rangle$. The second laser couples then the virtual level with the excited level $|2\rangle$ by stimulated emission, where another momentum is transferred. In the example in Fig. 2.6b), the atom absorb momentum in the upward direction. Then the stimulated emission emits a photon downward and due to energy conservation the atom gets a momentum in the upward direction which leads to a total of $2\hbar k$ momentum transfer.

The $2\hbar k$ are calculated by the two laser frequencies

$$\Delta p = 2\hbar k = \frac{\omega_{1i} + \omega_{i2}}{c} \quad (2.44)$$

with c as the speed of light in vacuum. With co-propagating beams, the transferred momentum is nearly zero, because the absorbed photon with the frequency ω_{1i} moves in the same direction as the emitted photon with the frequency ω_{i2} . For counter-propagating beams both photons transfer momentum in the same direction.

This can be used to transfer multiple $2\hbar k$ with a row of alternating co- and counter-propagating beams as displayed in Fig. 2.7b). Another way to reach the same effect is the use of counter-propagating beams and microwave transfers instead of the co-propagating beams. The choice between these two setups depends on the control and quality of the pulses and the existence of a microwave antenna for the microwave transfers. Also the different Rabi frequencies need to be taken into account, which depends on the power of the microwave or the Raman pulses. The increase of the Raman laser power can be limited by undesired heating effects.

FUNDAMENTAL SENSITIVITY LIMITS OF ATOM INTERFEROMETRY

In this chapter we will explore the different fundamental sensitivity limits for interferometers with atoms and how squeezing can be employed to surpass these limitations. These limits are also discussed in a context of a realistic application. At the end of this chapter, an overview over the different techniques to generate squeezing is shown and it is discussed which one is the favorite solution for an entangled-enhanced atom interferometer with inertial sensitivity.

3.1 SHOT NOISE AND DENSITY LIMIT

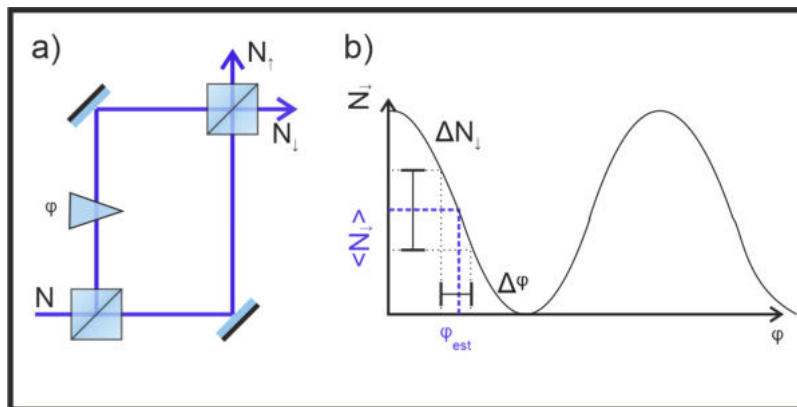


Figure 3.1: **Classical interferometer**

- a) The input port has N particles and the second input port is empty. The first beamsplitter creates a superposition of state one (upper path) and state two (right path). In the upper path, a phase shift φ is applied. Due to the second beamsplitter the both path interfere with each other. That results in a change of the mean atom number in $\langle N_{\uparrow} \rangle$ and $\langle N_{\downarrow} \rangle$ at the output ports, depending on the relative phase φ . b) Calculation of the phase from the mean particle number. The black dashed lines help to display the range of the resulting phase depending on the noise.

In a classical interferometer, the sensitivity is limited by the shot-noise limit. The origin of the shot noise can be explained by looking into a classical interferometer as in Fig. 3.1 with N uncorrelated particles. In this interferometer, the first beamsplitter transfers a particle into a superposition of the two paths, where the second input port only contains vacuum. In one path, the signal acquires a phase shift φ compared to the other path. Then the two states are combined again

at the second beamsplitter and the particle numbers in both output ports are measured. The phase difference φ translates into a particle number difference in the output ports.

The phase can be caused by different sources and the schemes are designed in a way that the quantity of interest is proportional to the phase. Therefore, a better phase estimation corresponds to a more sensitive interferometer. The phase estimation is based on the particle difference of the two output ports. The detection probability for the spin down output port can be expressed as $P_{\downarrow} = \cos^2(\frac{\varphi}{2})$. Because this translates into a particle number difference at the two output ports, the probability P_{\downarrow} can be estimated as

$$P_{\downarrow} = \frac{\langle N_{\downarrow} \rangle}{N}. \quad (3.1)$$

With this the estimated phase is calculated as

$$\varphi = 2 \cos^{-1} \left(\sqrt{P_{\downarrow}} \right) = 2 \cos^{-1} \left(\sqrt{\frac{\langle N_{\downarrow} \rangle}{N}} \right). \quad (3.2)$$

It is important to notice that this is only true modulo 2π . Therefore, the measurement steps need to be chosen in a way that the result is between 0 and 2π . However, every particle is randomly measured in one of the two output ports which causes quantum fluctuations of N_{\downarrow} and the estimated phase φ . The measurement of N_{\downarrow} follows a binomial distribution and therefore has a standard deviation of $\Delta N_{\downarrow} = \sqrt{NP_{\downarrow}(1 - P_{\downarrow})}$. This allows to calculate the phase estimation error $\Delta\varphi$ as

$$\begin{aligned} \Delta\varphi &= \left| \frac{\Delta N_{\downarrow}}{\partial_{\varphi} \langle N_{\downarrow} \rangle} \right| \\ &= \left| \frac{\sqrt{NP_{\downarrow}(1 - P_{\downarrow})}}{-N \cos(\frac{\varphi}{2}) \sin(\frac{\varphi}{2})} \right| \\ &= \left| \frac{\sqrt{N \cos^2(\frac{\varphi}{2}) \sin^2(\frac{\varphi}{2})}}{-N \cos(\frac{\varphi}{2}) \sin(\frac{\varphi}{2})} \right| = \frac{1}{\sqrt{N}}. \end{aligned} \quad (3.3)$$

This is the fundamental shot-noise limit which depends only on the particle number of the uncorrelated particles. Due to the fact that the particles are completely independent, it makes no difference if a measurement is done one time with N particles or r times with one particle(, $N = r$ for this example). Therefore a correct description would be

$$\Delta\varphi = \frac{1}{\sqrt{Nr}}, \quad (3.4)$$

for r measurements with N particles. The repetition of measurements can be employed to improve the stability, on the cost of a longer

measurement time. It still allows to overcome the technical limitations due to a limit in the particle number, because the benefit in sensitivity is higher than the loss through the longer measurement time.

This limit for uncorrelated, classical particles can be overcome by squeezing. The use of correlated particles can push the limit down to the Heisenberg limit,

$$\Delta\varphi = \frac{1}{N}. \quad (3.5)$$

DENSITY DEPENDENT SHIFT An atom interferometer can be used as an inertial sensor, by spatially separating a BEC in two clouds which experience a different gravitational potential and therefore get a relative phase shift to each other. For a highly sensitive interferometer we need the low expansion rate of a BEC and a high amount of atoms, which leads to a high density. This leads to interactions of the atoms in a BEC between N atoms in a volume V which leads to a mean field energy shift of the ground state energy proportional to $\frac{N^2}{V}$. If a momentum beam splitter is applied, each mode has its own density dependent shift. Every beamsplitter induces at least quantum fluctuations in the number of atoms and thus in the densities of the two clouds which increase $\Delta\varphi$. The effect of the density dependent shift can be modeled by the one-axis twisting Hamiltonian $H = \hbar\zeta J_z^2$ [39]. The one axis-twisting can be understood as a twisting around J_z with the strength of J_z^2 which leads to a stronger twisting as more far the point on the Bloch sphere is from the equator. For the Bose-Einstein condensates in this thesis $\hbar\zeta = \frac{U}{V}$ is valid, with $U = 4\pi\hbar^2 \frac{a_s}{m}$, where a_s is the scattering length of the atoms and m is the mass [40]. The twisting effect is explained in more detail in the following section and also shown on the Bloch spheres in Sec. 4.3.

3.2 PHASE, NUMBER AND OPTIMAL SQUEEZING

In this section, we will analyze the effect of squeezing on the shot noise limit and the influence of the density dependent shifts. We will deduce an optimal choice of squeezing to counteract the density effect.

In Fig. 3.2, different states are displayed, the chosen plane is the J_y, J_z -plane of a Bloch sphere description with the J_x -axis as the rotation axis. This is the tangential plane to the J_x -axis, which allows us an approximation of the 3-D surface of the Bloch sphere into a 2-D description. This is the position of our state after the first beamsplitter in an interferometer, where it then collects a phase during the evolution time. The phase is collected in the J_y direction, therefore the fluctuation ΔJ_y should be minimal. In this description, the one-axis twisting twists every point in the J_y, J_z -plane depending on its distance to the J_y -axis, which can be explained with Fig. 3.2b). There it is shown that the part of the state with $J_z = 0$ does not change, but the outer ends

of the ellipse move the most. The twisting is $\propto J_z^2$. Now we want to analyze how that can be used to improve our interferometer in the presence of a density shift. This can be modeled by the one-axis twisting Hamiltonian $H = \hbar\xi J_z^2$ [39], with $\mu = 2\xi T$ or $\mu = 2 \int_0^T dt \xi(t)$ as the strength of the density effect. For a uniform BEC it is $\hbar\xi = \frac{U}{V}$ and $U = 4\pi\hbar^2 a_s/m$ with a_s as the scattering length of the atoms and m as the mass of the atoms [40]. This allows to describe the sensitivity with Eq. 2.14 combined with

$$e^{-iHT/\hbar}|\Psi\rangle, \quad (3.6)$$

if H is time independent.

In Fig. 3.2a), a coherent state is shown in blue as a circle. The uncertainty is equal on both axes for the classical state. The green dashed line shows the influence of the density effect, which twists the coherent state into a diagonal ellipse. This increases the phase measurement uncertainty $\Delta\varphi$ which is proportional to the uncertainty along J_y , with

$$\Delta\varphi = \frac{\Delta J_y}{\langle J_x \rangle} = \frac{\Delta J_y}{\frac{N}{2}}. \quad (3.7)$$

The perfect squeezing for a small phase estimation error without density effect is now the so-called phase squeezing shown in Fig. 3.2b) as the blue ellipse. The name comes from the minimal phase estimation error of the generated state. However, due to the density effect, the ellipse is twisted into the green dashed ellipse which displays the incoupled noise from the J_z direction. Therefore, the phase measurement uncertainty even increases compared to the values of a twisted coherent state. To avoid the effect of the density twisting, a number squeezed state can be used, where the number uncertainty is minimal as shown in Fig. 3.2c). In this case, the twisting indeed barely affects the state. However, it is already anti-squeezed in the phase direction and this extra noise makes it less useful for an interferometer.

By choosing an optimal squeezing phase in between number and phase direction (Fig. 3.2d)), where the initial phase uncertainty is not ideal (blue ellipse), the density effect counteracts the original squeezing rotation and leads to a perfect squeezing orientation (green dashed ellipse). That leads to an optimal squeezing value with a minimal phase uncertainty similar to the unaffected phase squeezing ellipse. If the squeezing phase is $\theta = 0$ for phase squeezing and π for density squeezing, the optimal phase θ_{opt} can be calculated by

$$\tan\theta_{opt} = \frac{4\mu N}{4 - \mu^2 N^2}. \quad (3.8)$$

This equation is derivated from the density effect, which leads to the evaluation

$$U = e^A, \quad A = -i\frac{\mu}{2}J_z^2. \quad (3.9)$$

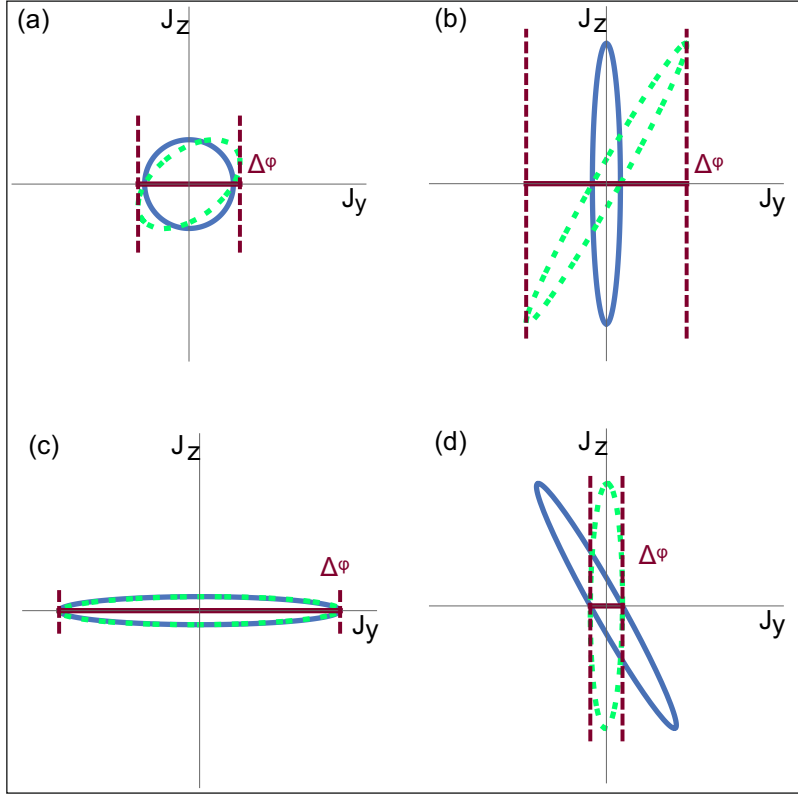


Figure 3.2: **Different kinds of squeezing**

- a) Coherent state: the blue line shows the state on the J_y, J_z tangential plane to the Bloch sphere without density effect, respectively with the green dashed line for the density effect. The measured phase uncertainty $\Delta\varphi$ is displayed by the horizontal purple dashed lines.
 b) Phase squeezing c) Density squeezing d) Optimal squeezing

If all atoms in the mode a , all atoms are in a coherent state along J_x . Then the mean field approximation for J_z can be written, as

$$J_z \approx \frac{\sqrt{N}}{2i} (b - b^\dagger). \quad (3.10)$$

In this approximation we can apply the calculus for single-mode Gaussian states. The matrix elements of B are defined as

$$B = \begin{pmatrix} b^2 & bb^\dagger \\ b^\dagger b & (b^\dagger)^2 \end{pmatrix}. \quad (3.11)$$

Then

$$J_z^2 = -\frac{N}{4} (b^2 - b^\dagger b - bb^\dagger + (b^\dagger)^2) \quad (3.12)$$

follows, which leads to

$$-iKA = -i\frac{\mu N}{8} \begin{pmatrix} 1 & -1 \\ 1 & -1 \end{pmatrix} \quad (3.13)$$

with

$$K = \begin{pmatrix} 1 & 0 \\ 0 & -1 \end{pmatrix}. \quad (3.14)$$

We can then use a real symplectic transformation [41] that refers to the quadrature operators by

$$L = \frac{1}{\sqrt{2}} \begin{pmatrix} 1 & 1 \\ -i & i \end{pmatrix}, \quad (3.15)$$

with

$$\begin{pmatrix} q \\ p \end{pmatrix} = \frac{1}{\sqrt{2}} \begin{pmatrix} a + ia^\dagger \\ -ia + a^\dagger \end{pmatrix} = L \begin{pmatrix} a \\ a^\dagger \end{pmatrix}, \quad (3.16)$$

to gain the symplectic matrix $S = LS_cL^\dagger$. For that we use the complex symplectic matrix S_c ,

$$S_c = e^{-iKA} = \begin{pmatrix} 1 & 0 \\ 0 & 1 \end{pmatrix} - i\frac{\mu N}{8} \begin{pmatrix} 1 & -1 \\ 1 & -1 \end{pmatrix}. \quad (3.17)$$

This leads to

$$\begin{aligned} S &= LS_cL^\dagger \\ &= \begin{pmatrix} 1 & 0 \\ 0 & 1 \end{pmatrix} - i\frac{\mu N}{8} \begin{pmatrix} 1 & 1 \\ -i & i \end{pmatrix} \begin{pmatrix} 1 & -1 \\ 1 & -1 \end{pmatrix} \begin{pmatrix} 1 & i \\ 1 & -i \end{pmatrix} \end{aligned} \quad (3.18)$$

$$= \begin{pmatrix} 1 & 0 \\ 0 & 1 \end{pmatrix} + \frac{\mu N}{2} \begin{pmatrix} 0 & 1 \\ 0 & 0 \end{pmatrix}, \quad (3.19)$$

which is a symplectic matrix, which fulfills the relation

$$S\Omega S^T = \Omega, \quad (3.20)$$

with

$$\Omega = \begin{pmatrix} I_n & 0 \\ 0 & -I_n \end{pmatrix}, \quad (3.21)$$

where I_n is the identity matrix of the size n [41]. In this case we use $n = 1$. A squeezed vacuum state

$$|\psi(t)\rangle = S(\xi)|0\rangle \quad (3.22)$$

leads to an operator σ [41], the variance of the Gaussian state,

$$\sigma = \cosh(2s) \begin{pmatrix} 1 & 0 \\ 0 & 1 \end{pmatrix} + \sinh(2s) \begin{pmatrix} \cos(\theta) & \sin(\theta) \\ \sin(\theta) & -\cos(\theta) \end{pmatrix}. \quad (3.23)$$

The derivation is shown in the appendix A.1. The squeezed vacuum state will be explained in detail in the next chapter. This leads together to

$$\begin{aligned}
\tilde{\sigma} &= S\sigma S^T \\
&= \cosh(2s)SS^T + \sinh(2s)S \begin{pmatrix} \cos(\theta) & \sin(\theta) \\ \sin(\theta) & -\cos(\theta) \end{pmatrix} S^T \quad (3.24) \\
&= \cosh(2s) \left(\begin{pmatrix} 1 & 0 \\ 0 & 1 \end{pmatrix} + \frac{\mu N}{2} \begin{pmatrix} 0 & 1 \\ 1 & 0 \end{pmatrix} + \frac{\mu^2 N^2}{4} \begin{pmatrix} 1 & 0 \\ 0 & 0 \end{pmatrix} \right) \\
&\quad + \sinh(2s) \left(\begin{pmatrix} \cos(\theta) & \sin(\theta) \\ \sin(\theta) & -\cos(\theta) \end{pmatrix} \right. \\
&\quad \left. + \frac{\mu N}{2} \begin{pmatrix} 2 \sin(\theta) & -\cos(\theta) \\ -\cos(\theta) & 0 \end{pmatrix} + \frac{\mu^2 N^2}{4} \begin{pmatrix} -\cos(\theta) & 0 \\ 0 & 0 \end{pmatrix} \right) \quad (3.25)
\end{aligned}$$

The perfect squeezing phase is derived from $\tilde{\sigma}_{11}$ 3.25, which corresponds to $\Delta^2 J_z$. Its θ dependent part is

$$f(\theta) = \cos(\theta) - \frac{\mu^2 N^2}{4} \cos(\theta) + \mu N \sin(\theta). \quad (3.26)$$

$\tilde{\sigma}_{22}$ would describe the measurement in J_z -direction. The minimum of this function is then

$$\begin{aligned}
\frac{d}{d\theta} f(\theta) &= - \left(1 - \frac{\mu^2 N^2}{4} \right) \sin(\theta) + \mu N \cos(\theta) = 0 \\
\Rightarrow \frac{\sin(\theta)}{\cos(\theta)} &= \frac{\mu N}{\left(1 - \frac{\mu^2 N^2}{4} \right)}, \quad (3.27)
\end{aligned}$$

which is the optimal squeezing phase. The resulting sensitivity is far better than for an unsqueezed state. It is slightly worse than for a phase squeezed state without density effect because the density effect affects not only the squeezing phase but also its amplitude, as shown in Fig. 3.2d). The proposed method thus constitutes a viable path to make use of squeezed atomic samples in the experimentally relevant cases, where density effects can not be neglected.

3.3 REALISTIC APPLICATION

In a realistic application, the constraints for an interferometer are not only set by the fundamental limits, they are also set due to experimental restrictions. By using BECs with delta-kick collimation, the expansion rates can be held on the level of 100pK and below [42] which reduces the constraints on the beamsplitting laser diameter and the detection system. In this analysis, the noise sources taken into account are quantum phase noise, gravity gradients of the atomic

ensemble, coupling of rotations and interactions that can affect the differential signal [43–46]. That is calculated for a shot-noise limited position $\Delta r/\sqrt{N}$ and velocity uncertainty $\Delta v/\sqrt{N}$. It needs to be taken into account that the dependency of T^3 of the noise sources increase the noise for longer baseline interferometer, where T as the evolution time is increased to reach a higher sensitivity.

The density shift depends of the amount of atoms per volume, therefore also the standard density limit (SDL), the best reachable limit in the presence of density effects, depends on the amount of atoms.

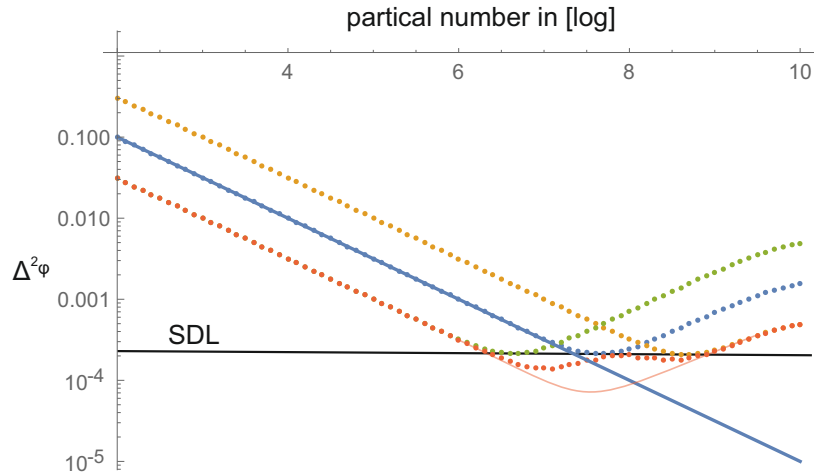


Figure 3.3: **Density depending squeezing**

The blue dots are a coherent state with density effect. The light blue line shows the coherent state without density effect. The yellow dots are a number squeezed state which starts with the highest $\Delta\varphi$ and the green dots are a phase squeezed state. The red dots are the optimal squeezed state in the presence of density effects, the light red line shows the optimal squeezing without the effect of inhomogeneity.

Calculated with a squeezing of 10dB as an example.

In Fig. 3.3 are four different states displayed, all under the influence of density effects. Starting with a coherent spin state (blue dots) which follows the shot noise scaling, by reducing the phase uncertainty $\Delta\varphi$ with an increase in the atom number N at a fixed volume. The increase of the uncertainty is then the effect of the mean-field interactions, which fluctuate due to shot-noise. This will be now the limit that we want to surpass with squeezed states and we call it the standard density limit (SDL). The scaling without density effect is shown by the light blue line. If we take a density squeezed state (yellow dots), it is worse than the classical state for a lower number of atoms but better than the classical state for a higher number of atoms. That is clear according to Fig. 3.2c), where it is shown that the density effect barely effects the state. Nevertheless, the minimal phase uncertainty is just the same as for a coherent state, only at a higher number of

atoms. The phase squeezed state (green dots) has the same shape as the number squeezed state but now starting at the same point as the optimal squeezing, but the density effect influence the state at a lower atom number than a coherent state. Therefore, it would be better for lower atom numbers but also have a minimal phase variance as the coherent state only at a lower atom number, which is normally beneficial in experiments with a limited amount of atoms.

Only with the optimal squeezing, it is possible to reach the best phase uncertainty $\Delta\varphi$ below the standard density limit. As shown in Fig. 3.3, the optimal squeezing (red dots) follows the phase squeezing for low atom number and the density squeezing for high atom numbers. I will now focus on the intermediate area, where also the standard density limit is violated. This operation needs a mostly homogeneous density profile for the BEC. This limits the noise suppression below the SDL, as shown in the comparison of the light red line and the red dots in Fig. 3.3. This can be avoided by restricting the readout of the interferometer to high-density regions. That will slightly reduce the number of analyzed atoms, which is equivalent to a small shift to the left in Fig. 3.3, which would still lead to a better result than with the inhomogeneity. But even with the inhomogeneity a measurement below the SDL is possible.

3.4 METHODS FOR GENERATING SQUEEZING

For the generation of meteorologically useful entanglement with atoms, two different paths have been demonstrated experimentally: atom-light interaction and atomic collisions.

Atom-light interaction was used to generate spin-squeezed states or W states in laser-cooled samples [15–17, 47] and in gas cells [18, 19]. The current record value in squeezing of 20.1dB below shot noise has been reached by exploiting the coupling between an atomic ensemble and the light field of a cavity which is placed around it [20]. All these methods are only applied to thermal ensembles and not to Bose-Einstein condensates. BEC sources are favorable for achieving highest precision in large scale atom interferometers due to the lower expansion rate. In addition, the use of an optical cavity constrains the optical and mechanical access to the atoms for the rest of the experimental setup. Therefore, I will now look deeper into the the second method of entanglement generation.

The collisional interaction in a BEC can be described as a nonlinear process for the generation of entangled states. As an example, this technique can be used to generate entangled states on the external degrees of freedom, that are desired for an interferometer. The creation of entangled momentum pairs was demonstrated with Helium [10, 11, 48] and Rubidium [12]. The latter is a more commonly used element in BEC interferometers. In these experiments, the temporal coherence

and the mode quality of the entangled states is quite low, because the entangled states are created as a stream of entangled atom pairs. Therefore, they will be neglected for the further process. It is also possible to generate spatial entanglement between the two spatially separated modes of a double well potential [13, 14]. Such a scheme has the problem of addressing the two spatial modes independently from each other to transfer these state into the input ports of an momentum interferometer without destroying the entanglement during that process.

Therefore, the most promising approach for inertially sensitive atom interferometry is the generation of entanglement in spin space and transferring it to the external degrees of freedom for the momentum interferometer. This can be done by well-known techniques like Bragg or Raman laser transfers, as explained in Sec. 2.4.2. For this thesis I will use the Raman transfer as explained before. Being independent in the creation process of the interferometer states and the momentum interferometer itself allows for a greater freedom in the design of the interferometer scheme. The entanglement in the spin squeezed domain can be generated in the basis of one-axis twisting (OAT), which uses the collisional properties of two spin states [21, 22]. An alternative to this method is the generation of entanglement by using spin changing collisions (SCC) which can generate spin-squeezed states [9, 25–27] or twin-Fock states [24, 49].

To use one-axis twisting to generate entangled states, the collisional interaction needs to be precisely modulated, which can be done by Feshbach resonances [21]. Therefore, we would need to operate comparably high magnetic fields, which is an unwanted complication. Another method, controlling the mode overlap [22], is not favorable as a generation method for an entanglement-enhanced interferometer. The required spacial splitting process can easily destroy the mode quality of the squeezed atomic clouds. In this thesis, the focus will be on the second method, the generation of entanglement with spin changing collisions. The entanglement is generated in three atomic spin states and then the desired states are selected and manipulated in a way that they are useful for a momentum-space atom interferometer. The process of generating spin squeezed states and twin-Fock states is described in Ch. 4.

GENERATION OF SQUEEZING IN SPINOR BECS

In this chapter, spin squeezing and the states that are generated by this will be described theoretically and from an experimental point of view. We use spin-changing collisions in ^{87}Rb BECs to generate multi-particle entangled states. These states can be used as squeezed input states for the interferometer sequences. The introduced states are the twin-Fock state and the two-mode squeezed vacuum state. Those can be implemented in an entangled interferometer, as well.

4.1 SPINOR BECS

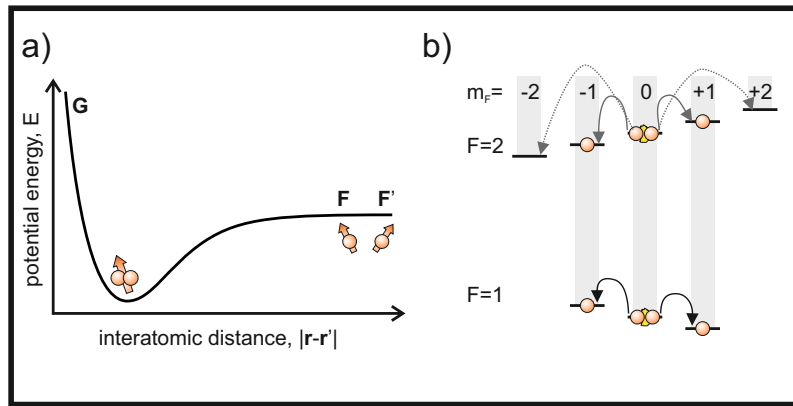


Figure 4.1: Spin changing collisions.

a) At long inter atomic distances $|r - r'|$ the internal states of cold ^{87}Rb atoms are described by the hyperfine spins F and F' . At a small interatomic distance they are described by the total spin $G = F + F'$. The molecular potential and the scattering length a_G are depending on the total spin. b) ^{87}Rb energy level scheme. Colliding atoms in $F = 0, m_F = 0$ can be transferred into $m_F = \pm 1$ under energy conservation. The same is possible in $F = 2, m_F = 0$, with the additional possible transfer into $m_F = \pm 2$. However, this process is suppressed by orders of magnitude.

At low magnetic fields of a few Gauss, the internal state of a ^{87}Rb atom can be described by the hyperfine spin \vec{F} with its length $|\vec{F}| = \sqrt{F(F+1)}$. Its projection onto the magnetic field axis is m_F , the magnetic quantum number for the hyperfine states. The ^{87}Rb atom can be in one of the two hyperfine manifolds $F = 1$ or $F = 2$ with the corresponding projections onto the magnetic field $m_F = F, F - 1, \dots, -F$. The different m_F -states split up in a magnetic field due to the Zeeman effect. If two atoms in the hyperfine states F and F' approach each

other in an atomic collision this description stops to work. The atoms are then described by a total spin $\vec{G} = \vec{F} + \vec{F}'$ with an internal state of $|G, m_G\rangle$ as shown in Fig. 4.1a). During that phase, interactions between the atoms can lead to a coupling of the two hyperfine spins $|F, m_F\rangle$ and $|F', m'_F\rangle$ to a different output channel $|\bar{F}, m_{\bar{F}}\rangle$ and $|\bar{F}', m'_{\bar{F}}\rangle$. This could lead to a change of the quantum numbers

$$|F, m_F\rangle|F', m'_F\rangle \rightarrow |\bar{F}, m_{\bar{F}}\rangle|\bar{F}', m'_{\bar{F}}\rangle. \quad (4.1)$$

If the interaction changes the hyperfine manifold from $F = 2$ to $F = 1$, a large amount of energy is set free which leads to a loss of atoms from the ensemble. This loss mechanism can be avoided experimentally by using the spin dynamics in the $F = 1$ manifold. Therefore, we assume that the hyperfine manifold does not change ($F = F' = \bar{F} = \bar{F}'$). Due to the ultra cold temperature of a BEC, only s-wave scattering can occur [50], therefore the total orientation of the angular momentum needs to be preserved, $m_F + m'_F = \bar{m}_F + \bar{m}'_F$. After the interaction during the collision, they can separate and are then described again by the hyperfine spin \vec{F} for a single atom. We call that then a spin-changing collision.

If the spin dynamics start with all atoms in the $m_F = m'_F = 0$ state, only the dynamics shown in Fig. 4.1b) are possible.

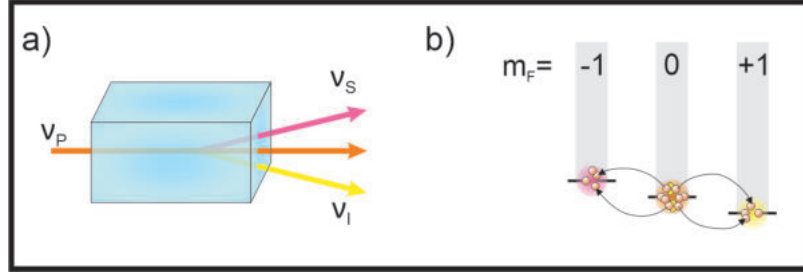


Figure 4.2: **Parametric down conversion analogue.**

a) For the process of parametric down conversion, a strong pump beam with the frequency ν_p is passing a nonlinear crystal. The non-linearity of the crystal generates entangled photons in the signal and idler beams with frequencies ν_s and ν_i . b) Spin changing collisions is an analogue in the particle domain. The strong pump is the BEC in $m_F = 0$ and the non-linearity is the spin changing collision. Then the modes $m_F = \pm 1$ are populated in analogy to the signal and idler beam.

As an example for the starting state for the spin dynamics, the $|F = 1, m_F = 0\rangle$ state is chosen, which only allow one combination spin exchange process. This process is pretty similar to the parametric down conversion from optics and it produces entangled atoms in the output modes. Parametric down-conversion is one of the most relevant methods in optics to generate entangled photons [51]. In the process of parametric down-conversion, a strong pump beam with

the frequency ν_p passes a non-linear crystal. The non-linearity leads to the creation of a signal and an idler beam with the frequencies ν_s and ν_i which have to fulfill the energy conservation $\nu_p = \nu_s + \nu_i$. As shown in Fig. 4.2a), the beams also have a geometrically different path. These two beams are highly entangled and can be used for various tasks like a quantum repeater, Bell tests and many more applications in quantum information [51]. Single-mode squeezed light can be produced by selecting $\nu_s = \nu_i = \frac{\nu_p}{2}$ [52], which can be employed for interferometric measurements beyond the shot-noise limit [53].

An analog for cold atoms is spin dynamics, which allows the creation of non-classical entangled states in the internal degrees of freedom of the atoms, an example for ^{87}Rb is shown in Fig. 4.2b). The ^{87}Rb BEC with all atoms in $m_F = 0$ ($F = 1$ or $F = 2$) can be treated as the analog of the pump beam. The spin changing collisions are fundamentally non-linear and therefore the analog of the down-conversion process in the crystal. As explained before, the atoms are only described by a total spin G during the collisions. Therefore it is indistinguishable which atoms are transferred to $m_F = +1$ and which to $m_F = -1$. The atoms that are transferred into the $m_F = \pm 1$ levels of the corresponding F manifold are then highly entangled and the analog of the signal and idler beam in the special case of squeezed light.

Like in the optical case, the amplification can be triggered by a seed in these energy levels or vacuum fluctuations [54, 55], where the seed would amplify the speed of the spin dynamics.

The vacuum fluctuations in optics stem from fundamental fluctuations in the electromagnetic field, the vacuum fluctuations during the process of spin dynamics origin from the fundamental fluctuations of the spin orientation that was explained in Sec. 2.1. In the next section, it will be shown that spin dynamics can be described by the same Hamiltonian as parametric down conversion for short times.

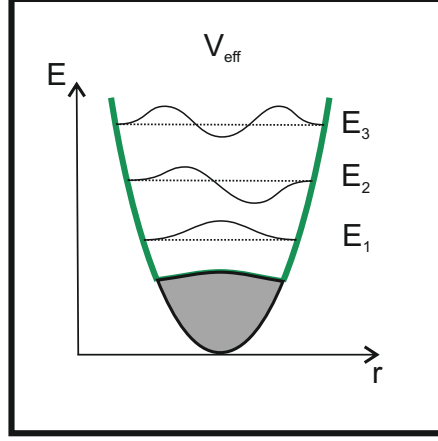
4.2 GENERATION OF ENTANGLEMENT

In this section, I will explain first the theoretical part of the entanglement generation and then two different experimental ways to generate entanglement in a BEC.

We will assume that we start the process of spin dynamics in the $|1, 0\rangle$ state and that the atoms are in a BEC in an external trapping potential. This is needed to reach a sufficient high density that the spin changing collisions happen. The potential can be described as

$$V_{eff}(r) = V_{ext}(r) + (U_0 + U_1)n_0(r) - \mu, \quad (4.2)$$

with $V_{ext}(r)$ as the external trapping potential (green/black parabola in Fig. 4.3) and μ as the chemical potential. The chemical potential μ shifts the energy of two atoms in the $m_F = 0$ state to zero. The term $(U_0 + U_1)n_0(r)$ describes the mean field interactions of two atoms in

Figure 4.3: **Effective potential.**

The effective potential (green line) for the atoms in $m_F = \pm 1$ is the sum of the external trap potential (black parabola) and the repulsive mean field interaction with the atoms in $m_F = 0$. The potential has many eigenenergies E_n (dashed lines) with their corresponding eigenstates (black curves).

$m_F = 0$ with $n_0(r)$ as the particle density operator for atoms in $m_F = 0$. U_l is a 2-particle interaction operator with $l = 0, 1, 2$. U_0 describes the energy scale of a collision of two atoms in $m_F = 0$ without a change of the m_F state and U_1 describes the collisions of two atoms and a change of the m_F state to $m_F = +1$ and $m_F = -1$ from $m_F = 0$ and vice versa. Calculated example values can be found in Ref. [28]. The graph shows the repelling effect of the mean field interaction as the gray area in the graph. Also the eigen energies E_n as the energies of the effective trapping potential are shown.

The interactions of spin dynamics can then be described by a many body-Hamiltonian H , which can be written as

$$H = (E_n + q)(N_{+1} + N_{-1}) + 2CU_1 \left(a_0^\dagger a_0^\dagger a_{+1} a_{-1} + a_{+1}^\dagger a_{-1}^\dagger a_0 a_0 \right). \quad (4.3)$$

N_{+1} and N_{-1} are the number of atoms in $m_F = \pm 1$, $a_{m_F}^\dagger$ is the creation operator for the respective m_F state and a_{m_F} is the annihilation operator. The Hamiltonian has two different parts.

The first part $(E_n + q)$ describes the interaction of the eigenmodes of the trapping potential and the energy difference $2q$ between two atoms in $m_F = 0$ compared to a pair in $m_F = +1$ and $m_F = -1$. q depends on the quadratic Zeeman effect, therefore is $q \propto B^2$ with B as the strength of the magnetic field. This energy difference can be manipulated experimentally to generate entangled states, which will be shown in the next subsections.

The second part describes the spin changing collisions. C is the spatial overlap integral

$$C = \int \phi_{+1}^*(r) \phi_{-1}^*(r) \phi_0(r) \phi_0(r) dr, \quad (4.4)$$

with ϕ_j as the wave function of the different m_F states. The first part of the bracket describes the annihilation of an atom in $m_F = +1$ and $m_F = -1$ each and the generation of two atoms in $m_F = 0$. The second part describes the reverse process.

In the resonance case, with $E_n = -q$, the first part of the Hamiltonian is zero and only the interacting term

$$H_{int} = 2CU_1 \left(a_0^\dagger a_0^\dagger a_{+1} a_{-1} + a_{+1}^\dagger a_{-1}^\dagger a_0 a_0 \right) \quad (4.5)$$

remains. That makes it easier to calculate the time evolution for this case. By using the approximation $a_0 = \sqrt{N}$ for large N with $N_0 \approx N$ we can rewrite the Hamiltonian as

$$H_{int} = \Omega \left(a_{+1} a_{-1} + a_{+1}^\dagger a_{-1}^\dagger \right), \quad (4.6)$$

with $\Omega = 2CU_1 N_0$ as the spin dynamics rate. That would lead to the two-mode squeezed vacuum operator

$$\begin{aligned} U(t) &= e^{-itH_{int}} \\ &= e^{-i\zeta(a_{+1}a_{-1} + a_{+1}^\dagger a_{-1}^\dagger)} = S(\zeta), \end{aligned} \quad (4.7)$$

with $\zeta = t\Omega$ which is then the same as the one in quantum optics [29].

Now we want to calculate the time evolution of the spin dynamics for the general case. The Heisenberg equation for time evolution reads

$$\begin{aligned} i \frac{d}{dt} a_{+1} &= [H, a_{+1}] = -(E_n + q)a_{+1} + i\Omega a_{-1}^\dagger \\ i \frac{d}{dt} a_{-1}^\dagger &= [H, a_{-1}^\dagger] = (E_n + q)a_{-1}^\dagger + i\Omega^* a_{+1}. \end{aligned} \quad (4.8)$$

with $\hbar = 1$. These couple of connected equations can be solved by a Bogoliubov transformation [56] and leads to the new operators

$$b_\pm(t) = e^{\mp i t \lambda} b(0) = u a_{\pm 1}(t) + v a_{\mp 1}^\dagger(t), \quad (4.9)$$

with $(u, v)^T$ as the eigenvector of the coupled equations. This new operator can be used to describe the time evolution of $a_{\pm 1}$. The eigenvalues are

$$\lambda = \pm \sqrt{(E_n + q)^2 - |\Omega|^2}, \quad (4.10)$$

following from the solution of

$$(-E_n - q - \lambda)(-E_n - q - \lambda) = -|\Omega|^2. \quad (4.11)$$

These eigenvalues λ can be completely imaginary and reach the maximal instability at resonance $E_n = -q$, where the spin changing is fastest. But the instability $\text{Im}(\lambda)$ is then a half circle around E_n with a radius of $|\Omega|$, for every E_n . That can be understand as an non infinitesimal small resonance peak, which would allow to start spin dynamics

with a non-perfect shifting of q . There are an infinity amount of energy levels and therefore a multi-peak structure of resonances.

This is one explanation why we start in the $|1, 0\rangle$ state, because Ω depends on U_1 which smaller in the $F = 1$ manifold compared to the $F = 2$ manifold, which allows a better separation of the different resonance peaks. This allows a spin dynamic only in the energy ground state without the excitation of higher modes. The higher modes can be excited by detuning the q value [57].

4.2.1 Two-mode squeezed vacuum states

Now let's look more into the details of a squeezed vacuum state. As it was explained in the section before, the operator for the time evolution of spin dynamics at resonance is the same as a two-mode squeezing operator $S(\xi)$.

With all atoms in $m_F = 0$ at the start, there are no atoms in $m_F = \pm 1$ and there is a vacuum state in both levels $|N_{+1}, N_{-1}\rangle = |0, 0\rangle$, which evolves to

$$|\psi(t)\rangle = S(\xi)|0, 0\rangle \quad (4.12)$$

[29]. Be aware that I changed the definition of the BraKet to $|N_{+1}, N_{-1}\rangle$ for this section. Now let's look at the mean number of atoms that are transferred to the $m_F = \pm 1$ states, $\langle N_+ + N_- \rangle = \langle a_{+1}^\dagger a_{+1} + a_{-1}^\dagger a_{-1} \rangle$. As shown before the time evolution of the bosonic operator $a(t)$ can be obtained through the Bogoliubov transformation with $-q = E_n$ for the resonance condition. The time evolution of $a_{+1}(t)$ can be described by using Eq. 4.9 as

$$\begin{aligned} a_{-1,+}(t) &= \frac{1}{2} \left(a_{+1}(t) + a_{-1}^\dagger(t) \right) = e^{|\Omega|t} a_{-1,+}(0) \\ a_{-1,-}(t) &= \frac{1}{2} \left(a_{+1}(t) - a_{-1}^\dagger(t) \right) = e^{-|\Omega|t} a_{-1,-}(0). \end{aligned} \quad (4.13)$$

The solution is then

$$a_{+1}(t) = a_{-1,+}(t) + a_{-1,-}(t) = \cosh(|\Omega|t) a_{+1} + \sinh(|\Omega|t) a_{-1}^\dagger. \quad (4.14)$$

Therefore the time evolution of the number operator is

$$\begin{aligned} \langle N_{+1}(t) \rangle &= a_{+1}^\dagger(t) a_{+1}(t) \\ &= \cosh^2(|\Omega|t) a_{-1}^\dagger a_{-1} \\ &\quad + \cosh(|\Omega|t) \sinh(|\Omega|t) [a_{+1}^\dagger a_{-1}^\dagger + a_{+1} a_{-1}] \\ &\quad + \sinh^2(|\Omega|t) a_{-1} a_{-1}^\dagger. \end{aligned} \quad (4.15)$$

The result for a vacuum state with $\langle a_{+1}^\dagger a_{+1} \rangle = \langle a_{-1}^\dagger a_{-1} \rangle = \langle a_{+1} a_{-1} \rangle = \langle a_{+1}^\dagger a_{-1}^\dagger \rangle = 0$ is then

$$\langle N_{+1}(t) \rangle = \sinh^2(|\Omega|t). \quad (4.16)$$

The change in the population for short evolution times t behave to an exponential growth at the beginning of the evolution time. This description can be used to approximate the necessary time to generate the spin squeezed states. Keep in mind that it only works for small evolution times before the saturation effect starts and not for the long evolution times necessary for the twin-Fock state. The atoms in $m_F = \pm 1$ are produced in pairs which makes it obvious that $\langle N_{+1}(t) \rangle = \langle N_{-1}(t) \rangle$.

The two mode squeezed state is the same for atoms as for optics [29]

$$|\psi\rangle = \sum_{n=0}^{\infty} \frac{(-i \tanh(\xi))^n}{\cosh(\xi)} |n, n\rangle, \quad (4.17)$$

generated with help of Eq. 4.12. We can see here, that it is a superposition of twin-Fock states with different total atom number, but with the exact same amount of atoms in the $m_F = \pm 1$ states.

Pair production can be experimentally realized by tuning the q parameter. To do that the energy difference between the $m_F = \pm 1$ and $m_F = 0$ levels is shifted such that $E_n = -q$ for $n = 0$. The shift is done by microwave coupling as described in Ch. 2, on the $F = 1, m_F = -1$ to $F = 2, m_F = -2$ coupling. This coupling is chosen, for experimental reasons. Normally no atoms are transferred at this level pair and also a mislead transfer can easily be observed. The microwave frequency is ramped to the resonance and then kept there to transfer atoms by spin dynamics into the $m_F = \pm 1$ levels, a so called "quench". For a squeezed vacuum state, only a minor percentage needs to be transferred. Therefore, the dressing is only active for 675 μs , which transfers around 0.75 atoms from 10000 atoms by spin dynamics, which is enough for a two-mode squeezed vacuum state [9]. In this state the squeezing is between the quadratures of the sum and the differences of the atom numbers in $m_F = \pm 1$. We can change the description by a base change to have again the picture of single mode squeezing. The new base is the symmetric and the antisymmetric mode

$$|S\rangle = \frac{1}{\sqrt{2}} (|1, +1\rangle + |1, -1\rangle) \quad (4.18)$$

$$|AS\rangle = \frac{1}{\sqrt{2}} (|1, +1\rangle - |1, -1\rangle). \quad (4.19)$$

The squeezed vacuum state is observed in an 3-mode system, now made out of the $|0\rangle, |S\rangle$ and $|AS\rangle$ state.

4.2.2 Twin-Fock states

On the twin-Fock time scale, the ensemble is ideally transferred completely into the $m_F = \pm 1$ levels with the same amount of atoms in

each level. In an ideal case, also the total atom number N would be every time the same, due to fluctuations in the total atom number that is not the case. This can be described by a superposition of twin-Fock states due to the different amount of atoms pairs that are generated during each spin dynamic process. The total atom number after each sequence is detected, therefore it can be described by single twin-Fock states with a defined number of atoms.

The generation of entanglement is the same as for the squeezed vacuum, but now we disregard the atoms in the $|0\rangle$ state to have a pure two-mode system again. The experimental generation can be done in two slightly different ways. The first way is the same as in the sequence for the two-mode squeezed vacuum state: The "quench", only that now the dressing is active for a longer time about 200ms to generate the maximum amount of atom pairs in the $m_F = \pm 1$ levels. The process of a quench is fast compared to the next method but the resulting amount of atom pairs depends on the vacuum fluctuations which leads to large variances in the total number of pairs. This increases the amount of measurements that need to be done if a certain amount of measurement points of a defined number of atoms should be measured.

The second way is a ramp of the dressing over the resonance frequency [24, 58]. This is an adiabatic passage which allows for nearly 100% transfer into the $m_F = \pm 1$ levels and therefore a lower variance of the atom numbers in the twin-Fock state. The disadvantage of this method is the rather long time of 3s, which leads to decoherence due to the limited life time of the BEC and the heating by the dipole trap. For that reason, a compromise between maximum transfer and holding time need to be found for our setup. In our experiment, we normally use a ramp with 1s length. That transfers the majority of the atoms, reduce the variance in the number of atoms in the twin-Fock state and still gives us enough coherence to perform the different interferometer sequences afterwards.

4.3 GEOMETRIES FOR ENTANGLED ATOM INTERFEROMETERS

The section before provided the description of producing entanglement with spin dynamics in ^{87}Rb BECs. For a measurement of the acceleration of earth the atom interferometer have to be in the external degrees of freedom to have the access to the difference in gravitational potential. Therefore, the BEC will be free falling during the interferometer sequence, after the preparation of the state on the internal states in the trapping potential. Now, the experimental restrictions and the assumptions that we make will be explained and two different concepts of entangled atom interferometers for acceleration measurements will be presented.

In an ideal case the state is optimally entangled, the free fall time is long and the beam splitting pulses transfer as much momentum in units of $\hbar k$ as possible. But in reality, all three parameters have restrictions that need to be taken into account when planning an entangled-atom interferometer. For the first point of optimal entanglement for the input state, the technical noise needs to be as low as possible. A detailed view on the noise sources in our experiment is shown in Sec. 5.3. The evolution time T for the interferometer is limited in many experiments by the free fall time of the atomic ensemble. This is directly connected to the length of the vacuum chamber. As example values, our experiment allows us a free fall time of $11ms$, an experiment with an $1m$ vacuum chamber for the free fall will have a free fall time of around $0.45s$ and a long baseline experiment like the Very Long Baseline Atom Interferometry (VLBAI) in Hannover with a Baseline of $10m$ will have a free fall time of $0.8s$ to $2.8s$ depending on the configuration (free fall vs catapult mode) [59].

A well known source for high-momentum beam splitter pulses is double Bragg diffraction which requires a strong optical lattice that is far detuned to the resonance frequency of the atoms. This is a 2-photon process. This could also be combined with Bloch oscillations for more momentum transfer, which was shown with up to $1008\hbar k$ [35]. However, we will use a Raman transfer for the schemes due to our way to generate entanglement. We can not use Bragg pulses or Bloch oscillations, because the entanglement is generated in the spin space and needs to be transferred to the momentum space. For an explanation why it is an advantage to create it in the spin space see Chap. 3. For that reason the pulses which are used to implement the interferometer in momentum space need to be state selective. Therefore, the use of Bragg pulses and Bloch oscillations is not possible, because they act state-independent.

Another option is the use of 2-photon-Raman transfers for the momentum transfer. Raman pulses are state selective and can be used multiple times in a row to transfer multiples of $2\hbar k$ momentum, with a record of $400\hbar k$ momentum [60]. Such a multiple momentum transfer is displayed in Fig. 2.7. To this end, two phase-locked lasers with a frequency difference corresponding to the energy difference of the two hyperfine levels are required. The lasers need to be aligned in the direction of the desired acceleration. Each transfer also changes the internal state of the atoms which is not a problem because the internal state can also be changed back by a microwave pulse. With this the entanglement can be transferred from the internal to the external momentum states.

Now, two different interferometer types will be shown that both are able to measure the Earth's acceleration using different squeezed states.

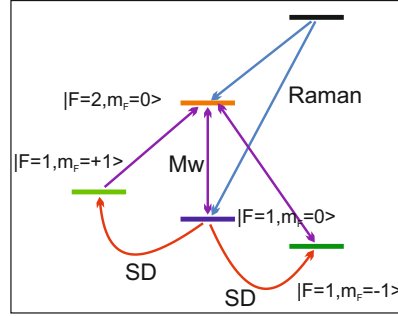
4.3.1 *Twin-Fock interferometer*

Figure 4.4: **Level scheme for the twin-Fock interferometer.**

Microwave transfer (purple) between different levels and $|2, 0\rangle$, the transfer from $|1, -1\rangle$ is only used for preparation purposes. Spin dynamic (SD) starting in $|1, 0\rangle$. The detuned intermediate level for the Raman transfer is in the $5P_{3/2}$ manifold. Notice that the microwave pulses can be π -pulses or $\pi/2$ -pulses. Two photon Raman transfer (blue) between the clock states.

In this interferometer, a twin-Fock state is used as an input state, with the transitions shown in Fig. 4.4. Notice that the average number is always the same for a twin-Fock state but the distribution of the fluctuation is changing. This distribution contains the information. This is important, because now the variance needs to be measured.

The atoms are prepared in $|1, 0\rangle$, that is also shown on the Bloch spheres in the $o/+1$ and $o/-1$ basis in Fig. 4.6. Subsequently a twin-Fock state is generated in the $|1, 0/\pm 1\rangle$ levels, with the methods explained above. Because of the non-100% transfer, the residual atoms in $|1, 0\rangle$ are transferred to $|2, 0\rangle$ via a microwave π -pulse and then removed from the system by a resonant light push. After this process the BEC is released from the external potential and freely falling. Now we have only two atomic levels populated which is the twin-Fock state in the basis of $m_F = \pm 1$ and disregarded the the $m_F = 0$ level as described in the last section. It is displayed in the second Bloch sphere as an infinitesimally small ring on the equator. To access one of the two atomic ensembles with the Raman laser, minimal one ensemble has to be in one of the clock states. Clock states are, in first order, the magnetic insensitive states $|1, 0\rangle$ and $|2, 0\rangle$. Therefore the atoms in $|1, -1\rangle$ are transferred into the $|2, 0\rangle$ level via a microwave π -pulse, which only changes in which level the twin-Fock state is and not the state itself as shown in the third Bloch sphere. Now there is a freely falling cloud in $|1, 1\rangle$ as a reference and a second in the $|2, 0\rangle$ clock level and the preparation could be finished. To avoid to measure the influence of magnetic field noise, the reference state is transferred from $|1, 1\rangle$ to $|1, 0\rangle$ via a radio frequency rapid adiabatic passage. The transfer is possible without coupling to atoms in $F = 2$ using a

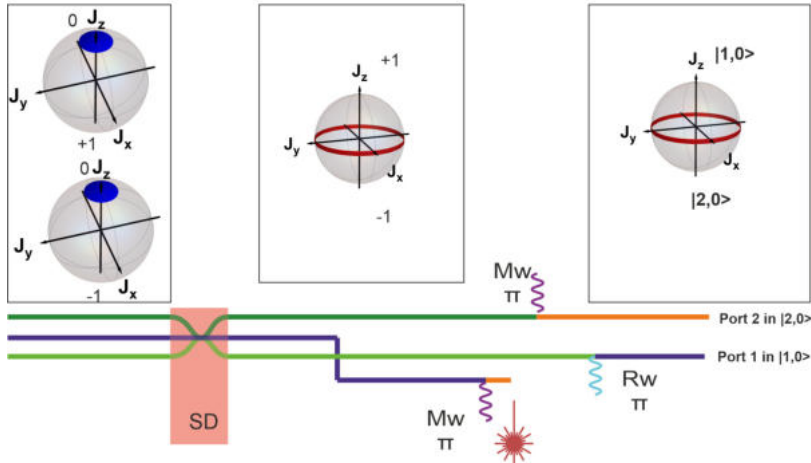


Figure 4.5: **State preparation for the twin-Fock interferometer.**

Spin dynamics produce the twin-Fock state. After a base change, the remaining atoms are transferred from $|1, 0\rangle$ to $|2, 0\rangle$ and been removed by a resonant light push. Afterwards, the atoms in $|1, -1\rangle$ are transferred to $|2, 0\rangle$.

technique explained in Sec. 6.1. Now both states are in clock states, which are insensitive to magnetic field fluctuations to first order. After a sufficient free-fall time to distinguish the Raman transitions - they are shifted by the Doppler effect - the interferometer sequence can begin.

The interferometer is initiated with an opening microwave $\pi/2$ -pulse that couples the two levels of the twin-Fock state and rotates it on the first Bloch sphere as shown in Fig. 4.6. This state is now highly sensitive for phase changes that are described as a rotation along the equator of the Bloch sphere. Up to now, only the internal levels should be coupled with each other. To achieve a spatial separation, the atoms in $|2, 0\rangle$ will be accelerated by a Raman π -pulse that transfers the $2\hbar k$. Because of the internal level change that happens with this transfer, the atoms are transferred back by a microwave π -pulse. This short sequence can now be repeated to transfer multiples of $2\hbar k$ momentum. I present here the sequence with the microwave state change due to the better control and efficiency compared with a co-propagating Raman laser pulse for our experimental setup. A similar idea for large momentum transfer (LMT) is shown in [60, 61] with Raman lasers only. For a setup with a higher efficiency in the Raman transfers also that technique can be used. The pulse sequence is then reverted to return the momentum back to $0\hbar k$ compared to the free falling reference ensemble, displayed by the second laser symbol in Fig. 4.6. After an evolution time T in which a phase depending on gravitational acceleration is collected, the two short sequences of accelerating downwards and the stopping are repeated. The phase shift is depicted on the second Bloch sphere as the rotated red circle compared to the start in

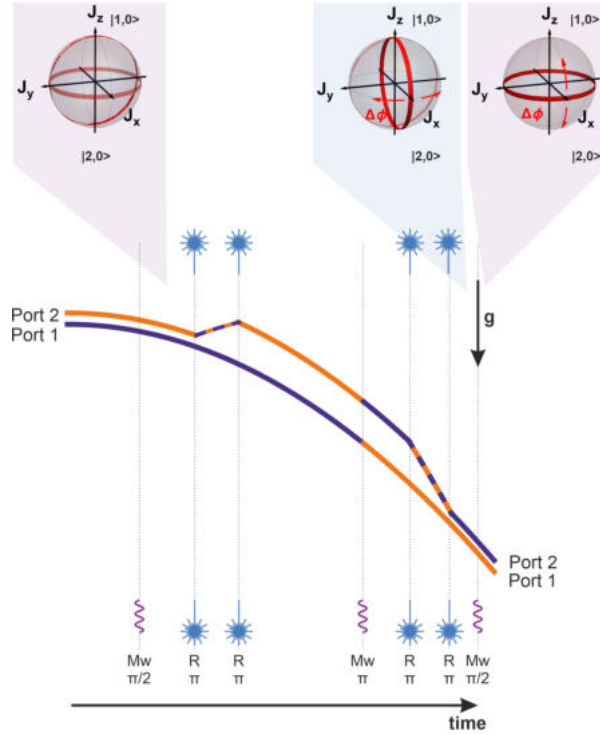


Figure 4.6: **Scheme of the twin-Fock interferometer**

The state is displayed on the Bloch sphere, " $R\pi$ " is a combination of Raman and microwave pulses. The input state generation is explained in Fig. 4.5. The dashed lines display the changes of the internal states during the acceleration and deceleration process. The depicted phases are chosen to depict the single steps.

light red. Now the two ensembles are spatially overlapped, but the internal states are not recombined. This is done by another microwave $\pi/2$ -pulse that couples $|1,0\rangle$ and $|2,0\rangle$ and therefore closes the interferometer. The measured atom number as a projection onto the J_z -axis gives now the measured phase. To measure g , the evolution time is changed and the measurement sequence repeated. If the starting phase is known also only one evolution time is sufficient, for an unknown starting phase there need to be minimal two different evolution times. Also it need to be ensured that its known if the point is in the range of 2π of the starting phase or not.

4.3.2 Squeezed vacuum interferometer

The second interferometer type is using a squeezed vacuum state as an input state. The employed states and transfers are shown in Fig. 4.7. The detuned intermediate level for the Raman transfer is in the $5P_{3/2}$ manifold. For the idea of this scheme, I will assume a free fall time that is long enough to separate the different Raman transitions by the Doppler-shift.

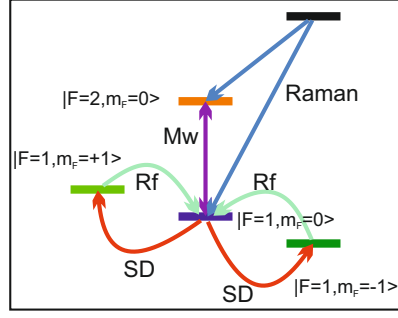


Figure 4.7: **Level scheme for the squeezed vacuum interferometer.** Radio frequency transfer between the $|1, \pm 1\rangle$ and $|1, 0\rangle$. Spin dynamic (SD) starting in $|1, 0\rangle$. Two photon Raman transfer (blue) between the clock states.

As in the twin-Fock interferometer, the atoms are prepared in $|1, 0\rangle$. This is also shown on the Bloch spheres in the $o/+1$ and $o/-1$ basis. Then a squeezed vacuum state is generated in the $|1, \pm 1\rangle$ states. The atoms in $|1, 0\rangle$ are transferred via a microwave π -pulse to the $|2, 0\rangle$ level. Now we have a two-mode squeezed vacuum state in the $o/+1$ and $o/-1$ basis and we will make a base change into the symmetric and anti-symmetric base. These bases are then used to display the squeezed state on the two Bloch spheres in the symmetric/anti-symmetric basis

$$|S\rangle = \frac{1}{\sqrt{2}} (|1, +1\rangle + |1, -1\rangle) \quad (4.20)$$

$$|AS\rangle = \frac{1}{\sqrt{2}} (|1, +1\rangle - |1, -1\rangle). \quad (4.21)$$

In this basis the state is not longer a disk on the Bloch sphere but an ellipse. The orientations of the two ellipses are rotated by 90° with respect to each other and it is single-mode squeezing in the symmetric/antisymmetric base. The symmetric state can then be transferred to the $|1, 0\rangle$ level via a radio frequency pulse, because the radio frequency only couples to the symmetric state. The anti-symmetric state remains unchanged in the $|1, \pm 1\rangle$ levels. These atoms are then not further used and do not interact further with the rest of the atoms during the interferometer sequence. The symmetric state on the other hand is now transferred to $|1, 0\rangle$ making up a simple two-mode interferometer. Now all atoms are in the two clock states $|1, 0\rangle$ and $|2, 0\rangle$ which is the starting point for the interferometer sequence. Therefore the BEC will be released from the external trapping potential into free fall to reach enough Doppler shift to separate the Raman transitions.

The interferometer is equivalent to the twin-Fock case. It begins again with a microwave $\pi/2$ -pulse that couples the $|1, 0\rangle$ and the $|2, 0\rangle$ level. This moves the ellipse on the Bloch sphere from the north pole to the equator, as shown on the first Bloch sphere in Fig. 4.9. The light red ellipse is the starting point from where we start after the preparation phase.

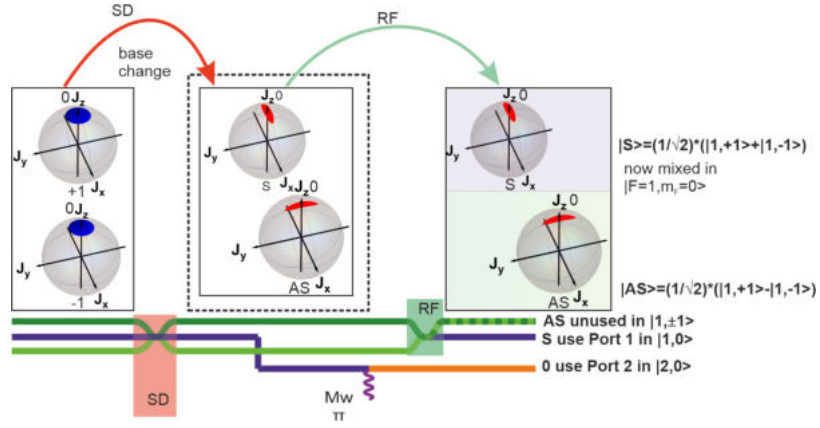


Figure 4.8: State preparation for the squeezed vacuum interferometer.

Spin dynamics produce the squeezed vacuum state. After a base change, the atoms are transferred from $|1, 0\rangle$ to $|2, 0\rangle$. Afterwards, the symmetric state is transferred to $|1, 0\rangle$ via a radio frequency π -pulse.

To now separate and bring the states together again, a series of Raman pulses and microwave pulses are applied as explained before in the twin-Fock interferometer.

The interferometer is closed by a microwave $\pi/2$ -pulse between the $|1, 0\rangle$ and the $|2, 0\rangle$ level. That leads to a rotation of the ellipse on the Bloch sphere which shifts the position of the J_z projection depending on the sampled phase during the evolution time. This projection onto the J_z -axis is measured by a state-selective atom number counting. To now measure g , the evolution time is varied as explained for the twin-Fock interferometer.

This operation of an interferometer with squeezed vacuum allows for an implementation of the optimal squeezing protocol of Sec. 3.2 to cancel the effect of fundamental density noise. The purple arrows showing in opposite directions depending of the sign of J_z display the density effect in the BEC which leads to a twisting of the state during the evolution time of the interferometer. By choosing the right squeezing angle, the twisting of the state during the evolution time in the interferometer can be counteracted. This is shown in the following Bloch spheres by twisting the ellipse on each of it for a little bit. Experimentally the squeezing angle can be choosing by a holding time after the spin squeezing and before the interferometer sequence starts.

With a well adjusted squeezing angle the measurement of the J_z -axis projection always uses the squeezed direction of the state and therefore the measurement can be better than the SQL. The anti-squeezed direction is then pointing in the non measured directions in the J_x, J_y plane. The signal here is imprinted onto the number difference between the two output states, therefore less statistic than for a measurement of the twin-Fock interferometer is necessary, where the variance of the measurement is holding the information.

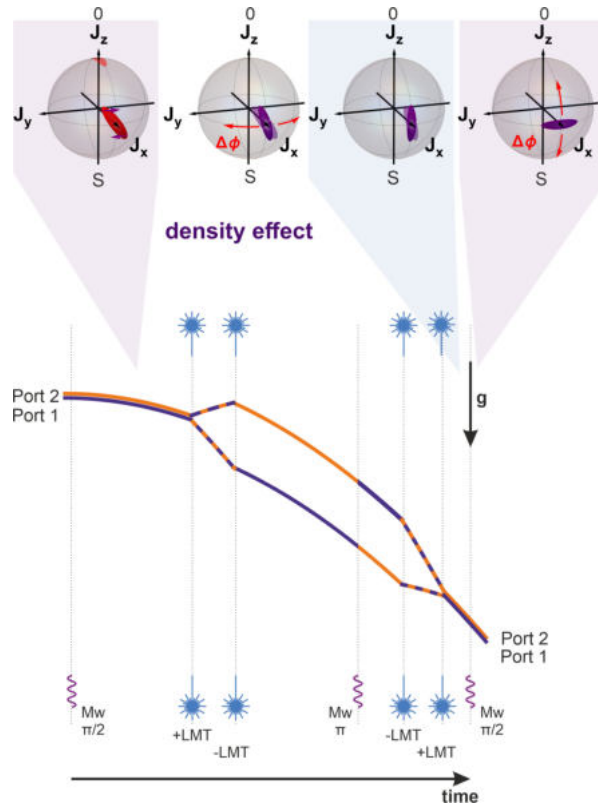


Figure 4.9: Scheme of the squeezed vacuum interferometer

The state is displayed on the Bloch sphere, LMTs are a combination of Raman and microwave pulses. The input state generation is explained in Fig. 4.8. The purple arrows and ellipse show the density shift, the red arrows the phase shift by gravity.

EXPERIMENTAL SETUP

We show how the presented entanglement-enhanced atom interferometer can be implemented experimentally. The results are described in chapter 6.

5.1 GENERAL EXPERIMENTAL SETUP

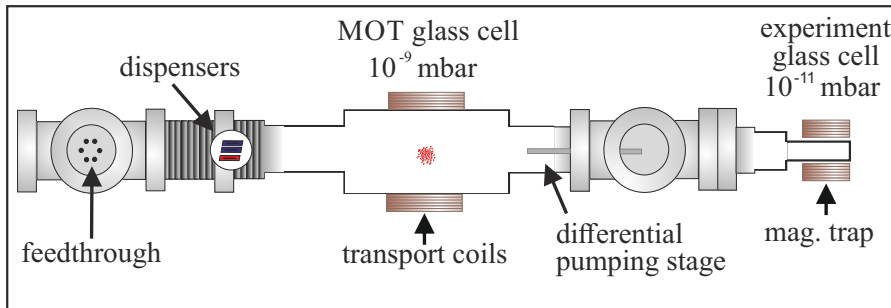


Figure 5.1: **Experimental setup, modified from Ref.**

[62]. A MOT is loaded from the background gas at 10^{-9} mbar. A magnetic trap is created by movable coils that transport the atoms into the magnetic trap in the experimental glass cell at a low pressure of 10^{-11} mbar. After radio-frequency evaporation the atoms are transferred into a crossed beam optical dipole trap.

Our experiments start with a BEC of ^{87}Rb in the Zeeman level $F = 1, m_F = 0$, as proposed in chapter 4. The preparation of these states will be briefly explained, for a more detailed explanation refer to the publications [63, 64] and theses [62, 65–69].

The experiment starts with a magneto-optical trap (MOT) that traps 10^9 ^{87}Rb atoms. The MOT, in a glass cell, is directly loaded from the background gas. We use dispensers as a source for the atoms, that are heated up by applying a current of 3.8 – 4.8 A for the loading time of the MOT (ca. 10s). The current depends on the desired atom flux and the age of the dispensers. To increase the background gas pressure, we shine in UV light to dissolve the Rb atoms that stick to the wall of the glass cell, which is at room temperature where Rb atoms tend to stick. Therefore spectroscopies glass cells are normally heated which is not possible here due to the experimental requirements. It is switched off after the MOT loading phase to reduce the pressure for the rest of the following sequence.

After a phase of 5ms with optical molasses cooling, the atoms are optically pumped into the $|F, m_F \rangle = |2, 2 \rangle$ state. Then the atoms are

trapped by a magnetic quadrupole field generated by two coils in an anti-Helmholz configuration. The coils are mounted on an electrical translation stage, which moves the trap with the atoms within 1.3s from the MOT glass cell into the experimental glass cell. To improve the vacuum pressure on the experimental side the two glass cells are connected by a differential pumping stage, a small tube shown in Fig. 5.1. This allows a pressure difference of 2 orders of magnitude and a ultra-high vacuum pressure of below 2×10^{-11} mbar is reached which is the limit of the hot cathode pressure measurement head (*Varian UHV24P*). This allows for minimal heating and losses of the atomic cloud from collisions with the background gas.

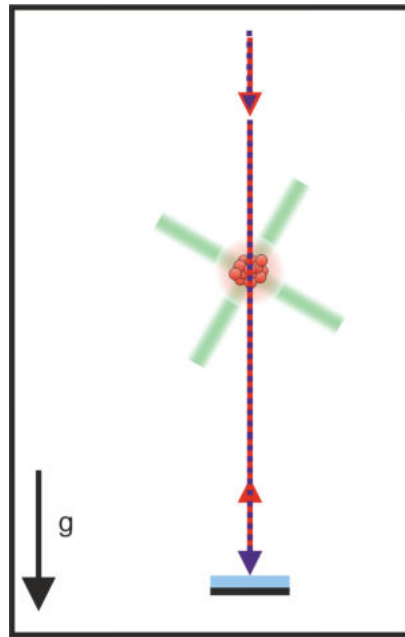


Figure 5.2: **interferometer setup.** The beam with the two different polarizations is vertically adjusted. The BEC is free falling after release from the optical trap (green beams).

The atoms are now transferred into a magnetic trap in quadrupole configuration in the experimental glass cell by lowering the current through the coils of the first trap and ramping up the current through the second trap. The atoms are then cooled near to quantum degeneracy by radio-frequency evaporation. For further evaporation, the atoms are loaded into a crossed optical dipole trap at 1064nm by ramping the optical trap up and the magnetic trap down. The optical trap is slightly below the center of the magnetic trap to reach the best loading efficiency. Both beams are in the horizontal plane with waists of $50\mu\text{m}$ and $30\mu\text{m}$ and maximum powers of 2.8W and 0.8W. The trap is then lowered down to 60mW and 22mW to evaporate the ensemble to a BEC within 1s. To stop the evaporation and reach higher densities, the trap potential is raised again

to the final trap frequencies of $2\pi * (150\text{Hz}, 160\text{Hz}, 220\text{Hz})$. Finally, we can produce BECs up to 30000 atoms with nearly no thermal fraction.

To detect non-classical states, the atom number difference in two or three clouds of atoms has to be measured with sub-shot-noise resolution. In this setup an absorption detection is used. A camera (*princeton instruments pixis 1024 BR eXcelon*) with a high quantum efficiency of $\eta = 0.98$ is used to detect the atoms, which are imaged onto the camera by a telescope setup of an aspheric and an achromatic

lens. The laser beam for the absorption detection passes through a polarization maintaining fiber and is filtered by a PBS and then shone onto the BEC and the camera. For every measurement there are three pictures taken: one with atoms, one only with the absorption beam and one background image. The setup leads to a detection noise of only $22.3(5)$ atoms in the atom number difference at $N = 10000$ total atoms [28]. The noise is explained in detail in subsection 5.3.4.

The state preparation happens in the optical trap after the evaporation. Then the BEC can be released from the crossed-beam dipole trap and then followed by a delta kick, see Fig. 5.2. The delta kick is performed by switching on again the dipole trap for a short time. This reduces the expansion rate of the BEC and leads therefore to smaller BECs after a longer free fall time. Then the interferometer sequence is started. The Raman lasers are orientated in the direction of gravity. The detection area is big enough to be able to detect the atoms also after the free fall time.

5.1.1 *Improvements of the existing system*

In the following subsections I will describe some improvements in this setup that were done since the last description in the thesis of Bernd Lücke [28].

5.1.1.1 *Diode laser exchange*

The cooling laser was changed from a self-built diode laser to a commercial diode laser DL100 from *Toptica* with commercial temperature and current control electronics. The new laser has the advantage of a wide mode-hopping-free range and a better long-term stability. The laser runs at 150mA and 20.1°C with an output power of 80mW in an external cavity setup. As an example in our setup the laser holds the frequency lock on a rubidium spectroscopy for about 1-5 days in average. Now both lasers, the cooling and the repump laser are DL100 laser. The rest of the laser setup is unchanged with respect to the thesis of Carsten Klempt [66].

5.1.1.2 *Detection system*

The original laser system for the absorption detection included a self-built diode laser that was stabilized by a saturated absorption spectroscopy (SAS). This system was installed on an independent optical table with an aluminum shield for laser protection and temperature isolation. With the improvements that I will explain, the long term stability of the detection laser increased and a higher flexibility in the employed frequencies is achieved.

For that reason, the system is installed on the main optical table, together with the rest of the laser system, which gives a better stability

against vibrations. Instead of a saturated absorption spectroscopy, a modulation transfer spectroscopy (MTS) is used to stabilize the laser frequency. The MTS is an advanced version of the SAS. The SAS use frequency modulation in the order of 100kHz. The MTS uses a frequency modulation to generate sidebands with 3MHz on the pump beam. This pump beam is then superposed with the probe beam in the spectroscopy cell, where the modulation is transferred to the probe beam via four-wave mixing. The feature of this spectroscopy is that the four-wave mixing produces sidebands where the lower and upper sideband of the carrier show signals of the absorption depending of their detuning from the transition. This can be used as a control signal. The four-wave mixing only happens in the natural linewidth of the hyperfine transitions, which means the background is nearly zero. Closed transitions produce a stronger signal during the four-wave mixing than open transitions. Therefore, the signal is not disturbed by nearby open transitions.

The frequency generation of the carrier frequencies is realized by a direct digital synthesizer (DDS). The DDS is self-built, and allows to set a frequency at around 160MHz. The DDS also features a register with up to 8 frequencies which can be switched by a TTL signal. In contrast to this register approach, one could also use a voltage-controlled frequency, which changes the frequency by sending a voltage signal to the DDS. This is used to change the frequency of the laser to probe the atomic resonance.

However, this could result in the incoupling of noise. Switching to a different register can be used in the final setup to remove unwanted atoms during the interferometer sequence by shining in resonant light. For more information about the optical setup and the frequency generation I refer to the bachelor thesis of Janina Hamann [70].

With this setup, the requirements are fulfilled: The system allows us to run the detection for a week without the need to relock the laser stabilization. A recalibration of the detection laser frequency is only needed after a couple of months or a change in the detection magnetic field.

5.1.1.3 *Magnetic field stabilization*

The magnetic field stabilization is necessary for the homogeneous magnetic field that lifts the degeneracy of the ^{87}Rb atoms according to the Zeeman effect. This needs to be as stable as possible, because also the q parameter that is introduced in Ch. 4.2 depends on the magnetic field. One of the main noise sources that exists are 50Hz oscillations and higher harmonics of these oscillations that stem from the power line. Their suppression is the main goal of this stabilization.

The old stabilization setup was improved to a higher stability of $57\mu\text{G}$ from shot to shot [71]. The components of the actual stabilization are shown in Fig. 5.3. The magnetic field is measured with a *Bartington*

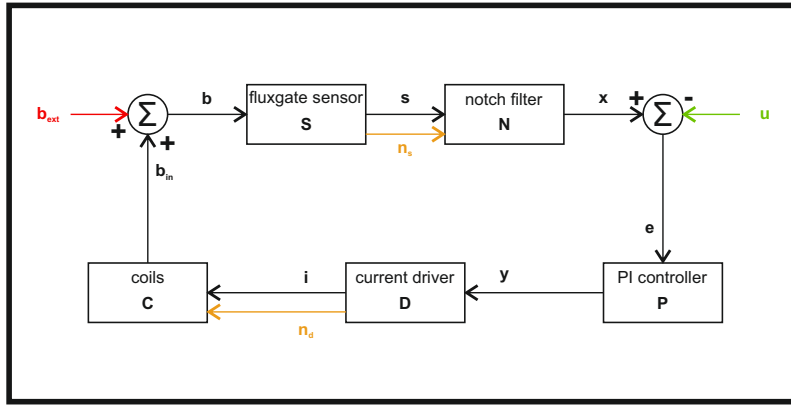


Figure 5.3: **Magnetic field stabilization.**

Schematic of the magnetic field stabilization. b_{ext} is the incoupling external field while b_{in} is the field that is produced by the coils. b is the sum of them. s is the signal of the fluxgate sensor and n_s is the noise of the signal that is produced by the sensor. For the current driver, the notation is similar with i and n_d . u is the set signal for the loop, x is the signal after the notch filter and e is the error signal. y is the signal of the PI controller. Setup from master thesis M.Quensen [71].

Mag-03IEv1 fluxgate sensor, which is able to measure magnetic field strength for small magnetic fields. These sensors have low noise but an internal frequency of 7.813 kHz which limits the maximal speed of the sensor. That could limit the maximal bandwidth of the control loop. The sensor outputs the signal s and the noise n_s . Those signals are then filtered by a low pass notch filter and subsequently present the best estimation of a signal x that can be produced in this setup. This signal is subtracted by the set point signal u that come from the experiment control computer. The error signal e is used in a PI controller to generate a corrected control signal y for the current driver. The current driver sends a current i through the coils in Helmholtz configuration, but also generate some noise n_d on the signal. Finally, the coils translate the current into a magnetic field that is then seen by the sensor and the atomic ensemble.

The notch filter filters out the second harmonic frequency of the sensor, which is fundamentally produced for this type of sensor. As shown in the master thesis of Martin Quensen [71], the coils are the components that are the main limitations followed by the notch filter. The current coils are wound below and above the optical table which has a metallic plate. This can be magnetized and therefore slows down the change of the magnetic field when the current through the coils is altered. Another parameter is that the components of the control loop produce noise, indicated by the yellow arrows in Fig. 5.3. However, the main contributions are the sensor at high frequencies and the notch filter at low frequencies. It could be possible to improve the

performance by removing the notch filter and adjust the parameter of the PI controller.

The improvement that was done is a better PI controller and adjusted filter in the control loop. Furthermore, the sensor head was placed closer to the atoms which improves the stabilization. The placement is now beside the glass cell, fixed to the coils that produce the magnetic quadrupole field. The notch filter was adjusted to reduce the noise floor at the second harmonic of the fundamental of the sensor frequency. The influence of the now improved system to the measurements are explained in Sec. 5.3. For more information about the setup of the regulation and a deeper noise analysis I refer to the master thesis of Martin Quensen [71].

5.1.1.4 Dipole trap

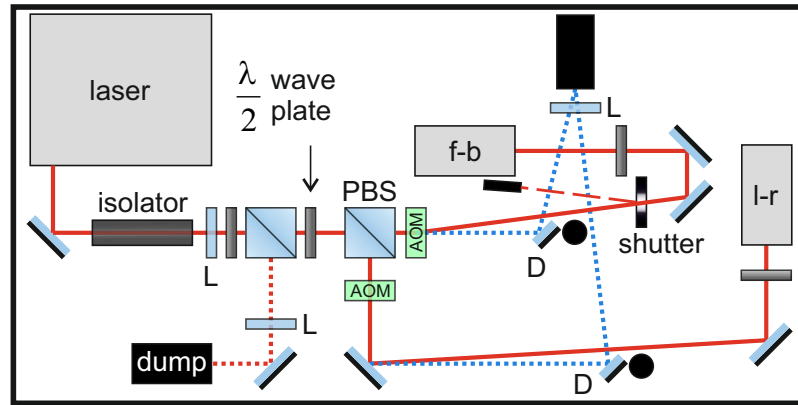


Figure 5.4: Dipole trap laser distribution system.

The beam should be distributed to two fiber couplers for the left-right beam (l-r) and the front-back beam (f-b) of the crossed-beam optical dipole trap. For the switching and power stabilization, AOMs are used and the unused power is dumped in water cooled beam dumps.

To separate the first order beam from the zero-order beam of the AOM, d-shaped mirrors are used (D). The first lens (L) is used to collimate the beam, the two other lenses are used to widen up the beams before entering the beamdumps.

The original laser that was described in [28] is replaced by a 25W *Mephisto* MOPA system from *Coherent* which provides the opportunity to have a stronger crossed-beam optical dipole trap. The solid state laser consists of a seed laser with a Non-Planar Ring Oscillator (NPRO), which is the main reason for a high frequency stability and low noise. In a second step, this light is then amplified multiple times. It is possible to change the laser frequency by up to 30GHz. A water cooling with a minimum flow of $3 \frac{1}{\text{min}}$ is required to be connected for the cooling of the laser. The water in our system has a temperature of 22°C which needs to be well above the dew point of the lab air to avoid

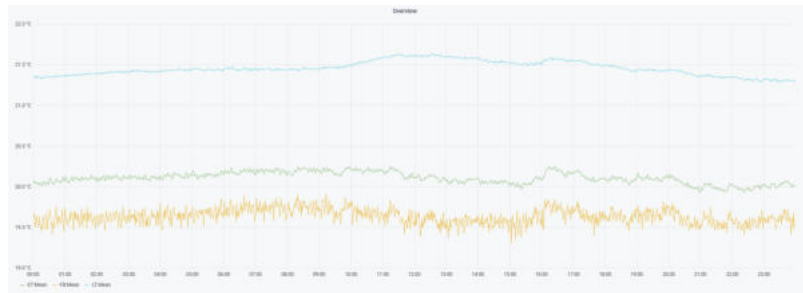
condensation inside the laser. A higher cooling water temperature reduces the maximal heat reduction per hour but this is not a problem in this setup.

Due to the increased power, the distribution system for the 1064 nm light was rebuilt. An external isolator (IO-3-1064-VHP from *Thorlabs*) is placed behind the laser output to protect it from unwanted back-reflections. The position of the isolator is not irrelevant because of the power density threshold of the isolator. To collimate the beam at the preferred size, we have to place a lens with $f = 300\text{mm}$ at 245mm distance behind the laser output. The isolator should be placed 220mm behind the focus and have a length of 115mm, so we made a trade off and placed the isolator as far as possible but before the collimation lens. The collimated beam has a waist radius of $210\mu\text{m}$ at 1m distance behind the focus. After the collimation, a setup made of a $\lambda/2$ waveplate and a polarizing beam splitter is used to attenuate the power, shown in Fig. 5.4. Note that it is not an option to decrease the current in the amplification stage of the laser to decrease the power, because the beam profile becomes worse below the normal current setting. The beam is then expanding using a concave lens and dumped into a water cooled beam dump (LC-ABD-2C) from *laser components* (dotted blue line in the figure). The water cooling is necessary to avoid a heat source on the experimental table. The attenuated beam is subsequently split up and each of the beams is sent through an acousto-optical modulator (AOM) in single pass configuration. The AOMs are used to change the power of the beam depending on a signal from a power stabilization proportional-integral-derivative controller (PID). Finally, each beam is coupled into a polarization-maintaining single-mode fiber to the existing setup. To switch the power off, the PID normally sends zero power to the AOMs. However, in the front-back direction, there is an additional shutter because it is critical to have no photons at all. If the laser would hit the camera during detection, this would degrade the detection. For that reason, the shutter is only closed during our detection sequence. The back reflection from the closed shutter is dumped into a small beam dump that is passively cooled to the optical table. The d-shaped mirrors are used to pick up the zeroth order of the beams and to dump them into a second water cooled beam dump using again a concave lens to expand the beams. The black round posts behind the d-shaped mirrors absorb the rest of the laser light that is transmitted through the mirrors due to the high power of the beams. The $\lambda/2$ waveplates are used to adjust the polarization to the fast fiber axis. The fiber in the left-right direction of the dipole trap has an end cap to reduce the power density at the fiber facet of the in coupling. In the front-back direction a fiber end cap is not necessary, because there is only 1.2W of power used. The entire system is placed in an anodized aluminum box to shield the

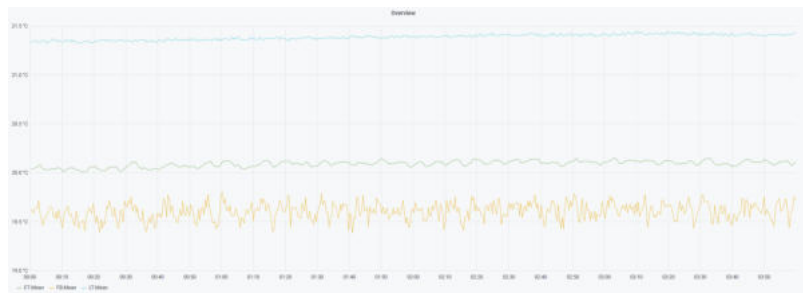
experiment from stray light that could affect the atoms and provides additional laser safety.

For the power stabilization, commercial photo diodes (PDA36A(-EC) from *Thorlabs*) are used with a parallel 50Ω resistance connected to the output, which should have less noise. The photo diodes are then connected to PID controllers which control the power of the AOMs.

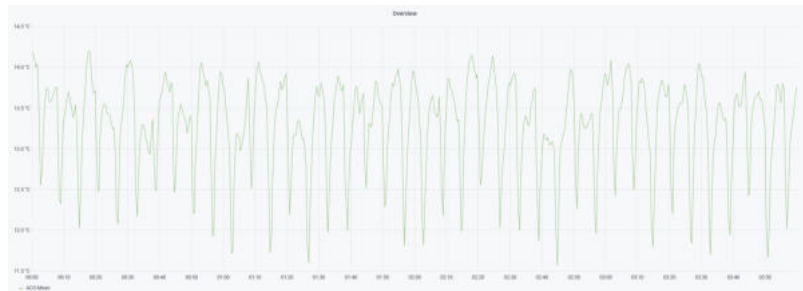
5.1.1.5 Laboratory temperature stability



(a) 24h



(b) 4h



(c) 4h temperature outlet

Figure 5.5: **Temperature fluctuations**

a,b) The yellow line displays the fluctuations in the lab by a measurement near the flowbox in the middle of the lab. The green line displays the temperature on the experimental table and the blue line displays the temperature at the laser table. c) Fluctuations at the temperature outlets of the AC. A clear oscillation is visible.

A new air condition (AC) was installed, to provide a better temperature stability in the lab. The AC has a compressor for cooling and an

electrical heating. For the best result in temperature stability both are running at the same time. The compressor is running between 31Hz and 49Hz. The temperature set point is 20°C and shows peak to peak fluctuations of 0.4°C in the lab. The fluctuations at the outlets of the AC is 2.0°C.

We also measured the temperature on our laser table and the experimental table. The laser table is completely boxed into anodized aluminum which reduces all fast oscillations of the temperature. This leads to a temperature fluctuation of 0.03°C peak to peak fluctuations which is near to the sensitivity of our sensors. The experimental table has a filtered flow box on top which couples the temperature on the table to the temperature in the lab. The sides of the experiment are shielded with removable anodized aluminum shields such that the air flows only from the top to the bottom and leaves the table through the space between the shields and the table. This results in temperature fluctuations of 0.1°C on a similar period as in the lab. Three example curves for one day and for four hours are displayed in Fig. 5.5. On the laser table a slow oscillation over 24h is visible which could depend on the environment around the lab (other rooms/ outside) which cool down in the night. The cooling is here only passive over the table and not active compared to the experimental table with the flowboxes. Therefore the fluctuations on the laser table are slower but the overall drift is bigger than on the experimental table.

5.1.2 State manipulation with microwaves

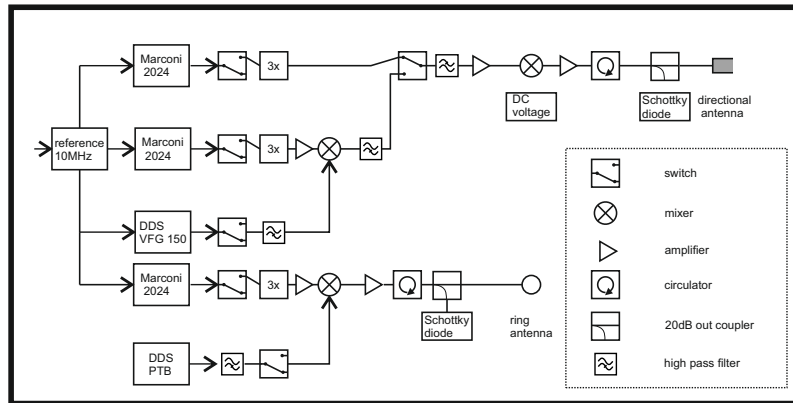


Figure 5.6: Schematic of the microwave setup

From top to bottom there are 3 different microwave chains displayed. They are used for the dressing microwave field as well as for the state preparation. The 3rd microwave chain with the ring antenna is only used when the other antenna is occupied with a microwave dressing.

The circulators are connected to appropriate 50Ω termination to protect the other components from back reflection.

As stated in chapter 2 and 4, we use microwaves to manipulate the internal states of the atoms. We need to use two different microwave frequencies at the same time, one for the dressing frequency and one for the pulses. For that reason, we use two different microwave chains. I will briefly explain how they work and what the characteristics are. For a more detailed explanation look into [28].

All signal generators that are used here are referenced by a ultra stable 100MHz reference oscillator (the same as for the Raman laser system) which is then divided to 10MHz by one of our self-built direct digital synthesizer (DDS). This is necessary because the frequency generators (*Marconi 2024*) do not accept 100MHz reference inputs. On the first antenna we have the option to use the frequency of a signal generator that is tripled to $\sim 6.83\text{GHz}$ and mixed with a dc voltage allowing for intensity stabilization. It is then amplified to 7W and sent to the directional antenna. With this antenna, the efficiency of the power output is increased with respect to a loop antenna. That reduces the pulse duration of microwave pulses at the same output power of the microwave chain. The other option is to use the tripled frequency of 6.705GHz from another signal generator and then mix it with $\sim 135\text{MHz}$ from a DDS. This final signal is then filtered and sent to the same amplifiers and antenna as for the first path. Compared to the first signal, the signal of this second path has a lower spectral purity. This spectral purity is required for long irradiation times of the microwave dressing, where unwanted residual frequencies could cause transfer of atoms into other Zeeman levels. On the other hand, the DDS allows for a fast switching of the frequency and an amplitude shaping of the microwave pulse. That enables the preparation of BEC in the desired hyperfine state in less than $500\mu\text{s}$. The pulse shaping reduces the overall spectral width but increases the width of the central peak which makes the transfer more insensitive to frequency jitter. We use $5\mu\text{s}$ shaped edges on our microwave pulses to benefit from the shaping effect but still achieving fast transfers. The microwave chain also features a power stabilization where a PID controller uses the output signal passed through a Schottky diode as an input signal and regulates a DC signal at the last mixer before the antenna to stabilize the power.

To be able to drive microwave transfers during an active microwave dressing, there is a third microwave that is similar to the second one, just without the possibility of pulse shaping and with a maximum output power of 7W as shown in Fig. 5.6. The Schottky diode in this setup is only used for monitoring because it is not necessary to stabilize the power for short pulses.

Another interesting point is the existence of cross transfer pulses. Due to the finite width of the energy levels and the microwave pulses in the frequency domain, a resonant microwave pulse that should transfer atoms from $|1, -1\rangle$ to $|2, 0\rangle$ also affect the transition from

$|1,0\rangle$ to $|2,-1\rangle$ as shown in Fig. 5.7. This cross transfers would limit the ability to transfer atoms between the states when one of the both other states are populated, which limits the options to design an interferometer sequence. It is most of the time sufficient to compensate one of the cross transfers to have a wide possibility of interferometers sequences because the states can be shifted in a way that they end most of the time on one of the two shown cross transfer positions. It is important to kept that in mind, because the interferometers normally using the clock states, that could be affected. These cross transfers depend on the Zeeman splitting caused by the magnetic field and by the phase caused by the pulse length and the detuning. A way to overcome this problem is to choose the pulse length and the magnetic field in a way, that the unwanted cross transfer has a full Rabi oscillation back into the initial state and the wanted transfer is a π pulse.

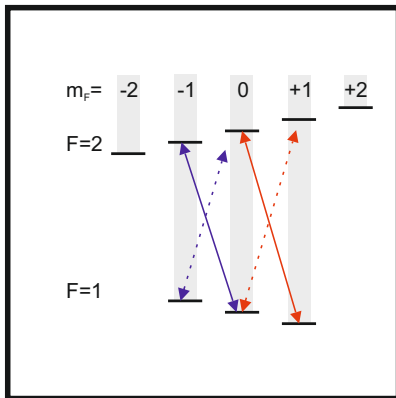


Figure 5.7: **Microwave cross transfer.**

Examples for microwave cross transfers, with the solid line as a resonant 100% transfer, the dashed line is a detuned transfer. The rot and blue pair of transfers have different frequencies.

is a little bit unstable in mathematica, but the changes are minimal. In our experiment we are limited at the moment to magnetic fields up to 3G. On the other hand, it is not possible to reduce the magnetic field too much, due to external frequency noise which would couple into the magnetic field.

I calculated that by using the Clebsch-Gordan coefficients for the coupling between the energy levels. The starting parameters are the pulse durations for the σ_+ , σ_- and π transfers, which are $45\mu\text{s}$, 45s and $34\mu\text{s}$ respectively. As shown in Fig.5.8, it is possible to find various combinations of magnetic fields and pulse lengths to be able to suppress one of the cross transfer pulses. The most interesting values for our current setup are the values around 1.5G with a pulse length around $110\mu\text{s}$. For higher magnetic fields there are multiple more solutions. The slightly noisy looking signal is due to the calculation of the pulse time of the π -pulse, which

5.2 INTERFEROMETER SETUP

As explained in chapter 2, two lasers with a frequency difference on the order of the hyperfine splitting of rubidium are required for a Raman transfer. I will explain here the experimental setup in detail.

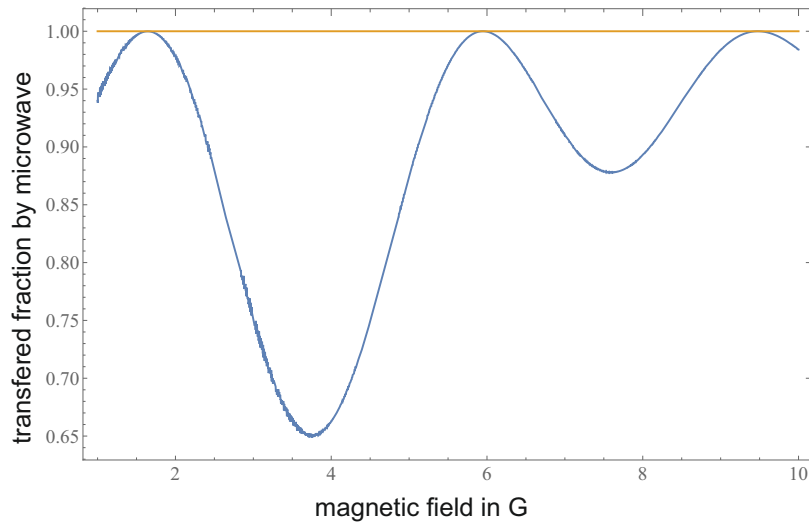


Figure 5.8: **cross transfer pulse simulation.**

Cross transfer calculated for a resonant transfer from $|1, -1\rangle$ to $|2, 0\rangle$. The pulse duration for the π -pulse is calculated in dependency of the magnetic field. The maxima displays the combination where 0% of the atoms are transferred by the cross transfer pulse due to a full Rabi oscillation back to the initial state. The orange line is a guide to the eye for 100% transfer.

The Raman lasers are self-built diode lasers, (a master and a slave laser) that are superposed with each other before they are emitted from the laser housing. The master laser is an interference-filter-stabilized diode laser with external cavity (ECDL), that is sent through an isolator to protect the diode from unwanted back reflections. A small portion of light is transmitted through a mirror and used for a rubidium spectroscopy setup and a frequency stabilization with respect to a Rb reference laser.

For this lock, the light is coupled into a fiber to guide it close to the cooling laser. The two beams are then superposed by a PBS and sent to a photo-diode. The photo-diode is supplied via a bias tee that is connected to a 9V battery. The signal is amplified by two *Mini Circuit* amplifiers (ZJL-7G) and split into two paths. One path is used to directly monitor the beat signal on a spectrum analyzer, the other one is mixed with a 1GHz signal from a frequency synthesizer (the synthesizer that is also the frequency reference). In a last step, the signal is filtered by a low pass at 520MHz and transformed into a voltage by a frequency-to-voltage element. This voltage is used as a direct input for the proportional-integral-derivative controller (PID) of the master laser which generates the error signal for the master laser piezo element. With this setup, the detuning of the Raman laser to the cooling transition of ^{87}Rb is set and can be adjusted.

The main part of the master laser beam is then amplified by a tapered amplifier and sent through another isolator to a PBS to combine

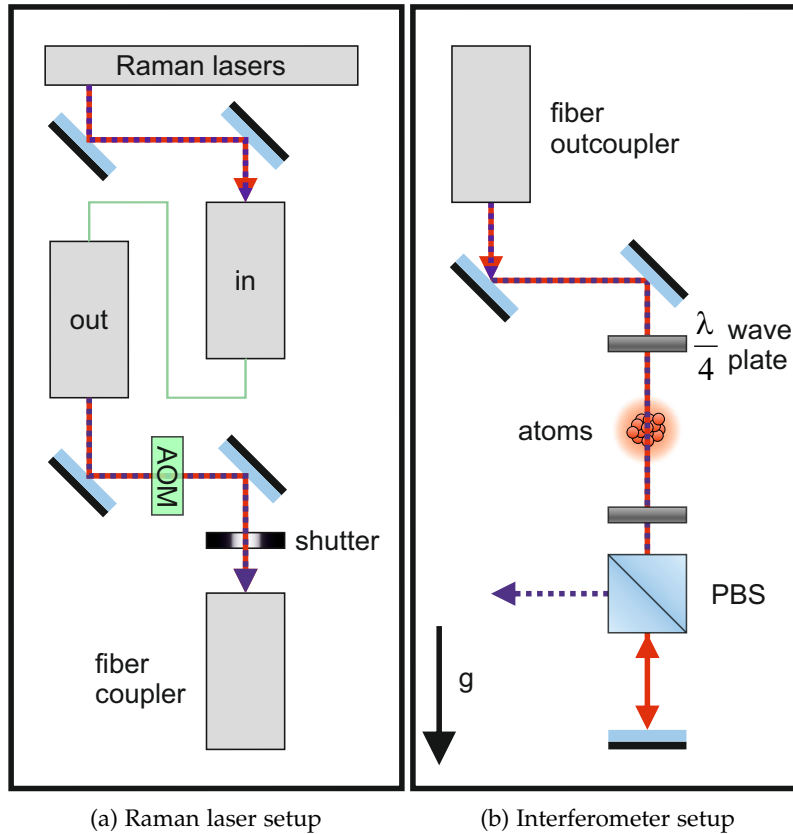


Figure 5.9: **Experimental interferometer setup.**

- a) The Raman laser emits two linear polarized beams with 90° rotated polarization (blue and red beam). The beam is guided through a filter and a switching setup. Finally it is coupled into a fiber from the optical table to the experimental table. b) The beam with the two different polarizations is vertically adjusted to gravity and the light is circular polarized by a $\lambda/4$ waveplate. On a PBS, one beam is coupled out and the other is reflected back.

it with the slave laser. The slave laser setup is similar, without the beam that is used for a offset lock. The main part of the combined beam at the PBS is the output laser beam, but a small portion is coupled out through the second exit port of the PBS and focused onto a GaAs photo diode (*Hamamatsu G-4176*) for the phase lock of the two lasers.

For the phase lock, the photo diode is supplied by a bias tee (*Mini-Circuits ZX85-12G-S*). The signal is amplified with a low noise amplifier (*MITEQ AMF-3B-067069-30*) and converted to 166MHz by mixing the signal with a highly stable microwave reference at 7GHz. A 100MHz quartz oscillator that is phase-stabilized to a 5MHz quartz oscillator is the base of this reference frequency and multiplied to output the 7GHz. The mixed signal is sent to a phase detector where it is compared to the reference signal of 166MHz from a self-built DDS that is stabilized to the same 100MHz reference. The generated error signal is used

for two different control paths. For the fast control path with a high bandwidth, the current through the laser diode is modulated by a direct AC coupling to the output of the laser diode current driver. The slow control path uses the signal as an input into a PID controller that is sending an error signal to the modulation input of the laser diode driver. It is limited to a bandwidth of up to 100kHz. This combination reduces the influence of the low-frequency noise on the fast regulation path. This system stabilizes the Raman laser beat frequency, which can be changed between each Raman pulse with a minimal dead time of less than 100 μ s. Now, all frequencies of the Raman system are defined and ultimately reference stabilized to the reference oscillator.

After leaving the Raman laser the superposed beam is sent into a switching and stabilization setup that is shown in Fig. 5.9a with its main components. The output beam is coupled into a polarization maintaining fiber through two mirrors and a $\lambda/2$ wave plate. This is necessary to transform pointing fluctuations in the beam into power fluctuations, which can be stabilized afterwards and do not affect the rest of the setup. After the first fiber, the beam is sent through an AOM for switching and shaping the laser pulses that are used in the interferometer. After the AOM, another set of mirrors and a $\lambda/2$ wave plate are used to couple the beam into a second fiber that transfers the light onto the experimental table. The shutter is used to ensure that no light reaches the atoms during the time they are in the dipole trap while still being able to work with a warmed-up AOM. The power of the master and the slave are monitored by measuring the transmitted signal on PDs behind two mirrors, using PBSs to only measure the master or the slave laser. These signals can be used in a digital PID that modulates the current through the tapered amplifier to regulate the power in both laser beams.

We chose a setup with back-reflection of the laser beams to have a better phase lock. The Raman lasers are stabilized with the phase lock, every phase that couples into only one of the lasers after that point worsen the phase stability of the Raman lasers. If we use one laser from the bottom and one laser from the top, we would have longer independent laser paths, where the phase could change individually. Therefore, we chose the setup with a back reflected beam, which have the same laser path. The goal of this setup is to have only one pair of counterpropagating Raman laser beams, as shown in Fig. 5.9b. For that reason we have to couple one of the Raman laser beams out to be not back-reflected. To adjust the Raman beams parallel to gravity, we use the mirrors above the glass cell and a small bowl with ethanol at the place of the back-reflection mirror. The surface is used as a mirror that is referenced to g . For the best possible result, it is important to use a liquid with a low surface tension, to be not influenced by the size of the bowl and to block the back reflections from the ground of the bowl. The back reflections are blocked by a black metal piece on

the bottom of the bowl. To get the best adjustment, the beam that is reflected from the liquid's surface is coupled back into the fiber and the power is measured. After this adjustment, the rest of the setup is implemented. The $\lambda/4$ wave plate changes the linear polarized light into σ_+ and σ_- light that can now interact in the two-photon process with the atoms. Behind the glass cell, a $\lambda/4$ wave plate converts the circular polarized light back into linear polarized light. The slave laser beam (blue beam) is then coupled out by a PBS and the red beam in the graphic is transmitted and reflected with a phase jump of π . When it passes the $\lambda/4$ wave plate it is again σ_+ polarized, which gives us the desired pair of σ_+ master laser light and σ_- slave laser light. Depending in which state ($|2,0\rangle$ or $|1,0\rangle$) we want to start the polarization of the coupled beams into the second fiber is changed by 90° , which decides if the master or the slave is outcoupled. The 10m polarization maintaining fiber transmits the Raman laser to the interferometer setup at the experimental glass cell. This makes it even more important to not use a setup with two individual laser path, because the phase accumulated in a individual polarization maintaining fiber is different.

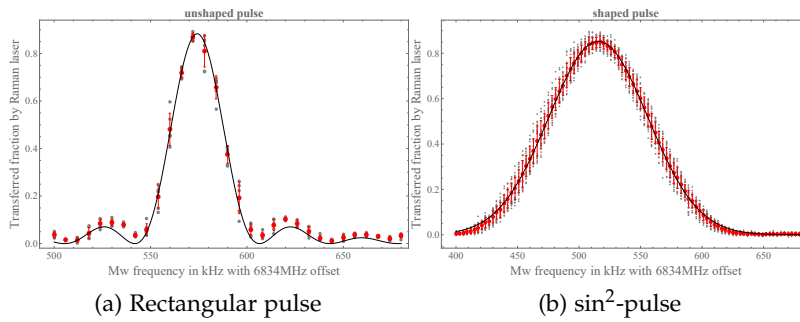


Figure 5.10: Raman laser pulse shaping

- a) Frequency vs transfer, with a pulse duration of $29\mu\text{s}$ for a block pulse. b) \sin^2 -pulse for pulse time of $14\mu\text{s}$

PULSE SHAPING Pulse shaping is also used in the interferometer. The AOM in the Raman laser setup allows for a shaping of the amplitude of the Raman pulses. The shaping of the pulses as a Blackman pulse would yield a good compromise between the width in the time and frequency domain. This would be beneficial to make the transfer less sensitive to frequency fluctuations in the Raman transfers. Because our frequency generator can already generate \sin^2 pulses we will use them. \sin^2 -pulses favor a wide pulse maximum and suppress higher order peak, as seen in Fig. 5.10b. Compared to that, a rectangular pulse is shown in Fig. 5.10a, where the second and third order maxima are clearly visible. The frequency width is then together with its second and third order maxima wider than the shaped pulse, which demands

a stronger separation of the energy levels in the BEC by a Doppler shift. This is an unwanted feature because this effect can excite undesired transitions. The method to normally negate that is a longer free fall time which is not an option for our setup. The only disadvantage of the shaped pulses are that the pulse time is nearly doubled due to the reduced total transferred power.

Both graphs were measured below the optimal pulse time, therefore the transfers do not reach 100%. That reduces only the maximal transfer and does not effect the shape of the pulses.

5.3 NOISE SOURCES IN THE INTERFEROMETER AND THE STATE PREPARATION

The different experimental components contribute to the noise in the state preparation and the interferometer. In the following section the different noise contributions are explained and discussed.

5.3.1 Raman laser

The Raman lasers are among the most crucial parts in the interferometer setup. The Raman transfer efficiency is a limit for the sensitivity of the interferometer. There are two important time scales for the noise of the Raman laser: long term drifts and shot-to-shot fluctuations including fluctuations between the single Raman laser pulses during the sequence. Both are associated with fluctuations in the absolute and relative Raman laser power and the polarization of the two Raman laser beams.

This leads to an influence of the AC Stark shift. The AC Stark shift stems from the influence of an off resonant light field on the level structure of an atom. It shifts the energy level depending on the detuning Δ and the Rabi frequency Ω of the light field.

$$\omega_{AC} = \frac{\Omega^2}{4\Delta} \quad (5.1)$$

For the calculation of the shift, all couplings with a higher multiplet level need to be summed up. For our case of a two photon light field with the frequencies ω_1 , ω_2 and the frequency difference ω_{12} between them, the frequency is

$$\omega_{AC,j} = \sum_k \frac{\Omega_{1,k}^2}{4\delta_{1,k}} + \sum_k \frac{\Omega_{2,k}^2}{4\delta_{2,k}} \quad (5.2)$$

with $\delta_{1,k}$ and $\delta_{2,k}$ as the detunings of a multiplet level $|k\rangle$ and the Rabi frequencies weighted by the corresponding Clebsch-Gordon coefficients. That leads in this case to a relative AC Stark shift of the resonance frequency of $\omega_{AC,diff} = \omega_{AC,e} - \omega_{AC,g}$. If the two levels shift

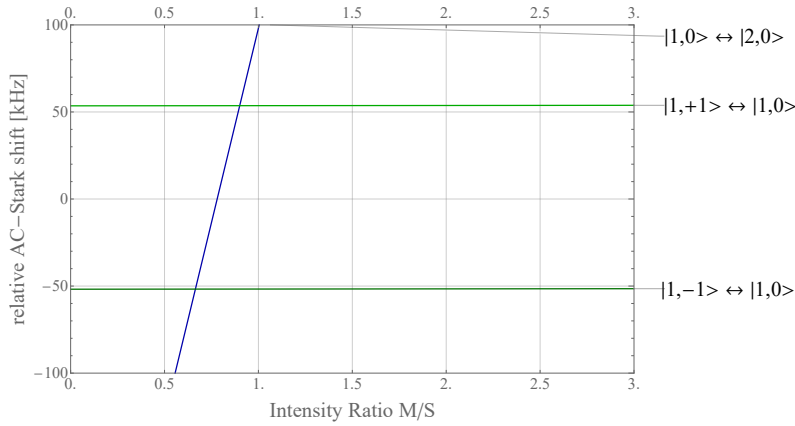


Figure 5.11: **Relative AC Stark shift.**

Relative AC Stark shift over the ratio between master and slave laser for an example parameter set in the experiment. The shifts are shown with respect to $|1,0\rangle$ for the levels $|1,\pm 1\rangle$ (dark and light green) and $|2,0\rangle$ (blue line).

exactly by the same amount, fluctuations of the total power do not change the resonance frequency of the transition.

In Fig. 5.11, the relative AC Stark shift is shown for 3 important transitions. The ratios are calculated at the position of the atom cloud. Therefore, the power ratio of the lasers after the fiber outcoupler needs to be different, because the slave laser is outcoupled and only counts once and the master laser is retro reflected and counts double at the position of the atoms. In addition, also the imperfect behavior of the polarization has to be taken into account, therefore the optimal experimental measured ratio is only close to the calculated values. The clock transition $|1,0\rangle \rightarrow |2,0\rangle$ is displayed in blue in the graph. It is visible that the slope of this transition is magnitudes higher than the ones for the levels in the $F = 1$ manifold. The shifts of these levels are important when a coupling between these levels is planned.

Furthermore, polarization fluctuations before the second fiber (see Fig. 5.9) translates into power fluctuations for the back-reflected beam and the outcoupled beam, due to the PBS before the back-reflection mirror. These fluctuations will lead to an imperfect power ratio at the position of the atoms which decreases the effectiveness due to a mismatched AC-Stark compensation. These short-term fluctuations of the polarization and the power generate shot-to-shot noise fluctuations of the Raman signal. On longer time scales, the power fluctuations are caused by the pointing fluctuation of the laser system before the first fiber, which translate into power fluctuations. That limits the maximal time, where the interferometer performs well and reduces the statistics of the measurements. For that reason, a power stabilization is implemented, which stabilizes the power behind the first fiber between the different experimental runs. It is a digital PID that uses the signal of

two photodiodes to regulate the current through the tapered amplifiers, as described earlier in this chapter. This stabilization does not interfere with the phase lock, because the regulation signal is only uploaded every 10ms. That is slow compared to the phase lock, but reduce the bandwidth of this stabilization. The bottleneck for a faster stabilization is the realization of the digital PID with LabView.

Other parameters that have an influence on the Raman transfer efficiency are the pulse width in time and the frequency width of the pulse. The noise in these parameters is not a limiting factor, they only have to be adjusted to avoid unwanted transfers from the two parallel Raman beams. The noise of the phase lock does not seem to be a limiting factor for the frequency, because the frequency shift that it could cause is way smaller than the shifts that are caused by the power fluctuations when the pulse time is fixed. But the phase noise can change the rotation axis on the Bloch sphere for our interferometer sequence which then couples into our interferometer signal. This is only significant if the frequency of the noise is high, in the order of the phase lock frequencies.

5.3.2 *Microwave*

The microwave amplitude can fluctuate in polarization or power, but it is hard to differentiate these effects. Moreover, the most precise measurements can only be done with atoms which are on the other hand also affected by the magnetic field. Our setup shows in total a fluctuation below 0.2% in the number of transferred atoms for a microwave $\frac{\pi}{2}$ -pulse. The microwave frequency noise is on the order of a few Hertz, which makes it negligible compared to the magnetic field noise. More information on the microwave noise in our setup is found in [28].

5.3.3 *Magnetic field*

The magnetic field fluctuations have a direct influence on our state preparation and the interferometer. When the magnetic field is fluctuating slowly, i.e. between two measurements, we have a different q value for our squeezing and a non-perfect efficiency for our transfer pulses between the Zeeman and hyperfine levels. The most sensitive measurement method that we can use is a Ramsey measurement [72, 73] of the transfer from $|2, 2\rangle$ to $|1, 1\rangle$ with two microwave pulses. This transition has the highest magnetic sensitivity. The Ramsey measurement consist of two $\pi/2$ pulses with an evolution time in between where the pulse duration is short against the evolution time. For that reason, the measurement is more stable against influences like a spatially inhomogeneous field or fluctuations of the microwave power or frequency. Nevertheless, the influence of the microwave instability

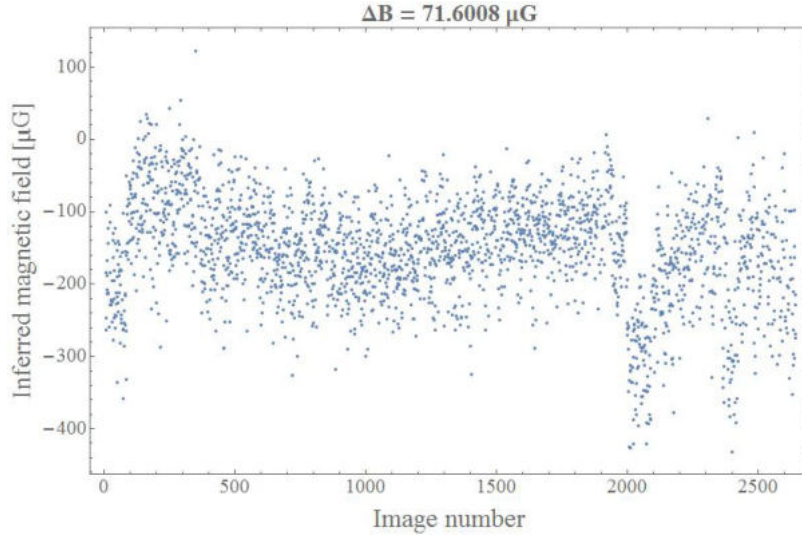


Figure 5.12: **Magnetic field noise.**

The average magnetic field noise is $72\mu\text{G}$ over a time of 19h.

noise can not be fully neglected, so that the measurement in Fig. 5.12 is a measurement of both noise sources. We measured an upper limit of the magnetic field noise of $\Delta B = 72\mu\text{G}$ over 19 hours, which is sufficient to generate entanglement and to operate an interferometer. The measurement includes a slow drift, therefore the shot-to-shot fluctuations are lower. For an overview of the detailed noise in the magnetic field stabilization, please refer to 5.1.1.3, and for more details to the corresponding thesis [71].

5.3.4 Detection noise

We use an absorption detection in our setup, that has the photon shot noise and the quantum efficiency of the camera as main fundamental noise sources plus the technical noise. The assumption is that the power of the laser beam is chosen such that the non-linearity in the atom light scattering is small. The camera converts the photons with a quantum efficiency η into electrons that are subject to shot noise. Therefore, the fundamental noise $\Delta N^{(i)}$ for a pixel i is

$$\Delta N^{(i)} = \sqrt{\frac{A_{px}^{(i)} h \nu}{\eta t}} \sqrt{\left(\sqrt{I_a^{(i)}} \frac{\partial n_c^{(i)}}{\partial I_a^{(i)}} \right)^2 + \left(\sqrt{I_b^{(i)}} \frac{\partial n_c^{(i)}}{\partial I_b^{(i)}} \right)^2} \quad (5.3)$$

with A_{px} as the area of the pixel, t the illumination time, $I_a^{(i)}$ the intensity with atoms, $I_b^{(i)}$ the intensity without atoms and n_c the atom column density [28]. Because the fluctuations in the camera pixels

are independent from each other, this leads to a fluctuations of the estimated atom number of

$$\Delta N_{est} = \sqrt{\sum_i (\Delta N^{(i)})^2}. \quad (5.4)$$

The minimal detection noise calculated for our system with formula 5.4 is $\Delta N_{est} \approx 10$ atoms. It is calculated with our optical parameters and an imaging intensity of $I \approx 40 \frac{W}{m^2}$. The noise is nearly independent from the number of atoms and is between $\Delta N_{est} = 10.6$ and $\Delta N_{est} = 9.3$ atoms for $N = 0$ to $N = 10000$ atoms in one cloud [28].

The technical noise is around 17 atoms which is added up to the fundamental noise. The total noise is measured and then the technical noise is calculated by subtracting the fundamental photo electron shot noise. The main technical noise sources are imperfections of the optics, dust that leads to diffraction of the beam and small laser beam displacements, which thereupon leads to an intensity fluctuations on the camera [28].

5.3.5 BEC life time

The lifetime of the BEC can be a limiting factor for the measurement with entangled ensembles. The lifetime of the BEC can be reduced by different effects. One effect would be collisions from the background gas which would limits the lifetime to 80s [66], that is reached through the pressure difference through the differential pumping state which is shown in chapter 5. A second effect is the heating of the BEC during the holding time in the dipole trap through the laser. A third effect are the three-body losses in the BEC due to a high density. This losses limits the lifetime of the BEC to 5s. That is the main limitation for the BEC.

5.3.6 Laboratory temperature effects

The temperature fluctuations in the lab and close to the experiment could influence multiple components. Example values for the temperature stability in the lab and on the optical table are given in the section before. Main components that could be influenced by the temperature are the frequency locks of the lasers, the electronic controllers of microwave components and laser locks and the mirrors of the dipole trap setup. There were no correlations seen that the temperature influences these parameters and overall the thermal noise is a minor noise source for the measurement. Nevertheless, the adjustments of the experiment start to deteriorate after days of measurements which could still be caused by long-term temperature fluctuations.

GRAVIMETER

6.1 RESULTS

In this section, I will present the experimental results and discuss possible improvements for a realistic interferometer. Spin-dependent collisions can provide squeezed vacuum in the symmetric superposition $|S\rangle$ of the states $|1, \pm 1\rangle$. Here, I present the realization of an atomic gravimeter which includes this state as an input state. I show that a future reduction of the so far dominant technical noise will allow for operation of this gravimeter with a sensitivity beyond the shot noise limit.

6.1.1 Classical-interferometer

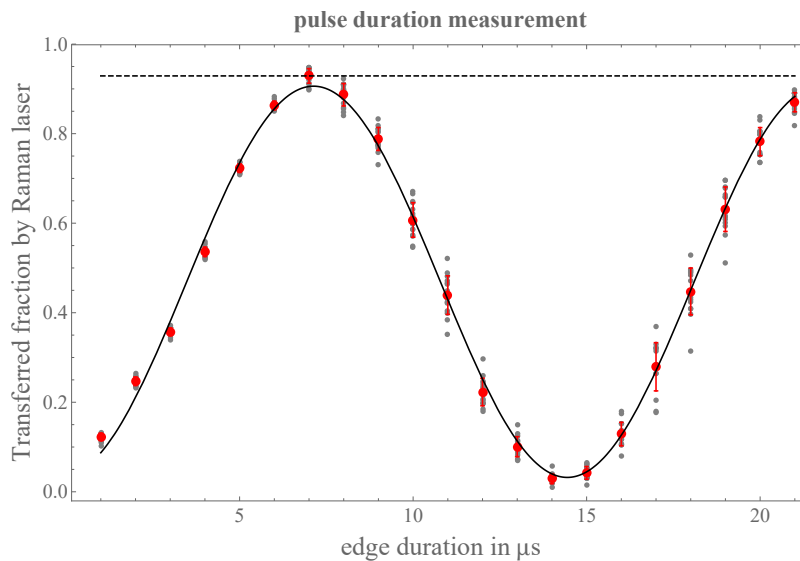


Figure 6.1: **Raman laser pulse duration measurement**

The duration on the x-axis is the time from the begin of the pulse to the maximum. For the full pulse time it need to be multiplied by 2. The black line is a fit through the data points. The black dashed line is only a guide to the eye. The employed pulses have a \sin^2 shape.

The Raman transfer is one of the critical components, because the transfer efficiency fluctuates in time. Therefore, it is analysed before the interferometer sequence. For a spectroscopy of the Raman laser, a transfer efficiency of 93% was measured, see Fig. 6.1. This efficiency depends strongest on the AC-Stark shift compensation and the correct

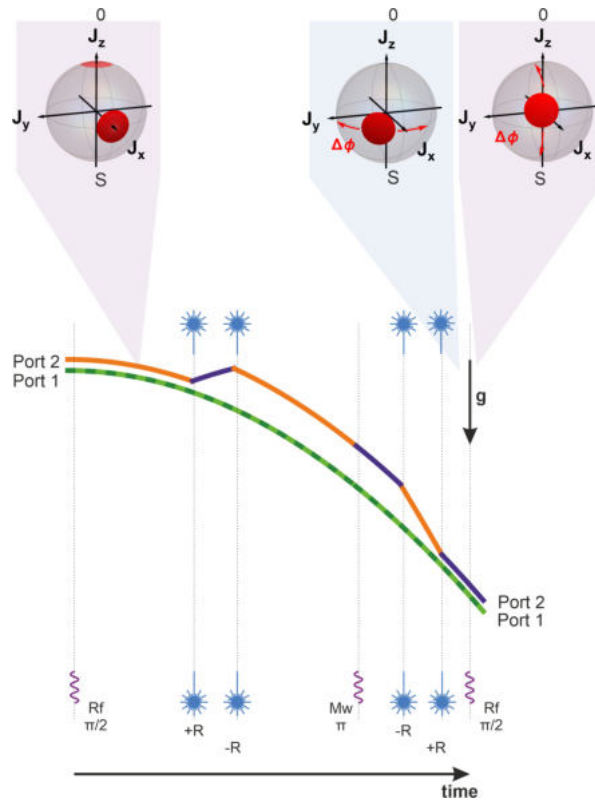


Figure 6.2: **Interferometer sequence**

The Rf $\pi/2$ pulses together with the Raman pulse act as a beamsplitter. The orange color displays the $|2,0\rangle$ level, the blue one the $|1,0\rangle$ and the dashed dark and bright green line displays the $|1,\pm 1\rangle$ level, which contains the symmetric state. The interferometric signal is measured by measuring the atom number in the output ports.

choice of the pulse lengths. The chosen pulse length of $14\mu\text{s}$ for the complete \sin^2 shaped pulse is the trade off that we made between a short pulse that excite other modes and a long pulse that is velocity selective for the distribution in the falling BEC. It is already possible to see in the measurement in Fig. 6.1 that for longer pulse times the fluctuations in the transferred fraction of atoms increases. This can be understood as an influence of the power fluctuations of the Raman lasers. The 2π pulse still transfer a minor amount of atoms due to this fluctuations, also a slowly decay in the maximal transferred fraction can be noticed for longer pulse times. The efficiency can fluctuate and drift during the measurement over all single runs as shown. Therefore this needs to be monitored during the measurement.

The scheme for a squeezed vacuum interferometer is introduced in Sec. 4.3. Before the implementation of squeezed vacuum, the protocol is tested with unsqueezed vacuum in the same state. Therefore, the preparation step as shown in Fig. 4.8 vanishes and we start with all atoms in the $|1,0\rangle$ level. If we use the symmetric and anti-symmetric

basis states of Sec. 4.3, the interferometer is described as a 2-mode interferometer with the symmetric state and the $m_F = 0$ state as a basis.

The employed protocol is shown in Fig. 6.2. At the beginning, all atoms are in the $|1, 0\rangle$ level (displayed on the first Bloch sphere by the transparent red disk) Subsequently, one is transferred to the symmetric state via a radiofrequency transfer to the $|1, \pm 1\rangle$ level, as displayed by the red disk on the Bloch sphere. Because this is a classical state, the uncertainties along J_x and J_y are the same, as represented by a disk. For the squeezing-enhanced operation, spin dynamics can be employed to generate a squeezed vacuum state in $|S\rangle$ prior to this protocol. This would lead to an ellipse that is squeezed along J_z at this point. Now, the ensemble is in a superposition of the symmetric state and the zero state, displayed on the equator of the Bloch sphere. A momentum of $2\hbar k$ is transferred by the Raman pulse in the upward direction. After a waiting time of $70\mu\text{s}$ to separate the two clouds, the second Raman pulse decelerates the cloud in Port 1. The following waiting time is varied to sample different phases, started with a waiting time of $1\mu\text{s}$ up to 1.001ms in steps of $50\mu\text{s}$. The following π -pulse is necessary to change the internal state for downward acceleration with the same pair of Raman beams, (see Sec. 5.2). Then, the two Raman pulses accelerate and decelerate the cloud again and both clouds are overlapped again. After these pulses, another short waiting time is applied that fills up the time of the phase collection to a constant duration of 1.002ms . For the first measurement point the duration is $1\mu\text{s} + 1.001\text{ms}$ and for the last point, it is $1.001\text{ms} + 1\mu\text{s}$. It is necessary to have always the same time between the two radio-frequency pulses that open also an interferometer on the internal states. The quadratic Zeeman effect shifts the energy levels of $|1, \pm 1\rangle$ compared to $|1, 0\rangle$ by $70\frac{\text{Hz}}{\text{G}^2}$, which cause a phase shift between the symmetric and the zero state. If this duration does not change, this part only generates a phase offset which can easily be subtracted to calculate the g -factor. But if the time between the radio-frequency pulses is varied, an additional phase variation is generated which disturbs the phase signal generated by gravity. In theory, that can be calculated and subtracted but it is more precise to avoid a second time dependent signal in the first place. The phase $\Delta\phi$ sampled by gravity results in a rotation around the equator as shown on the second Bloch sphere. The presented shift is only an example and depends on the evolution time. Now, the final microwave $\pi/2$ -pulse couples the symmetric state with the zero mode and closes the interferometer. This is displayed by a rotation around the J_y -axis on the third Bloch sphere. The projection onto the J_z -axis is then measured. This measurement is the atom number in the different states counted by the state selective absorption detection.

The time difference between the third and the fourth Raman pulse is the same as for the first and the second. Between all radio-frequency,

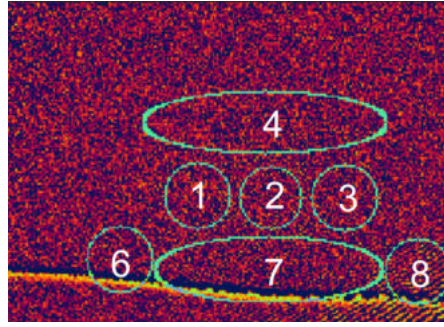


Figure 6.3: Mask placement on the absorption detection picture

microwave or Raman pulses a minimum waiting time of $1\mu\text{s}$ is induced to be ensure that the pulses are well separated by each other. The waiting times between the two Raman pulses are large enough to separate both pulses in the frequency domain.

Now, I will present the detection analysis after a full interferometer sequence. A non-perfect transfer can be observed by detecting atoms on the absorption picture, where they should not appear. I will explain this on an example picture of a rare incomplete Raman transfer, shown in Fig. 6.3. The green lines are the margins of the detection masks, in which the atoms are counted. The picture is taken with a logarithmic color scale, with white for a high atom number and red for a low atom number. In the left-right direction, the states are separated by their magnetic field number and in up-down direction by the momentum, that result from the Raman transfer. The first mask from the top (mask number 4) correspond to $+2\hbar k$ momentum, it collects the magnetic states $m_F = 0, \pm 1$. This mask only contains atoms when a transfer is imperfect and the atoms do not interact with a $+2\hbar k$ and a $-2\hbar k$ momentum kick. For the same reason also the lowest mask (mask number 7) with $-2\hbar k$ is only populated when the transfer is imperfect. The lower masks are more often populated, the corresponding atoms there are transferred by the third Raman pulse, that act one the leftover atoms in the starting state. The atoms that are transferred by the first or the second Raman pulse can be decelerated accidentally by the third or fourth Raman pulse. They are then not distinguishable from atoms in the $0\hbar k$ states due to the not visible spacial difference on the camera. Masks 6 and 8 identify atoms in $|2, +2\rangle$ and $|2, -2\rangle$, respectively. If they are populated, this is a sign for a real rare malfunction of the experiment. The reason can be a changed magnetic field or a delay in the experimental timing. This is a really rare event that can occur and mixed up the timings of the different components in the experiment. The masks 1, 2 and 3 are the masks for the desired interferometer states, they show the atoms with $0\hbar k$ momentum in $|1, -1\rangle$, $|1, 0\rangle$ and $|1, +1\rangle$. At the same position also the atoms in $|2, 0, \pm 1\rangle$ are shown, only with reverted sign, so for example in mask 1 the atoms in $|2, +1\rangle$. That needs to be kept in mind for further investigations of loss

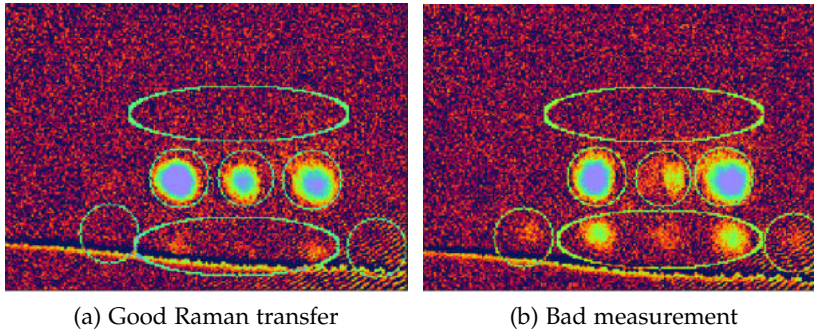


Figure 6.4: **Absorption pictures interferometer.**

- a) Normally looking absorption picture for a good Raman transfer efficiency. b) Post selected picture with bad Raman transfer efficiency and extra undesired transfers.

channels and noise analysis. Due to the interferometer sequence, it is very unlikely to have atoms at all in the $F = 2$ manifold. Therefore, the masks are analyzed as there are no atoms in the $F = 2$ manifold.

As you can see in Fig. 6.4a, a normal sequence produces atoms in masks 1, 2, 3 and only a negligible number in mask 7. On the other hand, during a sequence where a non perfect Raman transfer occurs, there is a bigger percentage of atoms in mask 7 which shows a worse Raman transfer and another problem that produces atoms in $|2, \pm 2\rangle$ (Fig. 6.4b). The process is clearly a influence of a bad Raman laser and are not dependent on the measurement scheme, therefore a post selection is a valid choice. The ratio of atoms outside of the masks 1,2,3 is used to choose only transfers with a high-efficient Raman transfer and no other disturbance that can be seen on the absorption images.

Fig. 6.5 displays an evaluation of the gravimeter sensitivity. As explained before, the measurement is postselected on experimental time jumps and minimal 97% of all atoms in the desired masks for an efficient Raman transfer. The red dots are the result for the different evolution times with one standard deviation error bars. The orange line show a sinusoidal fit with contrast, amplitude offset and phase offset as fitting parameters. The phase offset of 0.88π results from the fixed phase that is sampled due to the energy offset between $|S\rangle$ and $|1, 0\rangle$. The amplitude offset is 0.65. Resulting from the inefficient Raman transfer, which reduces the number of atoms in $|1, 0\rangle$ compared to the atoms in $|S\rangle$. The fitted contrast is $C = 0.4$, which reduces the sensitivity. The reduced contrast is a main technical problem, because a close-to-ideal contrast is required to exploit the effect of entanglement in the interferometer.

For a further analysis, we have to look at the bare data of the fraction of atoms in $|1, \pm 1\rangle$. In Fig. 6.6, the fraction of atoms in $|1, +1\rangle$ is displayed in blue, $|1, -1\rangle$ in green. The contrast ($C = 0.25$) is the

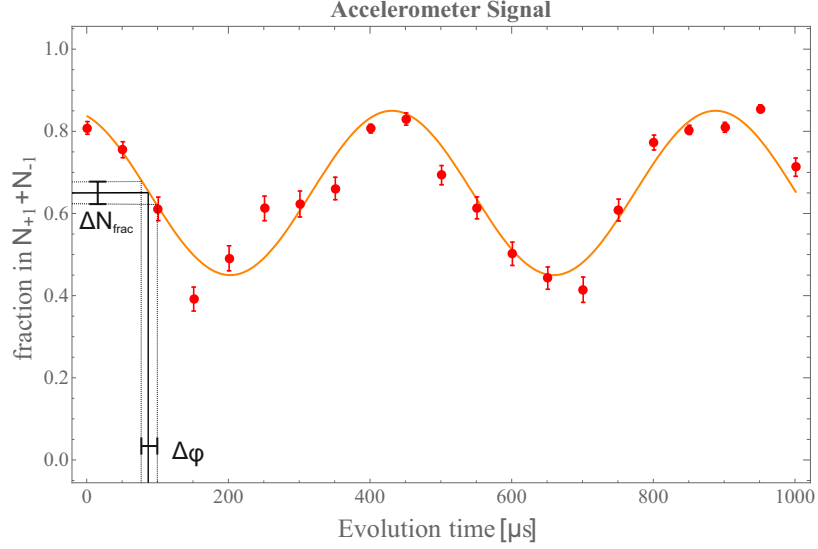


Figure 6.5: **measurement of the gravitational acceleration**

The y-axis is the ratio between the sum of atoms in $|1, +1\rangle$ and $|1, -1\rangle$ and the total number of atoms. The orange line is a sinusoidal fit for an ideal g value, yielding a contrast of 0.4 and a amplitude offset of 0.65 and a phase offset of 0.88π . The black line shows a example value, where the fluctuation in the transferred fraction ΔN_{frac} is used to calculate the fluctuation in phase $\Delta\phi$. That can be then used to calculate the fluctuations in g .

same for both. The amplitude offset for both is similar, the differences can be explained by a slightly suboptimal dressing. As explained before, a reason for the common amplitude offset could be the Raman momentum transfer, here we can see, that the maximal transfer is around 0.42 for the $|1, -1\rangle$ and 0.47 for the $|1, +1\rangle$, which is near to the expected maximum of 50%. That fits with the assumption, because a full transfer would also be possible with a steady amount of atoms transferred to the $|1, \pm 1\rangle$ states, but a fraction of 0% would be impossible. The data shows a phase difference of 0.43π between the two states. The phase difference between the two states explains the reduction of the contrast in Fig. 6.5. If the phase difference was close to π , no signal could be extracted because the sum would be constant. We could prove this interpretation by shifting the dressing frequency by a small amount of 5.1kHz. This leads to a close to zero contrast. The error margin of the calibration measurement for the microwave dressing is bigger than the precision that would be needed for a zero phase shift in the interferometer. This complicates the calibration procedure. Further sources for the phase difference are discussed in Sec. 6.2.

To simulate how much the contrast of the signal would be improved without the phase offset between the states, the phase offset is artificially corrected by shifting the data points. The result is displayed

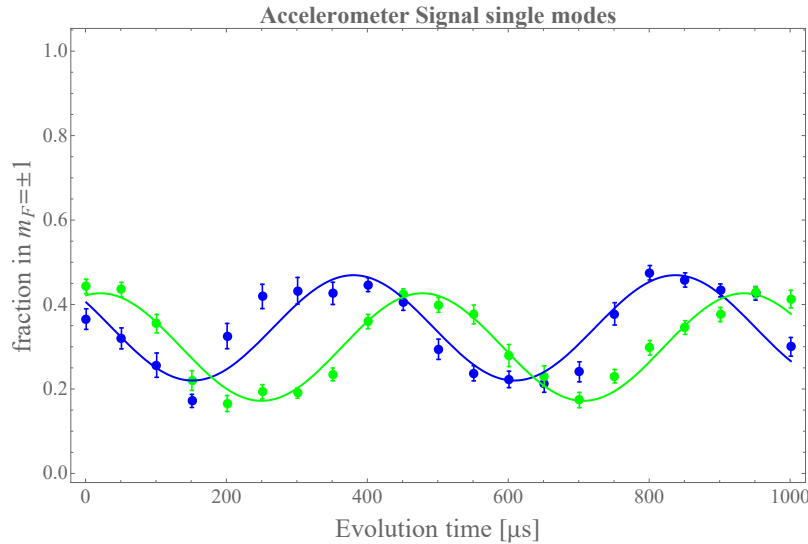


Figure 6.6: **single state g measurement**

The blue line is the fit for $|1, +1\rangle$ and the green line is the fit for $|1, -1\rangle$ compared to the total number of atoms.

in Fig. 6.7, where the data points are shifted and summed up. Compared to the original measurement, the contrast of 0.55 improved by 40%. This means a perfectly set dressing frequency for the microwave dressing is fundamental for a good measurement result. This is still not a contrast near 1, which is necessary to detect entanglement in an interferometer. But the artificial phase shift also destroys the correlation between the $|1, +1\rangle$ and $|1, -1\rangle$ mode, because the data is from different experimental realizations. Therefore, a real measurement could have a higher sensitivity due to the correlations, which could reduce the fluctuations in the sum.

However, we want to calculate the sensitivity of the measurement without the artificial phase shift. Therefore, the fluctuations in the transferred fraction of $|S\rangle$ and $|1, 0\rangle$ can be calculated into fluctuations of the evolution time as shown in Fig. 6.5. This value leads then to phase fluctuations which can be used to calculate the standard deviation of the phase which can be compared to the shot noise limit. I will now evaluate the gravimeter's sensitivity at mid-fringe position, where the sensitivity should be optimal.

Fig. 6.8 shows a histogram of the $551\mu\text{s}$ measurement point as a exemplary point.

Now, we can use the distribution near the mid fringe position to calculate the standard deviation of this distribution. The mid-fringe measurement shows no measured points below 0.2 or above 0.9 transferred fraction. Therefore, I will assume that no fringe hopping was happening and all points are only measured on one slope. The calculated standard deviation is a factor of 84 ± 7 larger than shot-noise. The most relevant source for the increased noise is the phase shift

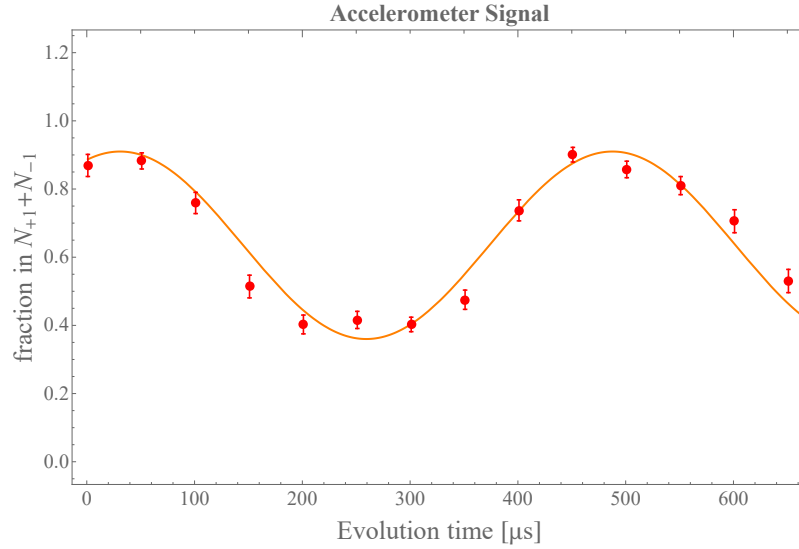


Figure 6.7: g measurement with post correction

The y-axis is the ratio of the sum of $|1, +1\rangle$ and $|1, -1\rangle$ to the total number of atoms. The orange line is the sinusoidal fit for an ideal g value, yielding a contrast of 0.55 and an amplitude offset of 0.65. The phase offset is adjusted. The single measurement points are shown as gray dots. Take into account that the phase offset between $|1, +1\rangle$ and $|1, -1\rangle$ is shifted and the ratios are summed up, which can lead to results larger than 1. The shown evolution time is shorter due to the shift of the data points.

shown before, that leads to a reduced contrast. We believe that fluctuations in the Raman laser intensities lead to strong fluctuations of this phase shift, as I will discuss in the following section. A further contribution is magnetic field noise, that couples to the symmetric state, but the calculated contribution is well below shot-noise.

6.2 DISCUSSION

Because this phase difference between $|1, +1\rangle$ and $|1, -1\rangle$ levels was a major problem, I will describe two experimental causes which lead to such a phase shift. Firstly the phase shift stems from incorrect dressing, which would affect the radio frequency transfers and lead to a constant phase accumulation during the interferometer sequence. This effect was experimentally reproduced by a second measurement with only a small change of 5.1KHz in the dressing frequency which results in a relative phase shift near π between the $|1, +1\rangle$ and $|1, -1\rangle$ levels. Such small changes are beyond the resolution of our calibration procedure. Therefore another technique needs to be developed to adjust the microwave dressing. Normally the dressing is tuned with a BEC in the crossed optical dipole trap and the spin dynamic resonance is observed. This dynamics have a huge variance due to there source

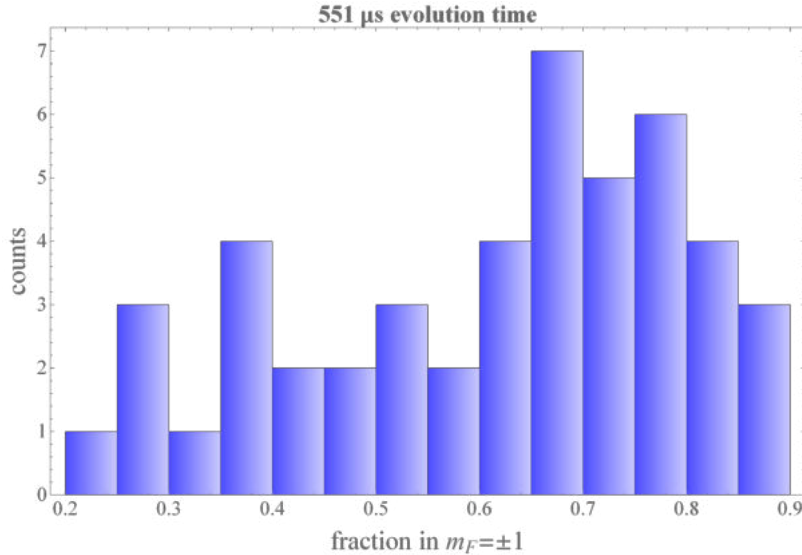


Figure 6.8: **Histogram of the transferred fraction**

Histogram at 551 μ s evolution time of the transferred fraction. The measurement is done near mid fringe.

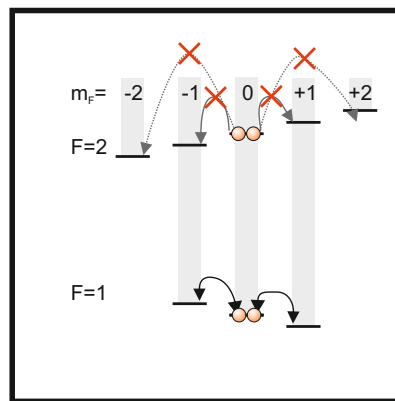
in the vacuum fluctuations, the measurement has therefore an error in the same order of magnitude as the change. An obvious approach would be a calibration with the full interferometer sequence without the Raman pulses.

Secondly, the Raman lasers produce an AC Stark shift of the $|1, \pm 1\rangle$ levels. The 2-photon transfer is very narrow in the range of a few kHz, while the normal light field is broad to couple all internal states to the intermediate level. For that reason, the offset-lock is 1.1GHz detuned to the intermediate level, but the difference between $|1, 0\rangle$ and $|1, \pm 1\rangle$ is only in the order of hundreds of kHz at the given magnetic field of 0.8G. Therefore, also the side levels are affected by the AC Stark shift. The different shifts of the different levels are shown in the Raman noise Sec. 5.3. That could be avoided by using the transfer of the squeezed vacuum to the clock states.

Another point that could be caused by the coupling of the detuned light field, is an increase of the fluctuations during the measurement. Because the AC Stark shift for the $|1, \pm 1\rangle$ levels cannot be compensated, every fluctuation in the power of the coupling laser is translated into a phase shift with a different strength. Even worse is that the coupling strength is not the same for the $|1, +1\rangle$ level and $|1, -1\rangle$ level. Therefore, they experience a differential phase shift, which cannot be suppressed by common mode rejection as in the difference variance analysis, used in Sec. 6.1.

6.2.1 *Improvements*

To improve the interferometer, there are two points to take into consideration. One is the technical implementation. The intensity fluctuations on the Raman lasers are a major problem for the interferometer. Therefore, the stabilization of the Raman laser system need to be improved. That could be done by completely rebuilding the Raman laser system, but with diode laser and without tapered amplifiers. This could increase the power stability, the pointing stability and also the speed of the laser power reacting on the stabilization. Both polarizations would be transferred through individual fibers, thereby improving the polarization stability. The phase lock should then be set-up with a as short as possible control loop, with the photo diodes behind the individual fibers. The only disadvantage of this setup would be that the light path between laser and phase lock detector is longer and also the signal from the lock back to the laser takes longer. This could lead to an increased length of the control loop by 2 – 3m but that should be a really small disadvantage compared to the gain in stability. That would also allow to integrate a power stabilization with AOMs behind the phase lock. These changes together should lead to a more stable Raman laser system with a higher average transfer. Another possible improvement is an even better magnetic field stabilization which allows to hold the corresponding microwave dressing values for a longer time and also reduce the unwanted phase shifts that can come from this as shown above. These are the most promising technical improvements that can be done.

Figure 6.9: **measurement of the gravitational acceleration**Figure 6.10: **Selective radio frequency transfer.**

Radio frequency transfer between the $|1, \pm 1\rangle$ and $|1, 0\rangle$, without transfer atoms in the $F = 2$ manifold.

The second point is a change in the interferometric scheme to the scheme that was shown in Fig. 4.9. This would transfer the single mode squeezed state from the symmetric state $|S\rangle$ to the $|1, 0\rangle$ level.

This has the benefit that the problem of the phase offset between $|1, \pm 1\rangle$ no longer exist, because the atoms do not sample the phase there during the evolution time. Another benefit is that then all atoms are in clock states which makes them less sensitive for magnetic field fluctuations and shifts through off resonant Raman laser coupling. For this, a special technique of radio-frequency coupling [74] by using circular polarization is necessary to transfer the atoms in the $F=1$ manifold and without transferring the atoms in the $F=2$ manifold (see Fig. 6.10).

6.3 SQUEEZED VACUUM VS. TWIN-FOCK INTERFEROMETER

The first big difference between the two different interferometer types is the state preparation. The generation of a squeezed vacuum state is faster, which reduces the heating during the holding time in the trap. This is beneficial to have less noise on the signal. The quasi-adiabatic ramping to generate the twin-Fock state leads to heating due to the long holding time. If the ramping is performed faster, the resulting variance of the transferred atoms becomes larger. This is a disadvantage, because the state should have a similar number of atoms for each cycle. For the longer holding time, the variance of the transferred atoms is smaller, which reduces possible fluctuations that are caused by fluctuations of the total number of atoms, such as density shifts. The squeezed vacuum state can be generated with less noise, mainly due to the smaller duration of spin dynamics. When the heating in the dipole trap could be reduced, the twin-Fock state could also be generated with less noise for smaller atom numbers. This would need a technical improvement of the dipole trap. But also there are still losses from the 3-body losses in the dipole trap which are density dependent, which would be not reduced by this technical improvement.

Another difference is the amount of energy levels that needs to be handled throughout the interferometer sequence. For the twin-Fock interferometer, there are just a few leftover atoms left in the $|1, 0\rangle$ level, which can be easily removed. Only two energy levels corresponding to the two states are handled during the interferometer sequence. For the squeezed vacuum interferometer, there are still atoms in $|1, \pm 1\rangle$ during the interferometer sequence which may not interact during the rest of the sequence with the other states.

In a squeezed vacuum state, the strength of the entanglement can be adjusted, whereas in the twin-Fock state it is set by the generation process and its noise. This is an advantage if a defined amount of squeezing should be reached. Moreover, the density effect compensation that is shown in the scheme for the squeezed vacuum interferometer is only working close to the equator of the Bloch sphere, which is not possible for the twin-Fock state because it covers also the poles

in the phase sensitive time (Bloch sphere 2, Fig. 4.6). Therefore, the squeezed vacuum interferometer has an advantage if the technical noise is reduced sufficient to approach the density limit.

After the state preparation phase, the interferometer schemes are pretty similar, but one big difference that needs to be noticed is that the signal in the squeezed vacuum interferometer is obtained from the atom number difference between the two ports. In the twin-Fock interferometer, the signal is obtained from the squared difference, which requires an adjusted interferometer readout.

CONCLUSION AND OUTLOOK

7.1 CONCLUSION

In this thesis, I presented two different schemes of entanglement-enhanced atom interferometers for a measurement of gravitational acceleration. The schemes and the results of a first, classical version were discussed and evaluated. I have identified uncontrolled AC Stark shifts as a main source of the fluctuations. This leads to the result that the technical noise needs to be reduced before an entanglement-enhanced atom interferometer can surpass its classical counterpart.

In a theoretical analysis, the boundaries for a perfect entanglement-enhanced interferometer in the parameters of squeezing and atom number density were discussed and it was shown that there is an ideal number of atoms where the density effect can be reverted by choosing the appropriate squeezing phase.

7.2 OUTLOOK

The implementation of these schemes in an experiment can lead to a first realization of an entanglement-enhanced atom interferometer. This could pave the way to more sensitive atom interferometers when the increase of other parameters is not possible anymore or too challenging. These measurements would also show where technical noise sources occur and if one of the two schemes has an advantage.

The use of these schemes in experiments with single-atom detection would allow the use of stronger entangled states, like Schrödinger-cat states, which could improve the sensitivity of the interferometer even more.

Also the implementation of the optimal squeezing protocol can lead to a further improvement of an a entanglement-enhanced interferometer in the presents of density shift.

Further improvements could be the use of two inverted interferometers behind each other to gain a common mode noise rejection to noise caused by the reference mirror.

TECHNICAL OUTLOOK The implementation of a more stable Raman system will also allow to demonstrate the use of LMT with multiple $\hbar k$. But for that, the two clouds need to be well separated in the frequency domain due to the Doppler shift. This requires a sufficient free fall time before the interferometer sequence. This is not possible in our current setup, because our vacuum chamber is not long enough and

the detection system is not in an optimal position. It is possible to move the detection system to reach a sufficient free fall time. In principle, the Raman system could also be used to change the internal states of the atoms instead of a microwave system if the transfer becomes more efficient than a microwave transfer. A higher stability also elongates the total measurement time which will allow to measure more data points. This elongation of the possible averaging time will improve the resolution of the measurement.

A further improvement of the magnetic field stabilization is the second major point that would improve the long term stability and also the noise during the interferometer. Therefore, it is desirable to improve this first. A further technical improvement could be the increase of the dipole trap depth to increase the evaporation time and with that also the cycle time. The improvement of the temperature stabilization on the experimental table and on the reference resistors for the laser locks and magnetic field stabilizations could improve the experiment in terms of the described diffuse drift behavior of the complete experiment over days.

It needs to be investigated how much the wavefront of the Raman laser influences the transfer of the atoms and if the intensity gradient may be a problem when the now existing noise sources are reduced.

A beneficial improvement for all our experiments with entangled atoms would be the generation of a stronger squeezed state by reducing the noise during the state generation process.

POSSIBLE LONG TERM GOAL The long term goal could be to enable an entanglement-enhanced atom gravimeter, whose absolute value is better than a classical interferometer with the same parameters and also reach the best sensitivity. Therefore, the schemes that will be tested, should be implemented in VLBAI. The VLBAI is a long baseline atom interferometer which is build in Hannover and features a excellent magnetic shielding, a free fall distance of 10m, a catapult mode and BEC source with a high repetition rate. This will allow for a free fall distance of 10m for the interferometer or longer for sequences that are using the catapult mode. In this setup, the order of magnitude in sensitivity is reached where entanglement instead of other less practical parameters will be useful to further increase the sensitivity.

A possible use of such a setup would be the generation of macroscopic entangled states, on the meters distance scale with evolution times in the range of seconds. Due to the large possible splitting of the state, it would be possible to test local collapse theories [75]. Another possibility would be the test of the characteristics of an entangled state in an macroscopic appearance. Also it would allows test of quantum information protocols in entangled BECs over the distance of meters.

Atom interferometer can also be employed to measure gravitational waves on earth and in space [7, 76]. These detectors would be highly

sensitive in frequency ranges, where laser interferometer as gravitational wave detectors are less sensitive. They assume in both papers extreme high sensitivities, where they already including squeezing, to reach sensitivities below the shot-noise limit. Therefore, we could build such an source for entanglement, which then could be implemented in such a gravitational wave detector.

APPENDIX

CALCULATIONS

A.1 OPTIMAL SQUEEZING

We are starting with a squeezed vacuum state and the two mode squeezing operator $S(\xi)$.

$$|\psi(t)\rangle = S(\xi)|0,0\rangle \quad (\text{A.1})$$

The squeezing operator is

$$S(\xi) = e^{\frac{1}{2}(\xi(b^\dagger)^2 - \xi^* b^2)}, \quad (\text{A.2})$$

with $\xi = s * e^{i\theta}$ and s as the squeezing strength.

We chose $S_c = e^{-iKH}$, $S = LS_cL^\dagger$ and $\sigma = S \begin{pmatrix} 1 & 0 \\ 0 & 1 \end{pmatrix} S^T$ [41] as before, with

$$L = \begin{pmatrix} 1 & 1 \\ i & -i \end{pmatrix} \quad K = \begin{pmatrix} 1 & 0 \\ 0 & -1 \end{pmatrix}.$$

Now we compare the Hamiltonian with the exponent of S_c which leads to

$$H = \frac{1}{2} \begin{pmatrix} 0 & -i\xi \\ -i\xi^* & 0 \end{pmatrix}. \quad (\text{A.3})$$

Following this, the full exponent is

$$-iKH = \begin{pmatrix} 0 & \xi \\ \xi^* & 0 \end{pmatrix}. \quad (\text{A.4})$$

By writing S_c now as a row and calculate the matrix exponential, we get

$$\begin{aligned} S_c = e^{-iKH} &= \sum_{j=0}^{\infty} \frac{1}{(2j)!} |\xi|^{2j} \begin{pmatrix} 1 & 0 \\ 0 & 1 \end{pmatrix} + \sum_{j=0}^{\infty} \frac{1}{(2j+1)!} |\xi|^{2j} \begin{pmatrix} 0 & \xi \\ \xi^* & 0 \end{pmatrix} \\ &= \cosh(|\xi|) \begin{pmatrix} 1 & 0 \\ 0 & 1 \end{pmatrix} + \sinh(|\xi|) \begin{pmatrix} 0 & \frac{\xi}{|\xi|} \\ \frac{\xi^*}{|\xi|} & 0 \end{pmatrix} \\ &= \cosh(s) \begin{pmatrix} 1 & 0 \\ 0 & 1 \end{pmatrix} + \sinh(s) \begin{pmatrix} 0 & e^{i\theta} \\ e^{-i\theta} & 0 \end{pmatrix} \end{aligned} \quad (\text{A.5})$$

From that we follow [41]

$$S = \cosh(s) \begin{pmatrix} 1 & 0 \\ 0 & 1 \end{pmatrix} + \sinh(s) \begin{pmatrix} \cos(\theta) & \sin(\theta) \\ \sin(\theta) & -\cos(\theta) \end{pmatrix}. \quad (\text{A.6})$$

Now everything is together to calculate σ

$$\sigma = \left(\cosh^2(s) + \sinh^2(s) \right) \begin{pmatrix} 1 & 0 \\ 0 & 1 \end{pmatrix} \quad (\text{A.7})$$

$$+ 2 \sinh(s) \cosh(s) \begin{pmatrix} \cos(\theta) & \sin(\theta) \\ \sin(\theta) & -\cos(\theta) \end{pmatrix} \\ = \cosh(2s) \begin{pmatrix} 1 & 0 \\ 0 & 1 \end{pmatrix} + \sinh(2s) \begin{pmatrix} \cos(\theta) & \sin(\theta) \\ \sin(\theta) & -\cos(\theta) \end{pmatrix}. \quad (\text{A.8})$$

This is used in Sec. 3.2.

A.2 ARTIFICIAL PHASE SHIFT

Here I will explain in more detail how the artificial phase shift is performed. Let me first explain how the data is stored. Lets describe them by a matrix, where the rows are the different evolution times and the column stands for the different measurement point. As an example

$$D = \begin{pmatrix} m_1 t_1 & m_2 t_1 & \dots & m_k t_1 \\ m_1 t_2 & m_2 t_2 & \dots & m_k t_2 \\ \vdots & \vdots & \ddots & \vdots \\ m_1 t_l & m_2 t_l & \dots & m_k t_l \end{pmatrix} \quad (\text{A.9})$$

If the data would be always in a shape like that the calculations would be more easy. However, the amount of the used data points t_l does not need to be the same due to post selection for bad measurement points or errors.

Now I construct the artificial phase shift, in the way that I take the data for the atoms in $|1, -1\rangle$ from data point $m_1 t_1$ and the data for the atoms in $|1, +1\rangle$ from the data point $m_1 t_8$, with is the explained shift,

$$\text{Sum} = |1, -1\rangle(m_k t_1) + |1, +1\rangle(m_k t_{1+s}), \quad (\text{A.10})$$

with s as the amount of steps that the signal should be shifted. Now there is the possibility that k have a different length for different l , therefore I use the shorter row for the calculation and dismiss the measurement points which do not have a counterpart.

To avoid the problem of the different total atom number for different measurements the relative values are used.

BIBLIOGRAPHY

- [1] A. Einstein. "Die Grundlage der allgemeinen Relativitätstheorie." In: *Ann. Phys.* 354.7 (1916), pp. 769–822. ISSN: 1521-3889. DOI: 10.1002/andp.19163540702.
- [2] W Heisenberg. "Über quantentheoretische Umdeutung kinematischer und mechanischer Beziehungen." In: *Z. Physik* 33 (1925), pp. 879–893. DOI: 10.1007/BF01328377.
- [3] E. Schrödinger. "Quantisierung als Eigenwertproblem." In: *Ann. Phys.* 384.6 (1926), pp. 489–527. ISSN: 1521-3889. DOI: 10.1002/andp.19263840602.
- [4] LIGO Scientific Collaboration and Virgo Collaboration. "Observation of Gravitational Waves from a Binary Black Hole Merger." In: *Phys. Rev. Lett.* 116 (6 2016), p. 061102. DOI: 10.1103/PhysRevLett.116.061102. URL: <http://link.aps.org/doi/10.1103/PhysRevLett.116.061102>.
- [5] J. Aasi et al. "Enhanced sensitivity of the LIGO gravitational wave detector by using squeezed states of light." In: *Nature Photon.* 7 (Aug. 2013), pp. 613–619. DOI: 10.1038/nphoton.2013.177.
- [6] James Lough et al. "First Demonstration of 6 dB Quantum Noise Reduction in a Kilometer Scale Gravitational Wave Observatory." In: *Phys. Rev. Lett.* 126 (4 2021), p. 041102. DOI: 10.1103/PhysRevLett.126.041102. URL: <https://link.aps.org/doi/10.1103/PhysRevLett.126.041102>.
- [7] B. Canuel et al. "ELGAR - a European Laboratory for Gravitation and Atom-interferometric Research." In: *Class. Quantum Grav.* 37 (2020). DOI: <https://doi.org/10.1088/1361-6382/aba80e>.
- [8] E. Oelker, R.B. Hutson, and C.J. Kennedy *et al.* "Demonstration of 4.8×10^{17} stability at 1s for two independent optical clocks." In: *Nature Photon.* 13 (July 2019), pp. 714–719. DOI: <https://doi.org/10.1038/s41566-019-0493-4>.
- [9] I. Kruse et al. "Improvement of an Atomic Clock using Squeezed Vacuum." In: *Phys. Rev. Lett.* 117 (14 2016), p. 143004. DOI: 10.1103/PhysRevLett.117.143004. URL: <http://link.aps.org/doi/10.1103/PhysRevLett.117.143004>.
- [10] Michael Keller, Mateusz Kotyrba, Florian Leupold, Mandip Singh, Maximilian Ebner, and Anton Zeilinger. "Bose-Einstein condensate of metastable helium for quantum correlation experiments." In: *Phys. Rev. A* 90 (6 2014), p. 063607. DOI: 10.1103/

- PhysRevA.90.063607. URL: <http://link.aps.org/doi/10.1103/PhysRevA.90.063607>.
- [11] D. K. Shin, B. M. Henson, S. S. Hodgman, T. Wasak, J. Chwedeczek, and A. G. Truscott. “Bell correlations between spatially separated pairs of atoms.” In: *Nat. Commun.* (2019).
- [12] Robert Bucker, Julian Grond, Stephanie Manz, Tarik Berrada, Thomas Betz, Christian Koller, Ulrich Hohenester, Thorsten Schumm, Aurelien Perrin, and Jorg Schmiedmayer. “Twin-atom beams.” In: *Nature Phys.* 7.8 (Aug. 2011), pp. 608–611. ISSN: 1745-2473. DOI: 10.1038/nphys1992.
- [13] J. Estève, C. Gross, A. Weller, S. Giovanazzi, and M. K. Oberthaler. “Squeezing and entanglement in a Bose-Einstein condensate.” In: *Nature* 455.7217 (Oct. 2008), pp. 1216–1219. ISSN: 0028-0836. DOI: 10.1038/nature07332.
- [14] T. Berrada, S. van Frank, R. Bucker, T. Schumm, J.-F. Schaff, and J. Schmiedmayer. “Integrated Mach-Zehnder interferometer for Bose-Einstein condensates.” In: *Nat. Commun.* 4 (June 2013), pp. –. DOI: 10.1038/ncomms3077.
- [15] M. H. Schleier-Smith, I. D. Leroux, and V. Vuletić. “States of an ensemble of two-level atoms with reduced quantum uncertainty.” In: *Phys. Rev. Lett.* 104 (7 2010), p. 073604. DOI: 10.1103/PhysRevLett.104.073604. URL: <http://link.aps.org/doi/10.1103/PhysRevLett.104.073604>.
- [16] Z. Chen, J. Bohnet, S. Sankar, J. Dai, and J. Thompson. “Conditional spin squeezing of a large ensemble via the vacuum Rabi splitting.” In: *Phys. Rev. Lett.* 106.13 (2011), p. 133601. DOI: 10.1103/PhysRevLett.106.133601.
- [17] R. J. Sewell, M. Koschorreck, M. Napolitano, B. Dubost, N. Bebbod, and M. W. Mitchell. “Magnetic Sensitivity Beyond the Projection Noise Limit by Spin Squeezing.” In: *Phys. Rev. Lett.* 109 (25 2012), p. 253605. DOI: 10.1103/PhysRevLett.109.253605.
- [18] J. Hald, J. L. Sørensen, C. Schori, and E. S. Polzik. “Spin squeezed atoms: A macroscopic entangled ensemble created by light.” In: *Phys. Rev. Lett.* 83.7 (1999), p. 1319. DOI: 10.1103/PhysRevLett.83.1319.
- [19] J. Appel, P. J. Windpassinger, D. Oblak, U. B. Hoff, N. Kærgaard, and E. S. Polzik. “Mesoscopic atomic entanglement for precision measurements beyond the standard quantum limit.” In: *Proc. Natl. Acad. Sci. U. S. A.* 106.27 (2009), p. 10960. DOI: 10.1073/pnas.0901550106.
- [20] Onur Hosten, Nils J. Engelsen, Rajiv Krishnakumar, and Mark A. Kasevich. “Measurement noise 100 times lower than the quantum-projection limit using entangled atoms.” In: *Nature* 529 (2016), p. 505. DOI: 10.1038/nature16176.

- [21] C. Gross, T. Zibold, E. Nicklas, J. Estève, and M. K. Oberthaler. “Nonlinear atom interferometer surpasses classical precision limit.” In: *Nature* 464.7292 (Apr. 2010), p. 1165. ISSN: 0028-0836. DOI: 10.1038/nature08919.
- [22] M. Riedel, P. Böhi, Y. Li, T. Hänsch, A. Sinatra, and P. Treutlein. “Atom-chip-based generation of entanglement for quantum metrology.” In: *Nature* 464.7292 (Apr. 2010), p. 1170. ISSN: 0028-0836. DOI: 10.1038/nature08988.
- [23] B. Lücke et al. “Twin matter waves for interferometry beyond the classical limit.” In: *Science* 334.6057 (Nov. 2011), p. 773. URL: <http://www.sciencemag.org/content/334/6057/773.abstract>.
- [24] Xin-Yu Luo, Yi-Quan Zou, Ling-Na Wu, Qi Liu, Ming-Fei Han, Meng Khoon Tey, and Li You. “Deterministic entanglement generation from driving through quantum phase transitions.” In: *Science* 355.6325 (2017), pp. 620–623. ISSN: 0036-8075. DOI: 10.1126/science.aag1106. eprint: <http://science.sciencemag.org/content/355/6325/620.full.pdf>. URL: <http://science.sciencemag.org/content/355/6325/620>.
- [25] C. D. Hamley, C. S. Gerving, T. M. Hoang, E. M. Bookjans, and M. S. Chapman. “Spin-nematic squeezed vacuum in a quantum gas.” In: *Nature Phys.* 8 (Feb. 2012), p. 305. ISSN: 1745-2481. DOI: 10.1038/nphys2245.
- [26] C. Gross, H. Strobel, E. Nicklas, T. Zibold, N. Bar-Gill, G. Kurizki, and M. K. Oberthaler. “Atomic homodyne detection of continuous-variable entangled twin-atom states.” In: *Nature* 480 (Nov. 2011), p. 219. ISSN: 1476-4687. DOI: 10.1038/nature10654.
- [27] J. Peise et al. “Satisfying the Einstein-Podolsky-Rosen criterion with massive particles.” In: *Nat. Commun.* 6 (2015), p. 8984. DOI: 10.1038/ncomms9984.
- [28] Bernd Lücke. “Multi-particle entanglement in a spinor Bose-Einstein condensate for quantum-enhanced interferometry.” PhD thesis. Technische Informationsbibliothek und Universitätsbibliothek Hannover, 2014.
- [29] C. C. Gerry and P.L. Knight. *Introductory quantum optics*. Cambridge University Press, 2005.
- [30] Bernard Yurke, Samuel L. McCall, and John R. Klauder. “SU(2) and SU(1,1) interferometers.” In: *Phys. Rev. A* 33.6 (1986), pp. 4033–4054. DOI: 10.1103/PhysRevA.33.4033.
- [31] Taesoo Kim, Olivier Pfister, Murray J. Holland, Jaewoo Noh, and John L. Hall. “Influence of decorrelation on Heisenberg-limited interferometry with quantum correlated photons.” In: *Phys. Rev. A* 57.5 (1998), pp. 4004–4013. DOI: 10.1103/PhysRevA.57.4004.

- [32] Fabrice Gerbier, Artur Widera, Simon Fölling, Olaf Mandel, and Immanuel Bloch. “Resonant control of spin dynamics in ultracold quantum gases by microwave dressing.” In: *Phys. Rev. A* 73.4, 041602 (2006), p. 041602. DOI: 10.1103/PhysRevA.73.041602. URL: <http://link.aps.org/abstract/PRA/v73/e041602>.
- [33] S. R. Leslie, J. Guzman, M. Vengalattore, Jay D. Sau, Marvin L. Cohen, and D. M. Stamper-Kurn. “Amplification of fluctuations in a spinor Bose-Einstein condensate.” In: *Phys. Rev. A* 79.4, 043631 (2009), p. 043631. DOI: 10.1103/PhysRevA.79.043631. URL: <http://link.aps.org/abstract/PRA/v79/e043631>.
- [34] Eva M. Bookjans, Christopher D. Hamley, and Michael S. Chapman. “Strong quantum spin correlations observed in atomic spin mixing.” In: *Phys. Rev. Lett.* 107 (21 2011), p. 210406. DOI: 10.1103/PhysRevLett.107.210406. URL: <http://link.aps.org/doi/10.1103/PhysRevLett.107.210406>.
- [35] Sven Abend. “Atom-chip Gravimeter with Bose-Einstein Condensates.” PhD thesis. Technische Informationsbibliothek und Universitätsbibliothek Hannover, 2017.
- [36] Saijun Wu, Edward Su, and Mara Prentiss. “Demonstration of an area-enclosing guided-atom interferometer for rotation sensing.” In: *Phys. Rev. Lett.* 99 (17 2007), p. 173201. DOI: 10.1103/PhysRevLett.99.173201. URL: <http://link.aps.org/doi/10.1103/PhysRevLett.99.173201>.
- [37] Edward J. Su, Saijun Wu, and Mara G. Prentiss. “Atom interferometry using wave packets with constant spatial displacements.” In: *Phys. Rev. A* 81 (4 2010), p. 043631. DOI: 10.1103/PhysRevA.81.043631. URL: <https://link.aps.org/doi/10.1103/PhysRevA.81.043631>.
- [38] Logan Latham Richardson. “Inertial noise post-correction in atom interferometers measuring the local gravitational acceleration.” PhD thesis. Technische Informationsbibliothek und Universitätsbibliothek Hannover, 2019.
- [39] Masahiro Kitagawa and Masahito Ueda. “Squeezed spin states.” In: *Phys. Rev. A* 47 (6 1993), pp. 5138–5143. DOI: 10.1103/PhysRevA.47.5138. URL: <http://link.aps.org/doi/10.1103/PhysRevA.47.5138>.
- [40] L. Pitaevskii and S. Stringari. *Bose-Einstein Condensation*. Oxford University Press, 2003.
- [41] Gianfranco Cariolaro and Gianfranco Pierobon. *From Hamiltonians to complex symplectic transformations*. 2017. arXiv: 1704.02008 [quant-ph].

- [42] Susannah M. Dickerson, Jason M. Hogan, Alex Sugarbaker, David M. S. Johnson, and Mark A. Kasevich. "Multiaxis Inertial Sensing with Long-Time Point Source Atom Interferometry." In: *Phys. Rev. Lett.* 111 (8 2013), p. 083001. DOI: 10.1103/PhysRevLett.111.083001. URL: <http://link.aps.org/doi/10.1103/PhysRevLett.111.083001>.
- [43] J. E. Debs, P. A. Altin, T. H. Barter, D. Döring, G. R. Dennis, G. McDonald, R. P. Anderson, J. D. Close, and N. P. Robins. "Cold-atom gravimetry with a Bose-Einstein condensate." In: *Phys. Rev. A* 84.3 (2011), p. 033610. DOI: 10.1103/PhysRevA.84.033610.
- [44] Jason M. Hogan, David M. S. Johnson, and Mark A. Kasevich. *Light-pulse atom interferometry*. 2008. arXiv: 0806.3261 [physics.atom-ph].
- [45] K. Bongs, R. Launay, and M. Kasevich. "High-order inertial phase shifts for time-domain atom interferometers." In: *Appl. Phys. B* 84 (2006), pp. 599–602. DOI: <https://doi.org/10.1007/s00340-006-2397-5>.
- [46] Ch.J. Bordé. "Atomic interferometry with internal state labelling." In: *Phys. Lett. A* 140.1-2 (1989), pp. 10–12. ISSN: 0375-9601. DOI: 10.1016/0375-9601(89)90537-9.
- [47] Giovanni Barontini, Leander Hohmann, Florian Haas, Jérôme Estève, and Jakob Reichel. "Deterministic generation of multi-particle entanglement by quantum Zeno dynamics." In: *Science* 349.6254 (2015), pp. 1317–1321. DOI: 10.1126/science.aaa0754. URL: <http://www.sciencemag.org/content/349/6254/1317.full.pdf>.
- [48] M. Bonneau, J. Ruauadel, R. Lopes, J.-C. Jaskula, A. Aspect, D. Boiron, and C. I. Westbrook. "Tunable source of correlated atom beams." In: *Phys. Rev. A* 87.6 (June 2013), p. 061603. DOI: 10.1103/PhysRevA.87.061603. URL: <http://link.aps.org/doi/10.1103/PhysRevA.87.061603> (visited on 10/13/2013).
- [49] B. Lücke et al. "Twin matter waves for interferometry beyond the classical Limit." en. In: *Science* 334.6057 (Nov. 2011), pp. 773–776. ISSN: 0036-8075, 1095-9203. DOI: 10.1126/science.1208798. URL: <http://www.sciencemag.org/content/334/6057/773> (visited on 03/06/2013).
- [50] J. Dalibard. "Collisional dynamics of ultra-cold atomic gases." In: *Proceedings of the International School of Physics - Enrico Fermi*. Ed. by M. Inguscio, S. Stringari, and C. E. Wieman. Vol. 321. IOS Press, 1999.
- [51] Jian-Wei Pan, Zeng-Bing Chen, Chao-Yang Lu, Harald Weinfurter, Anton Zeilinger, and Marek Żukowski. "Multiphoton entanglement and interferometry." In: *Rev. Mod. Phys.* 84 (2

- 2012), pp. 777–838. DOI: 10.1103/RevModPhys.84.777. URL: <https://link.aps.org/doi/10.1103/RevModPhys.84.777>.
- [52] Ling-An Wu, H. J. Kimble, J. L. Hall, and Huifa Wu. “Generation of Squeezed States by Parametric Down Conversion.” In: *Phys. Rev. Lett.* 57 (20 1986), pp. 2520–2523. DOI: 10.1103/PhysRevLett.57.2520. URL: <http://link.aps.org/doi/10.1103/PhysRevLett.57.2520>.
- [53] Henning Vahlbruch, Simon Chelkowski, Boris Hage, Alexander Franzen, Karsten Danzmann, and Roman Schnabel. “Demonstration of a Squeezed-Light-Enhanced Power- and Signal-Recycled Michelson Interferometer.” In: *Phys. Rev. Lett.* 95.21 (2005), p. 211102. DOI: 10.1103/PhysRevLett.95.211102.
- [54] Alain Aspect, Jean Dalibard, and Gérard Roger. “Experimental Test of Bell’s Inequalities Using Time-Varying Analyzers.” In: *Phys. Rev. Lett.* 49.25 (1982), pp. 1804–1807. DOI: 10.1103/PhysRevLett.49.1804.
- [55] C. Klempt, O. Topic, G. Gebreyesus, M. Scherer, T. Henninger, P. Hyllus, W. Ertmer, L. Santos, and J. J. Arlt. “Parametric amplification of vacuum fluctuations in a spinor condensate.” In: *Phys. Rev. Lett.* 104.19 (2010), p. 195303. DOI: 10.1103/PhysRevLett.104.195303.
- [56] N. N. Bogoliubov. “On the theory of superfluidity.” In: 77. *Engl. Transl. J. Phys.* 11 (1947). *Izv. Akad. Nauk. USSR* 11 (1947), p. 23.
- [57] K. Lange, J. Peise, B. Lücke, I. Kruse, G. Vitagliano, I. Apellaniz, M. Kleinmann, G. Toth, and C. Klempt. “Entanglement between two spatially separated atomic modes.” In: *ArXiv e-prints* (Aug. 2017). arXiv: 1708.02480 [quant-ph].
- [58] Z. Zhang and L.-M. Duan. “Generation of Massive Entanglement through an Adiabatic Quantum Phase Transition in a Spinor Condensate.” In: *Phys. Rev. Lett.* 111 (18 2013), p. 180401. DOI: 10.1103/PhysRevLett.111.180401. URL: <http://link.aps.org/doi/10.1103/PhysRevLett.111.180401>.
- [59] D. Schlippert, C. Meiners, R.J. Rengelink, C. Schubert, D. Tell, É. Wodey, K.H. Zipfel, W. Ertmer, and E.M. Rasel. “Matter-Wave Interferometry for Inertial Sensing and Tests of Fundamental Physics.” In: *CPT and Lorentz Symmetry* (2020). DOI: 10.1142/9789811213984_0010. URL: http://dx.doi.org/10.1142/9789811213984_0010.
- [60] Matt Jaffe, Victoria Xu, Philipp Haslinger, Holger Müller, and Paul Hamilton. “Efficient Adiabatic Spin-Dependent Kicks in an Atom Interferometer.” In: *Phys. Rev. Lett.* 121 (4 2018), p. 040402. DOI: 10.1103/PhysRevLett.121.040402. URL: <https://link.aps.org/doi/10.1103/PhysRevLett.121.040402>.

- [61] J. M. McGuirk, M. J. Snadden, and M. A. Kasevich. "Large Area Light-Pulse Atom Interferometry." In: *Phys. Rev. Lett.* 85 (21 2000), pp. 4498–4501. DOI: 10.1103/PhysRevLett.85.4498. URL: <https://link.aps.org/doi/10.1103/PhysRevLett.85.4498>.
- [62] T. Henninger. "Ultrakalte heteronukleare Feshbach Moleküle." PhD thesis. Leibniz Universität Hannover, 2008.
- [63] C. Klempt, T. van Zoest, T. Henninger, O. Topic, E. Rasel, W. Ertmer, and J. Arlt. "Ultraviolet light-induced atom desorption for large rubidium and potassium magneto-optical traps." In: *Phys. Rev. A* 73 (2006), p. 13410. DOI: 10.1103/PhysRevA.73.013410.
- [64] C. Klempt, T. Henninger, O. Topic, J. Will, St. Falke, W. Ertmer, and J. Arlt. "Transport of a quantum degenerate heteronuclear Bose-Fermi mixture in a harmonic trap." In: *Eur. Phys. J. D* 48 (2008), p. 121. DOI: 10.1140/epjd/e2008-00067-5.
- [65] Oliver Topic. "Resonante Spindynamik in Bose-Einstein-Kondensaten." PhD thesis. Leibniz Universität Hannover, 2010.
- [66] C. Klempt. "Wechselwirkung in Bose-Fermi-Quantengasen." PhD thesis. Hannover: Leibniz Universität Hannover, 2007.
- [67] J. Will. "Realisierung einer magneto-optischen Falle für ^{41}K ." MA thesis. Leibniz Universität Hannover, 2007.
- [68] L. Kattner. "Detection and Stabilization of ultracold Feshbach-Molecules." Masterarbeit. Leibniz Universität Hannover, 2008.
- [69] A. P. Kulosa. "Aufbau eines Lasersystems zur Detektion und Manipulation von Atomen." Staatsexamensarbeit. Leibniz Universität Hannover, 2009.
- [70] Janina Hamann. "Frequency Stabilization of a Laser System Using Modulation Transfer Spectroscopy." B thesis. Leibniz Universität Hannover, 2018.
- [71] Martin Quensen. "Fast Magnetic Field Stabilization Using the Anisotropic Magnetoresistive Effect." MA thesis. Leibniz Universität Hannover, 2020.
- [72] Norman F. Ramsey. "A New Molecular Beam Resonance Method." In: *Phys. Rev.* 76.7 (1949), p. 996. DOI: 10.1103/PhysRev.76.996.
- [73] Norman F. Ramsey. "A molecular beam resonance method with separated oscillating fields." In: *Phys. Rev.* 78.6 (1950), pp. 695–699. DOI: 10.1103/PhysRev.78.695.

- [74] Philipp Kunkel, Maximilian Prüfer, Stefan Lannig, Rodrigo Rosa-Medina, Alexis Bonnin, Martin Gärttner, Helmut Strobel, and Markus K. Oberthaler. "Simultaneous Readout of Noncommuting Collective Spin Observables beyond the Standard Quantum Limit." In: *Phys. Rev. Lett.* 123 (6 2019), p. 063603. DOI: 10.1103/PhysRevLett.123.063603. URL: <https://link.aps.org/doi/10.1103/PhysRevLett.123.063603>.
- [75] Björn Schrämski, Stefan Nimmrichter, and Klaus Hornberger. "Quantum-classical hypothesis tests in macroscopic matter-wave interferometry." In: *Phys. Rev. Research* 2 (3 2020), p. 033034. DOI: 10.1103/PhysRevResearch.2.033034. URL: <https://link.aps.org/doi/10.1103/PhysRevResearch.2.033034>.
- [76] Guglielmo M. Tino et al. "SAGE: A proposal for a space atomic gravity explorer." In: *Eur. Phys. J. D* 73 (2019). DOI: <https://doi.org/10.1140/epjd/e2019-100324-6>.

DECLARATION

Hiermit versichere ich, dass ich die vorliegende Arbeit selbständig und nur unter Benutzung der angegebenen Literatur und Hilfsmittel angefertigt habe. Wörtliche und sinngemäße Zitate sind unter Angabe der Quelle kenntlich gemacht. Die Arbeit hat in gleicher oder ähnlicher Form noch keiner Prüfungsbehörde vorgelegen und ist auch noch nicht veröffentlicht.

Hannover, 15.03.2021

Alexander Idel

PUBLICATIONS

- F. Anders, **A. Idel**, P. Feldmann, D. Bondarenko, S. Loriani, K. Lange, J. Peise, M. Gersemann, B. Meyer, S. Abend, N. Gaaloul, C. Schubert, D. Schlippert, L. Santos, E. Rasel and C. Klempt. "Momentum Entanglement for Atom Interferometry." (2020)
<https://arxiv.org/abs/2010.15796>
- B. Meyer, **A. Idel**, F. Anders, J. Peise and C. Klempt. "Dynamical low-noise microwave source for cold atom experiments." (2020)
<https://arxiv.org/abs/2003.10989>

CURRICULUM VITAE

Personal details

Name	Alexander Idel
Data of Birth	29.03.1992
Place of Birth	Hannover, Germany

Education

11/2016 - now	Doctoral studies at institute of quantum optics, Leibniz university Hannover
10/2014 - 10/2016	Master studies in physics at Leibniz university Hannover
10/2011 - 12/2014	Bachelor studies in physics at Leibniz university Hannover
06/2011	Abitur at Gymnasium Neustadt am Rübenge, Germany